DISSERTATION

Spin Ladder Systems doped with non magnetic Impurities A Quantum Monte Carlo Study.

From code development to simulating NMR spectra.

Ausgeführt zum Zwecke der Erlangung des akademischen Grades eines

Doktors der technischen Wissenschaften

unter der Leitung von

Univ.Prof. Dipl.-Ing. Dr.techn. Peter Mohn

E134

Institut für Allgemeine Physik (IAP)

eingereicht an der Technischen Universität Wien

Fakultät für Physik

von

Dipl.-Ing. Robert Achleitner

0025979

Dürergasse 23, 1060 Wien

Wien, am 03. September 2013

Kurzfassung

Das Ziel dieser Arbeit war die Entwicklung eines wissenschaftlichen Codes, der in der Lage ist realitätsnahe Systeme zu simulieren, und diesen auf einen, nicht gut verstandenen, experimentellen Effekt anzuwenden. Dieser experimentell bekannte Effekt ist die nicht intuitive NMR Signalverbreiterung in „spin-ladder-compounds“ bei niedrigen Temperaturen, wenn diese mit nicht magnetischen Fremdatomen versetzt werden. Insbesondere wurde Zn dotiertes $SrCu_2O_3$ untersucht.
Zu diesem Zweck wurde im Zuge dieser Arbeit ein Quantum Monte Carlo (QMC) Code, im Rahmen der Stochastischen Reihenentwicklung (Stochastic Series Expansion - SSE), geschrieben. Der Code ist eine Weiterentwicklung eines früher entwickelnten Programmes,[1] in welchem nur einfache Spinsysteme ohne äußerem Magnetfeld simuliert werden konnten. Das für diese Studie entwickelte Programm ist in der Lage komplexe Systeme zu simulieren. Dazu gehören Systeme, die über orthogonale Kopplungen hinaus gehen, Systeme mit Löchern, als auch Systeme mit externem Magnetfeld. Zusätzlich wurde eine Effizienzsteigerung bezüglich Rechenzeit durch optimieren des Codes, sowie Parallelisation, die eine Ausführung des Programmes auf einem Grid-System ermöglicht, erreicht.
Dieser hier entwickelte Code, angewandt auf das vorher genannte experimentell boabachtete Phänomen, führt zu der Schlussfolgerung, dass eine Kopplung in Stapel-Richtung (stacking direction) nötig ist, um die experimentelle Verbreiterung zu erreichen. Die hier simulierte Linienbreite benötigt, im Gegensatz zu frühere Studien zu ungestapelten Systemen, keine unphysikalisch großen Korrelationslängen.
Zusätzlich führte die Analyse des Einflusses der Fremdatomkonfiguration auf das NMR Spektrum auf eine Simulationsprozedur, die es ermöglicht, eine große Anzahl an solchen Konfigurationen, basierend auf einigen wenigen QMC Rechnungen, zu simulieren. Diese Methode ist sehr effizient in der Rechenzeit und ermöglicht somit in zukünftigen Arbeiten aufwendigere Untersuchungen in dotierten Spinsystemen.
Die Resultate dieser Dissertation wurden veröffentlicht.[2]

Abstract

The aim of this study was to develop a scientific code capable of simulating systems close to reality and to apply it to simulate and study experimental findings. This experimentally observed effect is the counter intuitive low temperature broadening of the NMR spectra of spin ladder compounds that are doped with a tiny amount ($x \leqslant 0.0025$) of non magnetic impurities, in particularly Zn doped $SrCu_2O_3$.
For this purpose, the code written in this work is a Quantum Monte Carlo (QMC) code in the framework of the Stochastic Series Expansion (SSE) based on earlier investigations,[1] in which a very simple simple program was developed to simulate spin lattice systems without an external magnetic field. The further developed program used in this study is capable to simulate more complex systems, such as models beyond simple orthogonal couplings, systems with holes, and systems in an external magnetic field. Additionally, enhancements in computation time were achieved by code optimization as well as parallelization to allow the execution on a grid computing system. The theory as well as the algorithm behind this method is described in this work.
Applying the developed code to the mentioned experimentally observed effect leads to the conclusion that a coupling in the stacking direction is necessary to describe the desired broadening. Our simulation of the broadening effect does not require physically unlikely large correlation lengths, which have been applied in former studies.
Further, studying the influence of different impurity configurations on the NMR spectrum resulted in the development of a framework to simulate a large amount of impurity configurations based on a few QMC simulations only. This method proved to be very efficient in computation time and thus allows more intense studies of such systems for future works.
The results of this thesis have been published.[2]

Contents

Introduction

This thesis presents the work of the author performed during his time as a PhD student within the Wissenschaftskolleg Computational Material Science of the Austrian Science Fonds (FWF) at the institute for applied physics at Vienna University of Technology.
The thesis is divided in three parts, to guide the reader from the beginning of the development of a code until its application on an experimentally observed effect. The first part provides the reader with the necessary background. There, the Monte Carlo (MC) method and statistic tools are explained in general. Furthermore, the framework of the Stochastic Series Expansion (SSE) is introduced and the required equations for the final Quantum Monte Carlo (QMC) code are derived. For better understanding of the algorithm, the reader will also be introduced into a graphical representation of the model used in this work.
The second part explains the algorithm itself. The two different operator updates are explained, as well as the parallelization of the program. In the end test calculations for simple systems are compared to analytically exact results to demonstrate the quality of the algorithm.
The third part presents a study in which the code is applied to the low temperature broadening effect of NMR spectra in spin ladder compounds upon doping with small amount of non magnetic impurities. After presenting the results and conclusions, obtained with the QMC code, a new procedure is introduced that allows to simulate NMR spectra closer to reality. Since this new method relies only on a few QMC calculations it is very efficient in calculation time, allowing for more detailed investigations of such impurity doped spin ladder systems.

Part I

Theory

Chapter 1

Monte Carlo Method

In this chapter a short overview about the Monte Carlo method is presented. The basic algorithm is explained using the famous problem of calculating π. Further, the reader is introduced in the Metropolis algorithm, which is demonstrated on a two particle Ising model. Additionally basic information about random number generators (RNGs) as well as statistical tools are presented.

1.1 The Beginning of the Monte Carlo Method

The Monte Carlo Method was developed in the late 40s in Los Alamos to solve the problem of neutron diffusion in fissionable material by Ulam, von Neumann and Metropolis. After the development of computers, and thus the ability to quickly calculate the same process over and over again, the idea came up to generate random starting points and velocities for the Neutrons and calculate their trajectories. Using statistical analysis on those simulated trajectories should lead to results comparable to experimentally observed distributions. As almost everything developed in Los Alamos had to be top secret that time, a code name for this method was needed. Since this method works with random starting values, similar to card games in casinos, the name "Monte Carlo" was chosen. [3]
This method is not limited to the original use only. It is a rather general method that can have many applications as stated in the abstract of an article of Metropolis and Ulam. [4]

Since its development, the Monte Carlo method has found its use for many different applications and has proven to be a very powerful computational tool, not restricted to science only.

1.2 Basic Algorithm

The basic algorithm[4] can be summarised as following:

1. Define the configuration space and determine how configurations are being sampled.
2. Generate a configuration
3. Calculate the desired observables
4. Save the data
5. Repeat step 2-4 until a chosen number of configurations has been sampled.
6. Use statistics to analyse the data.

1.3 Example: Calculating PI

A good example to demonstrate the algorithm is the calculation of π. It can be explained in a very descriptive way without the use of computer generated random numbers. Imagine a square with the length of the sides of 1. Draw the quarter of a circle with the radius 1 in it. Then throw, without aiming, darts towards that square. It is assumed that the darts hit that square randomly and uniformly. Then, the ratio between the darts that ended up within the quarter of the circle and the total amount that hit the square is equal to the ratio of the areas of the 2 figures. Using simple

algebra leads to an expression to evaluate π.

$$\begin{aligned} A_{square} &= a^2 \equiv 1 \\ A_{circle} &= \frac{r^2\pi}{4} \equiv \frac{\pi}{4} \\ \frac{N_{circle}}{N_{total}} &= \frac{A_{circle}}{A_{square}} \equiv \frac{\pi}{4} \\ \rightarrow \pi &= 4\frac{N_{circle}}{N_{total}} \end{aligned} \tag{1.1}$$

Applying this model on the basic algorithm (see Sec. 1.2) leads to following procedure:

1. Define the configuration space and determine how configurations are being sampled:

   The configuration space consists out of two states, namely a dart being either under the circle curve or not. The probability distribution on how those two states are sampled is determined by the geometry of the system.

2. Generate a configuration:

   Throw darts without aiming until N_{total} darts are within the square.

3. Calculate the desired observables:

   Count the number of darts under the circle curve and use Equ. 1.1 to calculate Pi and remove the darts.

4. Save the data

   Save the just obtained π_i (label it with the current data number i).

5. Repeat step 2-4 until a chosen number of configurations has been sampled:

   Repeat steps 2-4 until enough data points (π_i) have been sampled. The amount of data points to sample is generally chosen before process.

6. Use statistics to analyse the data:

   Calculate average and the standard deviation out of the data set π_i.

This process can simply be transferred into a computer code by replacing the darts with randomly drawn numbers (Fig. 1.1).

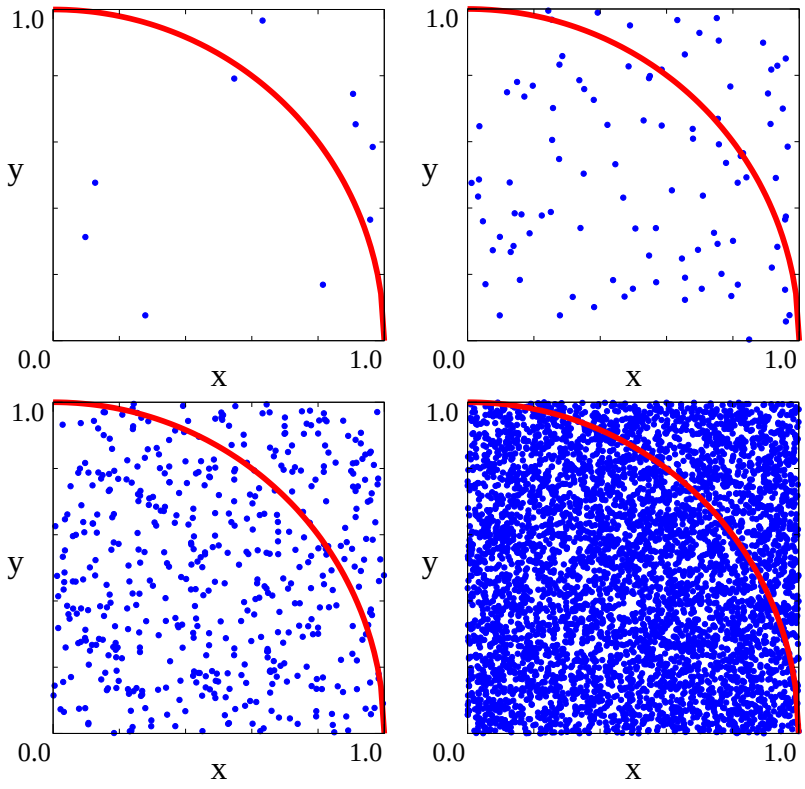

Figure 1.1: Calculation of π. Random dots are drawn over the square. The ratio of the number of dots under the circle curve and the total amount of dots provides an estimate for π

1.4 Random Number Generators (RNGs)

To generate random numbers so called pseudo-random-number-generators are used. Pseudo because they are actually created as a sequence of deterministic numbers. Important for the quality of a RNG is that the sequence of numbers is well distributed and the periodicity of the sequence is as long as possible. Fig.1.2 and Fig. 1.3 illustrate these two properties, that could easily be overlooked in short simulations.

While the standard RNGs of most compilers, with the periodicity of $2^{31}-1$, are sufficient enough for fast calculations, better RNGs such as the Mersenne - Twister[5] are recommended for higher precision. However, for more complex systems, standard RNGs can also lead to reliable results. Especially for Markov processes, in which each configuration can lead to a large number of new configurations, because then it is very unlikely have exactly the same

configuration at the restart of the number sequence. Instead of doing one

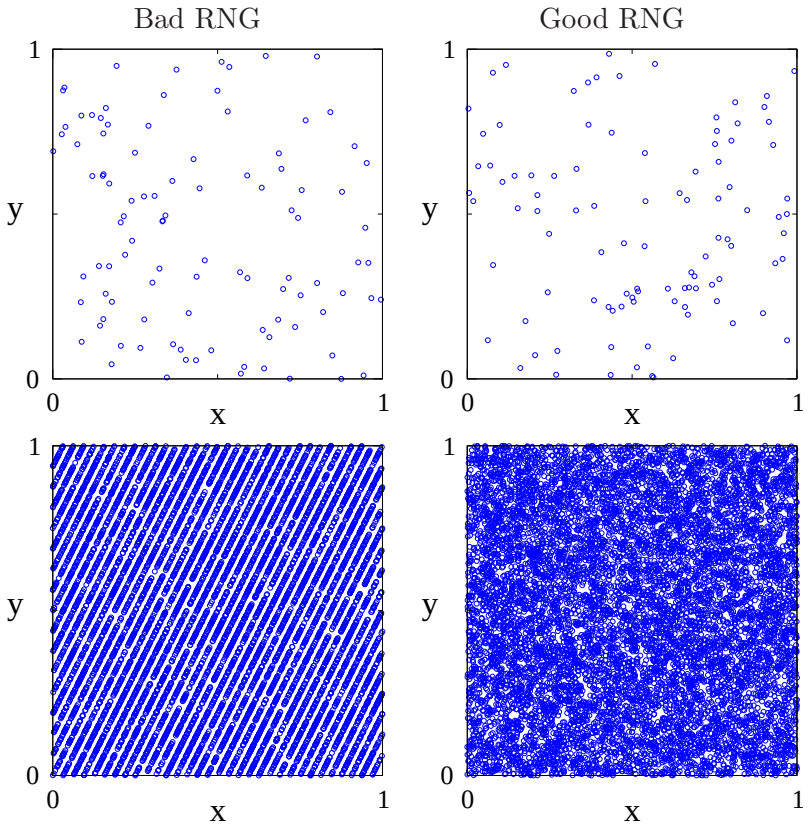

Figure 1.2: Illustration of a good and a bad random number generators. For 100 random points (top row) the bad RNG looks as random as the good RNG. However, for 10000 random points (bottom row), the difference is obvious.

run with lots of steps it is recommend to split up the sweeps into several runs. There are two reasons for doing this. The first reason is to neglect runs that end up in unlikely but possible configurations. The second reason is to neglect the limitation of the RNGs. That limitation comes from the periodicity of RNGs. Also to avoid runs starting with the same seed it is a good idea to generate some kind of list containing random numbers at first, from which a seed is drawn every time a new run starts. That way one will start each run with a different seed for the RNG, which results in different starting values for the simulation. That way unlikely paths of a simulation, that can happen in one run, will average out by other runs.

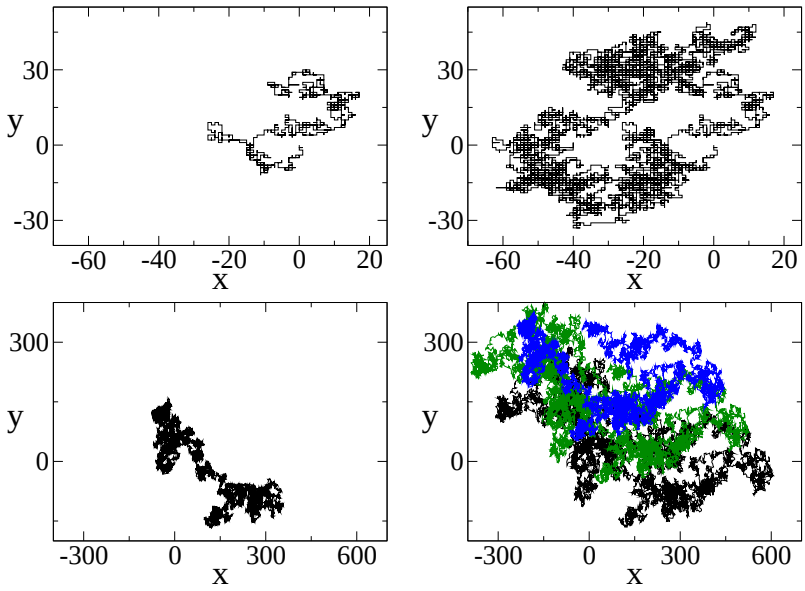

Figure 1.3: Simulated random walk after 1.000 (top left), 10.000 (top right), 100.000 (bottom left), and 10000000 steps. The periodicity of the used random number generator was limited to 400.000 to illustrate repeating patters for simulations longer than that. For easier recognition of the repeating pattern a color code was used (bottom right). Each color is representing a full cycle of the RNG.

1.5 Metropolis Algorithm

While in principle the basic algorithm works for all applicable systems, it can be rather ineffective for systems with larger configuration space. Imagine for example a canonical ensemble with many possible configurations, but only a few of them have reasonable large statistical weights. The basic algorithm would randomly generate configurations, which then would be weighted according to their Boltzmann factor. Thus a lot of configurations will be sampled that hardly contribute to the expectation values, which renders the simulation rather ineffective. To improve the algorithm, Metropolis enhanced it by sampling in a Markov chain rather than randomly generating configurations.[6] A Markov chain is a sequence of configurations. The next generated configuration depends only on the current state and the related transition-probabilities.[7]

Within this algorithm the current configuration will only be altered by a small change. The energy of the newly obtained system is compared with the old one. According to statistical weights and a random number check it is determined whether the new configuration is accepted or rejected. Energetically better configurations will always be accepted. This is repeated until a certain number of samples have been generated.

An important feature of this method is that configurations are sampled according to their statistical weight. Configurations with a small statistical weight will hardly be accepted, even tough they are still possible, to remain the completeness of the ensemble. This importance sampling reduces the amount of configurations needed for a reliable result, which speeds up the simulation overall. Additionally, the statistical weight does not need to be considered anymore for the expectation values of the observables, which simplifies the statistical analysis.

It needs to be mentioned that this algorithm needs a temperature (also called equilibrium) phase. The reason is that the simulation starts at a randomly generated configuration. This includes also less probable states, which can falsify the statistics.

This enhanced algorithm is named after his developer, Metropolis, and thus called Metropolis algorithm.

1.6 Example: Ising model for two spins

This example is used to illustrates the process of the Metropolis algorithm and to demonstrate the possible accuracy achieved with such a method.

1.6.1 Model Description

The Ising model[8] was developed by Ernst Ising to describe spin systems. It is a simplification of the Heisenberg model,[9] which will be discussed later on. For more detailed information about these models we refer to "Magnetism in the Solid State".[10]
In the Ising model, spins reside on a lattice and can have the values +1 or -1. Only two particle exchange (between spin i and spin j) are considered, with $J_{i,j}$ as coupling constant. The Hamiltonian, and thus also the total energy operator, is given as

$$\hat{H} = \sum_{i<j} J_{i,j} S_i S_j \quad . \tag{1.2}$$

In general one can consider also a Zeeman term, which takes the influence of an external magnetic field into account, which is omitted here. In Equ. 1.2 a spin S_i interacts with any other spin S_j. The $J_{i,j}$ vary according to the interaction partners S_i and S_j. For illustration purposes, the model is reduced to its most simple form. For that purpose a system consisting out of two spins only is considered. Then the Hamiltonian reduces to

$$\hat{H} = J S_1 S_2 \quad . \tag{1.3}$$

Since only one coupling is left, the indices in $J_{i,j}$ can be neglected. Note that the coupling constant J classifies the system. For $J > 0$ the energy is lower with anti-parallel aligned spins, referring to an anti-ferromagnetic system. For $J < 0$ the energy is lower when the spins face the same direction, referring to a ferromagnetic system.

1.6.2 Weight and Partition Functions

The weight-function is important, since the configurations are sampled according it. Every system state α inheres a total energy $E(\alpha)$. The statistical

weight of each state is then given by the Boltzmann distribution

$$W(\alpha) = e^{-\beta E(\alpha)} \quad . \tag{1.4}$$

Here β is the inverse temperature $\frac{1}{k_B T}$. Summing up the weights of all states results in the partition function

$$Z = \sum_{\alpha} e^{-\beta E(\alpha)} \quad . \tag{1.5}$$

The expectation value of an observable $f(\alpha)$ is then given by

$$\langle f \rangle = \frac{1}{Z} \sum_{\alpha} f(\alpha) e^{-\beta E(\alpha)} \quad . \tag{1.6}$$

1.6.3 Transition Probability

The simplified system used here consists only out of two spins. Each of them can only have the values +1 and -1, which results in 4 possible states ($|\uparrow,\uparrow\rangle$, $|\uparrow,\downarrow\rangle$, $|\downarrow,\uparrow\rangle$, $|\downarrow,\downarrow\rangle$). To sample this system with a Metropolis algorithm, one spin is updated/flipped and the weight functions before the update (initial state) and after the update (final state) are compared. The ratio between them (using Equ. 1.4)

$$P_{i \to f} = \frac{W_f}{W_i} = e^{-\beta(E_f - E_i)} \tag{1.7}$$

determines the acceptance rate of the spin flip, which corresponds to the transition-probability. Note that for systems with more than one update possibility, one has to consider also the detailed balance.[6] In Equ. 1.7 $P_{i \to f}$ exceeds the value of one, if the final state is energetically favourable. Since a probability larger than 1 has no meaning, one limits $P_{i \to f}$ to one leading to

$$P_{i \to f} = min(e^{-\beta(E_f - E_i)}, 1) \quad . \tag{1.8}$$

This means that a new state with a larger statistical weight than the initial one, is always accepted. On the other hand, energetically less favourable states are still accepted with the probability $P_{i \to f}$.

1.6.4 Algorithm

The algorithm follows in principle the general Monte Carlo algorithm, except that the sampling depends on the current state:

1. Generate a random starting configuration out of $|\uparrow,\uparrow\rangle$, $|\uparrow,\downarrow\rangle$, $|\downarrow,\uparrow\rangle$, $|\downarrow,\downarrow\rangle$.
2. Choose a spin and calculate its probability to flip according equation (1.8).
3. Draw a random number $r \in [0;1]$. If $r \leqslant P_{i\to f}$ then flip the spin, else not. [6]
4. Extract and save the desired data and repeat point 2-4 until the predetermined number of data points has been sampled.
5. Use statistics to calculate expectation values and errors.

1.6.5 Analytical Solution of χ

To demonstrate the quality of the algorithm the calculated susceptibility will be compared to the exact analytical solution. According to [11] χ is given by

$$\chi = \beta(\langle M^2\rangle - \langle M\rangle^2) \tag{1.9}$$

with M as the magnetisation. Using Equ. (1.6) and Equ. (1.9) allows to derive χ for a ferromagnetic system as following:

$$\begin{aligned}
\langle|M|\rangle &= \frac{0 \cdot e^{\beta J} + 2 \cdot e^{-\beta J}}{e^{\beta J} + e^{-\beta J}} = 2\frac{e^{-\beta J}}{e^{\beta J} + e^{-\beta J}} \\
\langle M^2\rangle &= \frac{0^2 \cdot e^{\beta J} + 2^2 \cdot e^{-\beta J}}{e^{\beta J} + e^{-\beta J}} = 4\frac{e^{-\beta J}}{e^{\beta J} + e^{-\beta J}} \\
\langle\chi\rangle &= \beta(\langle M^2\rangle - \langle M\rangle^2) \\
\langle\chi\rangle &= \beta[4\frac{e^{-\beta J}}{e^{\beta J} + e^{-\beta J}} - (2\frac{e^{-\beta J}}{e^{\beta J} + e^{-\beta J}})^2] \\
\langle\chi\rangle &= 4\beta[\frac{e^{-\beta J}}{e^{\beta J} + e^{-\beta J}} - \frac{e^{-2\beta J}}{(e^{\beta J} + e^{-\beta J})^2}] \\
\langle\chi\rangle &= 4\beta[\frac{e^{-\beta J}(e^{\beta J} + e^{-\beta J}) - e^{-2\beta J}}{(e^{\beta J} + e^{-\beta J})^2} \\
\langle\chi\rangle &= 4\beta[\frac{1 + e^{-2\beta J}) - e^{-2\beta J}}{(e^{\beta J} + e^{-\beta J})^2} \\
\langle\chi\rangle &= 4\beta\frac{1}{4\cosh^2(\beta J)} \\
\langle\chi\rangle &= \frac{1}{k_B T}\frac{1}{\cosh^2(\frac{J}{k_B T})}
\end{aligned} \tag{1.10}$$

Here $\langle|M|\rangle$ was used instead of $\langle M\rangle$, because with the absence of an external magnetic field the states $|\uparrow,\uparrow\rangle$ and $|\downarrow,\downarrow\rangle$ are equal.

1.6.6 Results - Demonstration of Accuracy

To demonstrate the potential of the Monte Carlo method, the susceptibility obtained with the Metropolis algorithm (see Sec. 1.6.4) is compared to the analytical solution(see Sec. 1.6.5). Fig. 1.4 shows the susceptibilities obtained by those two different approaches for comparison. For simplicity the constants k_B and J have been set to 1. The quality of the numerical (orange crosses) results when compared with the analytical (solid black line) solution is obvious.
For more detailed information on the Ising model and the applied statistical mechanics we refer to [11].

1.7 Statistics

In this section basic statistics used in Monte Carlo simulations is introduced.

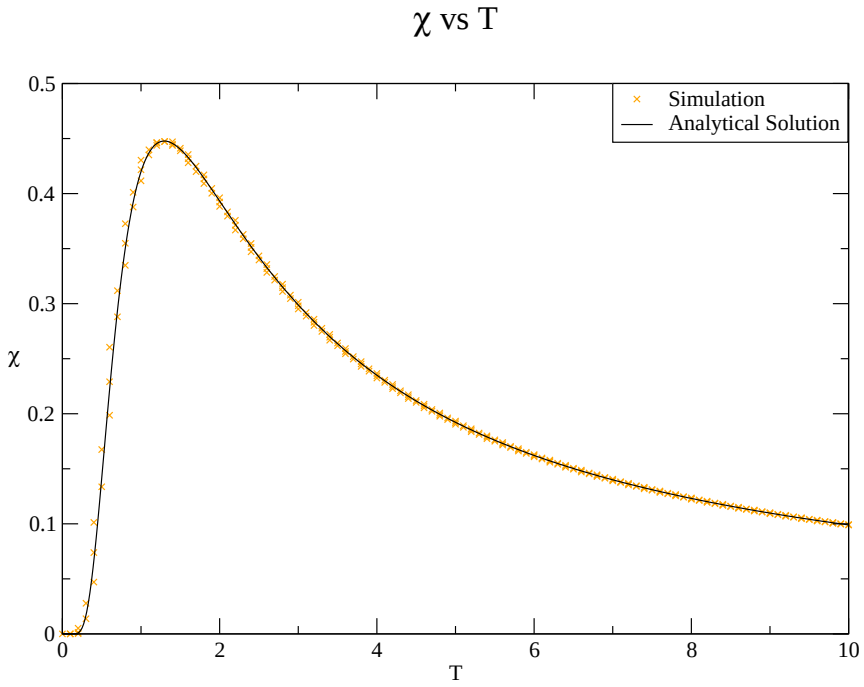

Figure 1.4: 2 spin Ising model. Analytical solution and simulation results for the susceptibility χ.

1.7.1 Averages and Expectation Values

When using importance sampling, such as the Metropolis algorithm, the statistical weights are already considered when the system states are generated. Thus, one can simply average over all the data points (also called measurements) the same way as experimental data are processed. Therefore Monte Carlo simulations are also referred as "simulated experiments". Averages and variances can be calculated with basic statistics.

$$\bar{A} = \frac{1}{N}\sum_{i=1}^{N} A_i \text{ mean value of observable } \hat{A} \tag{1.11}$$

$$\sigma^2 = \frac{1}{N}\sum_{i=1}^{N}(A_i - \bar{A})^2 \text{ variance of the population} \tag{1.12}$$

$$s^2 = \frac{1}{n-1}\sum_{i=1}^{n}(A_i - \bar{A})^2 \text{ variance of the sample} \tag{1.13}$$

It needs to be mentioned that for a Markov process, the errors obtained from Equ. 1.13 are underestimating the actual error. The reason is that the next

generated configuration is achieved by changing the original configuration only by a small amount. In other words, the newly updated configurations are correlated with the initial one and it takes a few update steps to achieve uncorrelated states.

1.7.2 Binning

To obtain the correct errors, "Binning" is used to get rid of the autocorrelation in the sampled data points. The principle is rather simple. Two neighbouring data points are grouped up into a "bin". The average value of both, forms a new data set. This process can be repeated for the new data point generation. Depending on the generation (k) of the generated data set, the bins consist out of 2^k original ($k = 0$) data points (see Fig. 1.5. The

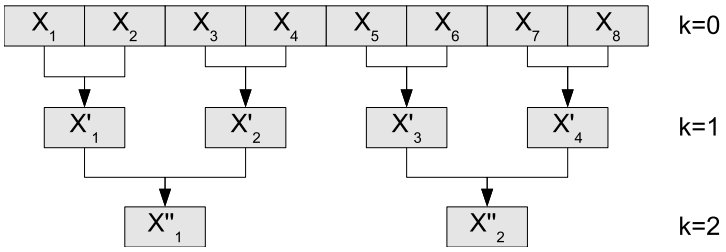

Figure 1.5: Illustration of the binning process

signification of this method is to generate uncorrelated data points and thus obtain a realistic value of the error. The arithmetic average of the data set remains unaffected as is proven in Equ. 1.15.

$$B_j = \frac{1}{2^k} \sum_{i=2^k(j-1)+1}^{2^k(j+1)} A_i \tag{1.14}$$

$$\bar{B} = \frac{1}{\frac{N}{2^k}} \sum_{j=1}^{\frac{N}{2^k}} B_j = \frac{2^k}{N} \sum_{j=1}^{\frac{N}{2^k}} \frac{1}{2^k} \sum_{i=2^k(j-1)+1}^{2^k(j+1)} A_i = \frac{1}{N} \sum_{i=1}^{N} A_i = \bar{A} \tag{1.15}$$

A_i are the initial data points of generation $k = 0$. B_j are the data points of generation k. While the expectation value remains unchanged, the variance, and thus the error, increases. This is a direct consequence of Equ. 1.13 when the number of data points is reduced. However, once the data points

are not correlated anymore, the variance reaches a plateau. This plateau corresponds to the actual error of the sampled data. Fig. 1.6 shows a typical evolution of the standard deviation of the sample, depending on the data point generation k. The red square is the beginning of the plateau, and thus

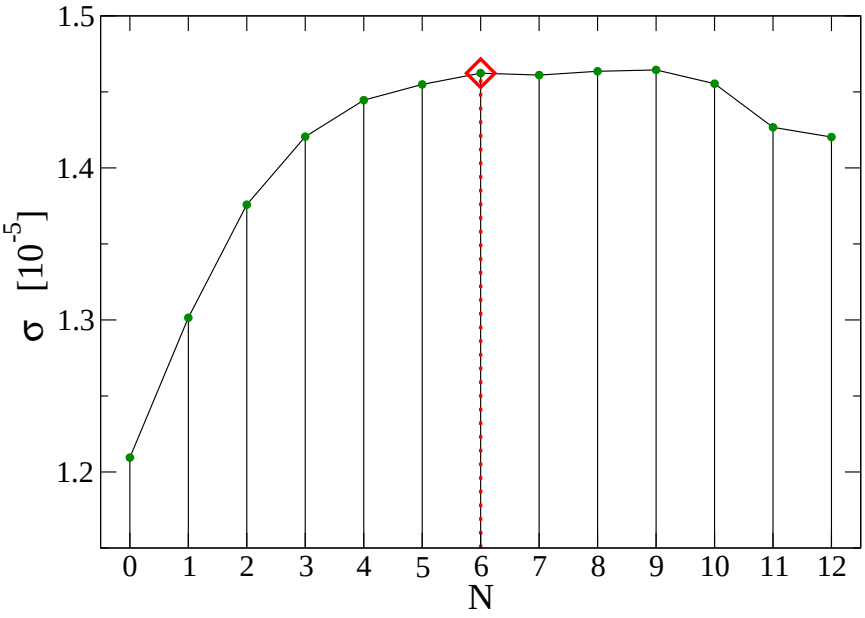

Figure 1.6: Evolution of the standard deviation of the sample during a binning procedure.

corresponds to the actual standard deviation of the sample. Note that the fluctuations after the plateau are caused by a too low amount of data points at higher generations k.

Chapter 2

Stochastic Series Expansion - Classical Approach

While the stochastic series expansion was developed for quantum mechanical systems, here the principle is explained first on classical mechanics. This allows to focus on its quintessence without overloaded equations.

2.1 Principle

The Stochastic Series Expansion (SEE) is a generalization of the Handscomb method[12, 13] developed by Sandvik and Kurkijärvi.[14] In quantum mechanics, instead of trying to solve the trace over the Boltzmann factor analytically, the system is decomposed into diagonal matrix elements that are easily solvable. Those matrix elements are then sampled in form of operator strings (see Chap. 3).
The principle would also work for classical mechanics, if a system would not be solvable analytically. For the next steps, following equations are used:

$$W(\alpha) = e^{-\beta E(\alpha)} \qquad \text{statistical weight} \tag{2.1}$$

$$Z = \sum_{\alpha} W(\alpha) \qquad \text{partition function} \tag{2.2}$$

$$\langle f \rangle = \frac{1}{Z} \sum_{\alpha} f(\alpha) W(\alpha) \qquad \text{expectation value of f} \tag{2.3}$$

$$\tag{2.4}$$

β is the inverse temperature $\frac{1}{k_B T}$. α is a system state. All possible α build

up the configuration space of the system. Assuming the exponential term in Equ. 2.1 cannot be resolved analytically, a series expansion needs to be performed. The resulting partition function is shown in Equ. 2.5.

$$Z = \sum_{\alpha} W(\alpha) = \sum_{\alpha} e^{-\beta E(\alpha)} = \sum_{\alpha} \sum_{n=0}^{\infty} \frac{\beta^n (-E(\alpha))^n}{n!} = \sum_{\alpha} \sum_{n=0}^{\infty} W(\alpha, n) \quad (2.5)$$

n appearing from the power series extends the configuration space by one dimension and a new weight-function is defined

$$W(\alpha, n) = \frac{\beta^n (-E(\alpha))^n}{n!} \quad . \quad (2.6)$$

For $E(\alpha) < 0$ Equ. 2.6 becomes negative. Since a negative statistical weight, and thus a negative probability of a state, is physically impossible, the zero point has to be shifted accordingly ($E(\alpha) \Rightarrow E(\alpha) - \varepsilon$, $\forall E(\alpha) < \varepsilon$) resulting in

$$W(\alpha, n) = \frac{\beta^n (\varepsilon - E(\alpha))^n}{n!} \quad . \quad (2.7)$$

Equ. 2.7 is the governing equation in SSE and used to sample the states consisting of α and n. So far n ranges from 0 until ∞ and a truncation is needed (see Chap. 3)

2.2 Number n and the System Energy

A feature from the new dimension n is that it can be used to calculate the system's energy directly. For that purpose we use the shifted Hamiltonian

$$H(\alpha) = H = \epsilon - E = \epsilon - E(\alpha) \quad . \quad (2.8)$$

The positive definite statistical weight (Equ. 2.7) then becomes

$$W(\alpha, n) = \frac{\beta^n H^n(\alpha)}{n!} \quad . \quad (2.9)$$

The following equations derive the expectation value of H in terms of n:

$$\langle H \rangle = \frac{1}{Z} \sum_{\alpha,n} H(\alpha) \frac{\beta^n H(\alpha)^n}{n!} \tag{2.10}$$

$$\langle H \rangle = \frac{1}{Z} \sum_{\alpha,n} \frac{\beta^n H(\alpha)^{n+1}}{n!} \tag{2.11}$$

$$\langle H \rangle = \frac{1}{Z} \sum_{\alpha,n} \frac{n+1}{\beta} \frac{\beta^{n+1} H(\alpha)^{n+1}}{(n+1)!} \tag{2.12}$$

$$\langle H \rangle = \frac{1}{Z} \sum_{\alpha,m} \frac{m}{\beta} \frac{\beta^m H(\alpha)^m}{(m)!} \tag{2.13}$$

with $m = n + 1$

$$\langle H \rangle = \frac{1}{\beta Z} \sum_{\alpha,m} m \frac{\beta^m H(\alpha)^m}{(m)!} \tag{2.14}$$

$$\langle H \rangle = \frac{1}{\beta Z} \sum_{\alpha,n} n \frac{\beta^n H(\alpha)^n}{(n)!} \tag{2.15}$$

with m renamed to n

$$\langle H \rangle = \frac{1}{\beta Z} \sum_{\alpha,n} n W(\alpha, n) \tag{2.16}$$

$$\langle H \rangle = \frac{\langle n \rangle}{\beta} \tag{2.17}$$

$$\tag{2.18}$$

It is shown that expectation value of H is proportional to the expectation value of n. This means that keeping track of n is sufficient to obtain the system's energy. From $H = \epsilon - E$ follows $E = \epsilon - H$. Thus the expectation value of E is given by

$$\langle E \rangle = \epsilon - \langle H \rangle = \epsilon - \frac{\langle n \rangle}{\beta} \tag{2.19}$$

Chapter 3

Quantum Monte Carlo - Stochastic Series Expansion

In this chapter, the principle of SSE is applied on the quantum mechanical formalism (QMC-SSE). Here, the basic equations, the configurations space, the truncation of the series, the "sign problem", and the here used transition probabilities are discussed. The theory presented here was developed by Sandvik, Kurkijärvi, and Syljuåsen.[14–17]

3.1 Basic Equations

In quantum mechanics statistical weight, partition function, expectation value of an observable $\hat{A}$, and the trace are defined as following:

$$W(\alpha) = \langle\alpha|e^{-\beta\hat{H}}|\alpha\rangle \tag{3.1}$$

$$Z = Tr(e^{-\beta\hat{H}}) \tag{3.2}$$

$$\langle\hat{A}\rangle = \frac{1}{Z}Tr(\hat{A}e^{-\beta\hat{H}}) \tag{3.3}$$

$$Tr(\hat{O}) = \sum_{\alpha}\langle\alpha|\hat{O}|\alpha\rangle \tag{3.4}$$

Here $\hat{\mathrm{H}}$ is the Hamiltonian of the system. The trace sums over all quantum mechanical states α. Analogue to Equ. 2.5 the configuration space can be

extended by one dimension by performing a series expansion.

$$W(\alpha, n) = \frac{\beta^n}{n!}\langle\alpha|(-\hat{H})^n|\alpha\rangle \tag{3.5}$$

$$Z = \sum_{\alpha,n} W(\alpha, n) \tag{3.6}$$

$$\langle\hat{A}\rangle = \frac{1}{Z}\sum_{\alpha,n} A(\alpha)W(\alpha, n) \tag{3.7}$$

To make use of the above equations, $(-\hat{H})^n$ needs to be rewritten in a non power law form. For that purpose, the Ansatz from Equ. 3.8 is used.

$$\hat{H} = -\sum_{a,b} \hat{H}_{a,b} \tag{3.8}$$

The Hamiltonian is decomposed into a sum of single bond operators. b is the bond index (also bond-number) and a the operator type. While the operator types are essential for the algorithm later, here no further definition is needed. Using Equ. 3.8 in $(-\hat{H})^n$ and calculating the bracket leads to Equ. 3.9.

$$\begin{aligned}(-\hat{H})^n = (\sum_{a,b} \hat{H}_{a,b})^n = \\ (\hat{H}_{1,1} + \hat{H}_{1,2} + \hat{H}_{1,3} + \cdots + \hat{H}_{x,n})^n = \\ \hat{H}^n_{1,1} + n \times \hat{H}^{n-1}_{1,1} \times \hat{H}_{1,2} + n \times \hat{H}^{n-1}_{1,1} \times \hat{H}_{1,3} + \cdots + \hat{H}^n_{x,n}\end{aligned} \tag{3.9}$$

Here x represents the number of operator types. Equ. 3.9 consists of terms of single bond operators multiplied with each other in all combinations. This rather cumbersome formalism can be rewritten in a simple form, by introducing "operator strings". An operator string is a product of single bond operators with taking their order into account $(\hat{H}_{a(1),b(1)} \times \hat{H}_{a(2),b(2)} \times ... \times \hat{H}_{a(n),b(n)})$. With the help of such operator strings Equ. 3.9 becomes

$$\sum_{\{a,b\}} \prod_{p=1}^{n} \hat{H}_{a(p),b(p)} \quad . \tag{3.10}$$

The sum is over all possible operator strings $\{a, b\}$ of length n. The partition function (Equ. 3.2) can now be written as

$$Z = \sum_{\alpha,n} \frac{\beta^n}{n!} \sum_{\{a,b\}} \langle\alpha| \prod_{p=1}^{n} \hat{H}_{a(p),b(p)} |\alpha\rangle = \sum_{\alpha,\{a,b\}} \frac{\beta^n}{n!} \langle\alpha| \prod_{p=1}^{n} \hat{H}_{a(p),b(p)} |\alpha\rangle \quad . \tag{3.11}$$

Equ. 3.11 sums over the new configuration space of $\alpha, \{a, b\}$, with a newly defined weight factor (Equ. 3.12).

$$W(\alpha, \{a, b\}) = \frac{\beta^n}{n!} \langle\alpha| \prod_{p=1}^{n} \hat{H}_{a(p),b(p)} |\alpha\rangle \quad . \tag{3.12}$$

3.2 Truncation of the Series

The sum in Equ. 3.11 is over all possible operator strings $\{a, b\}$. The lengths of these operator strings corresponds to n from the series expansion and thus range from 0 to ∞. For utilization in an algorithm, two more modifications on the configuration space have to be made. First of all, a truncation $M \epsilon \mathbb{N}$ of the series is performed. How to choose M without changing the statistics will be explained in Sec. 6.5. The second modification expands all operator strings with a length of $n < M$ to strings with a unified length of M. For that purpose, $M - n$ unit operators ($\hat{H}_{0,0}$) are added to each string. Note, that now n corresponds to the number of non unit operators in a string and not to the length anymore. Sine the order within an operator string matters, there are

$$l = \frac{M!}{(M-n)!n!} \tag{3.13}$$

possibilities for this extension. Because we transformed a $\{a, b, \}$ configuration into l statistically equally distributed configurations we have to divide our former statistical weight by the factor l and obtain Equ. 3.14.

$$W(\alpha, \{a, b\}) = \frac{\beta^n}{n!} \frac{(M-n)!n!}{M!} \langle\alpha| \prod_{p=1}^{n} \hat{H}_{a(p),b(p)} |\alpha\rangle$$
$$W(\alpha, \{a, b\}) = \frac{\beta^n (M-n)!}{M!} \langle\alpha| \prod_{p=1}^{n} \hat{H}_{a(p),b(p)} |\alpha\rangle \tag{3.14}$$

Equ. 3.14 is the base equation used to sample over the configuration space in the algorithm. For mathematical simplifications when deriving transition rates it will be necessary to calculate the eigenvalues of the single bond operators independently. This is achieved by adding identity operators between the single bond operators.

$$\langle\alpha|\prod_{p=1}^{n}\hat{H}_{a(p),b(p)}|\alpha\rangle = \langle\alpha|\hat{H}_{a(1),b(1)}\sum_{\alpha'}|\alpha'\rangle\langle\alpha'|\hat{H}_{a(2),b(2)}\sum_{\alpha'}|\alpha'\rangle\langle\alpha'|\ldots \\ \ldots\hat{H}_{a(2),b(2)}\sum_{\alpha'}|\alpha'\rangle\langle\alpha'|\hat{H}_{a(M),b(M)}|\alpha\rangle \tag{3.15}$$

Since the Eigenvalues of the single bond operators only differ from zero at a certain state α Equ. 3.15 is equivalent to

$$\langle\alpha|\prod_{p=1}^{n}\hat{H}_{a(p),b(p)}|\alpha\rangle = \langle\alpha|\hat{H}_{a(1),b(1)}|\alpha'_1\rangle\langle\alpha'_1|\hat{H}_{a(2),b(2)}\alpha'_2\rangle\langle\alpha'_2|\ldots \\ \ldots\hat{H}_{a(2),b(2)}|\alpha'_{M-1}\rangle\langle\alpha'_{M-1}|\hat{H}_{a(M),b(M)}|\alpha\rangle \tag{3.16}$$

The indices from α'_p in Equ. 3.16 only refer to the position in the operator string and not the state itself. Particularly, $\alpha'_p = \alpha'_{p+1}$ for diagonal $\hat{H}_{a(p+1),b(p+1)}$ and $\alpha'_p \neq \alpha'_{p+1}$ for off-diagonal $\hat{H}_{a(p+1),b(p+1)}$.

3.3 Sign Problem

As already discussed in Chapter 2, it is necessary to shift the zero point of the Hamiltonian to assure a non negative statistical weight. While this works well for classical mechanics, it cannot be done for all quantum mechanical systems. The problem is caused by the off-diagonal elements $\langle\alpha_1|\hat{H}_{a,b}|\alpha_2\rangle$ with $\alpha_1 \neq \alpha_2$, because the zero-point shift only effects diagonal elements. To ensure a positive statistical weight some system requirements need to be fulfilled. First of all, systems with positive off-diagonal elements don't need any restrictions. For Heisenberg systems this is valid for the ferromagnetic case.

For systems with negative off-diagonal elements a closer look at the term 3.17 reveals the required system limitations.

$$\langle\alpha| \prod_{p=1}^{M} \hat{H}_{a,b} |\alpha\rangle \tag{3.17}$$

Since in quantum mechanics the trace is used for the statistics, the state α is identical in the bra and the ket. However, applying the single bond operators of the operator string sequentially on the ket (or the bra) changes the intermediate system state through off-diagonal operators. To achieve a non zero value of the term 3.17, only operator strings are allowed that, once applied completely on a state, result in the initial state ($|\alpha\rangle$ as an eigenvector of $\{a, b, \}$). Further, to ensure a positive value of term 3.17, odd numbers of off-diagonal operators with a negative eigenvalue are forbidden. For example, closed anti-ferromagnetic Heisenberg chains with odd length are forbidden. Such resulting geometrical figures (triangles, pentagons, heptagons, ...) have to be avoided in any model structure.

3.4 Acceptance Rate

With the statistical weight of the configurations (Equ. 3.14) known one can calculate the acceptance rate, which in general is given by Equ. 3.18.

$$P_{accept}(A \to B) = \frac{W(B) P_{select}(B \to A)}{W(A) P_{select}(A \to B))} \tag{3.18}$$

$P_{select}(B \to A)$ and $P_{select}(A \to B)$ are the probabilities to transform state A into B and vice versa and are necessary to meet detailed balance.[6]
While in general transitions from every state into another are possible, the algorithm uses only certain possible transitions with a change of a single operator only. The following two subsections discuss the transitions used in the algorithm.

3.4.1 Diagonal Update Acceptance Rate

The diagonal update considers only transitions between diagonal operators. Strictly speaking only transitions between a unit operator $\hat{H}_{0,0}$ and a diagonal (non-unit) operator $\hat{H}_{1,b}$. This corresponds to a change in the non

unit operator number n by 1. Inserting the statistical weight (Equ. 3.14) into Equ. 3.18 and capping the acceptance rate at 1 leads to the Metropolis acceptance rates 3.19 and 3.20.

$$P_{accept}(n \to n+1) = min(\frac{B\beta}{(M-n)}\langle\alpha|\hat{H}_{1,b}|\alpha\rangle, 1) \tag{3.19}$$

$$P_{accept}(n \to n-1) = min(\frac{(M-n+1)}{B\beta\langle\alpha|\hat{H}_{1,b}|\alpha\rangle}, 1) \tag{3.20}$$

Here the number B is used to fulfill the detailed balance. While in the algorithm there is only one way to replace a non unit operator by an unit operator, there are B possibilities to replace a unit operator with a non unit operator (see Sec. 6.3).

3.4.2 Off-Diagonal Transitions

For this section a small outlook on vertices and the algorithm is provided to understand the upcoming transition rates. Since the system was decomposed into single bond operators, it is sufficient to focus on the spins affected by the current operator ($|\alpha\rangle \Rightarrow |S_i^z, S_j^z\rangle$). The bra-ket notation can then be represented by a vertex (see Equ. 3.21).

$$\langle\uparrow,\uparrow|\hat{H}_{1,b}|\uparrow,\uparrow\rangle \Rightarrow \begin{array}{ccc} \uparrow(1) & & \uparrow(2) \\ & \hat{H}_{1,b} & \\ \uparrow(3) & & \uparrow(4) \end{array} \tag{3.21}$$

A vertex consists out of a single bond operator and the spin states before (top row) and after (bottom row) the operator was acting on them. The 4 corners of a vertex are also called vertex-legs and are labelled 1 (top left), 2 (top right), 3 (bottom left), and 4 (bottom right). Another order of the labels is possible, but consistency is required over all vertices. During an off-diagonal update step (see Sec. 6.4), the algorithm reaches a vertex in one of those legs (= entrance leg) and, after changing the operator due statistical selection, exits the vertex in any of the 4 legs (=exit leg). This update process used in the "operator loop update"[15, 18], was later enhanced by "Directed loops".[16, 17] There a method was developed to shift the transition probabilities towards more probable states without violate the overall statistics. The advantage of directed loops is the reduction of "bouncing"

(entrance and exit legs are the same and the operator remains unchanged) effects, which slow down the simulation.
To calculate the transition weights for the off-diagonal updates one has to solve the general direct loop equations[17]

$$\begin{pmatrix} a_{11} & a_{12} & a_{13} & a_{14} \\ a_{21} & a_{22} & a_{23} & a_{24} \\ a_{31} & a_{32} & a_{33} & a_{34} \\ a_{41} & a_{42} & a_{43} & a_{44} \end{pmatrix} \begin{pmatrix} 1 \\ 1 \\ 1 \\ 1 \end{pmatrix} = \begin{pmatrix} W_1 \\ W_2 \\ W_3 \\ W_4 \end{pmatrix} \quad . \tag{3.22}$$

a_{ij} are the transition weights and W_i the total statistical weights of the possible vertices after the update. The transition probabilities are defined as

$$P(i \to j) = p_{ij} = \frac{a_{i,j}}{W_i} \tag{3.23}$$

Since vertices of the type $\langle\uparrow,\uparrow |\hat{H}_{a,b}| \downarrow,\downarrow\rangle$ are not allowed one of the W_i is equal to 0 and Equ. 10 reduces to a 3x3 matrix resulting in

$$\begin{pmatrix} a_{11} & a_{12} & a_{13} \\ a_{21} & a_{22} & a_{23} \\ a_{31} & a_{32} & a_{33} \end{pmatrix} \begin{pmatrix} 1 \\ 1 \\ 1 \end{pmatrix} = \begin{pmatrix} W_1 \\ W_2 \\ W_3 \end{pmatrix} \quad . \tag{3.24}$$

Further, exchanging entrance and exit legs, results in statistically equal vertices, so that $a_{ij} = a_{ji}$. The equation system now consists out of 3 equations with 6 variables (See Equ. 3.25).

$$\begin{pmatrix} a_{11} & a_{12} & a_{13} \\ a_{12} & a_{22} & a_{23} \\ a_{13} & a_{23} & a_{33} \end{pmatrix} \begin{pmatrix} 1 \\ 1 \\ 1 \end{pmatrix} = \begin{pmatrix} W_1 \\ W_2 \\ W_3 \end{pmatrix} \quad . \tag{3.25}$$

Because of this over-determination, 3 of the a_{ij} can be chosen freely. To sample with a minimum of bounces, the diagonal elements a_{ii} are set as small as possible. Three different cases can occur and the matrix elements a_{ij} have to be adjusted accordingly.

Case A - One of the weights W_i equals zero

This case occurs when one of the 3 vertices involved consists out of a single bond operator, which expectation value equals zero. This corresponds usually to the diagonal operator with the most negative eigenvalue.
Because one $W_i = 0$, the matrix in Equ. 3.25 is reduced by one dimension. The diagonal elements a_{ii} are simply set to zero and the resulting directed loop equations reduce to

$$\begin{pmatrix} 0 & a_{12} \\ a_{12} & 0 \end{pmatrix} \begin{pmatrix} 1 \\ 1 \end{pmatrix} = \begin{pmatrix} W_1 \\ W_2 \end{pmatrix} \quad . \tag{3.26}$$

The transition probabilities (Equ. 3.23) result in

$$p_{12} = \frac{W_1}{W_1} = 1 \tag{3.27a}$$

$$p_{21} = \frac{W_2}{W_2} = 1 \tag{3.27b}$$

Thus, for such an update, the system propagates to the only possible state, without the need to draw a random number.

Case B - $W_i + W_j \geqslant W_k$ for all permutations of i, j, k

The probably most general case is $W_i + W_j \geqslant W_k$ for all permutations of i, j, k, which, for example, appears in a Heisenberg model with a small external magnetic field. In that case the diagonal elements a_{ii} are set to zero. The resulting direct loop equations then reduce to

$$\begin{pmatrix} 0 & a_{12} & a_{13} \\ a_{12} & 0 & a_{23} \\ a_{13} & a_{23} & 0 \end{pmatrix} \begin{pmatrix} 1 \\ 1 \\ 1 \end{pmatrix} = \begin{pmatrix} W_1 \\ W_2 \\ W_3 \end{pmatrix} \quad . \tag{3.28}$$

The resulting transition probabilities are then given by Equations 3.29.

$$p_{12} = \frac{W_1 + W_2 - W_3}{2W_1} \tag{3.29a}$$

$$p_{13} = \frac{W_3 + W_1 - W_2}{2W_1} \tag{3.29b}$$

$$p_{23} = \frac{W_2 + W_3 - W_1}{2W_2} \tag{3.29c}$$

$$p_{21} = \frac{W_1 + W_2 - W_3}{2W_2} \tag{3.29d}$$

$$p_{31} = \frac{W_3 + W_1 - W_2}{2W_3} \tag{3.29e}$$

$$p_{32} = \frac{W_2 + W_3 - W_1}{2W_3} \tag{3.29f}$$

In the algorithm, one has to draw a random number between 0 and 1 and chose the propagation according to Equations 3.29.

Case C - $W_i + W_j < W_k$ **for one of the permutations of** i, j, k

The case $W_i + W_j < W_k$ occurs when one state is much more probable than the other two together. In a Heisenberg systems this is achieved by using a strong external magnetic field.

Here the diagonal elements a_{ii} cannot be set to zero, because then one of the transition probabilities would be negative (see Equations 3.29). The solution is to keep the diagonal matrix element $a_i i$ of the state with the maximum weight non zero, and instead forbid the the transition between the two lower probable states. For the following equations, W_1 is assumed to be the largest weight. Then the directed loop equations are

$$\begin{pmatrix} a_{11} & a_{12} & a_{13} \\ a_{12} & 0 & 0 \\ a_{13} & 0 & 0 \end{pmatrix} \begin{pmatrix} 1 \\ 1 \\ 1 \end{pmatrix} = \begin{pmatrix} W_1 \\ W_2 \\ W_3 \end{pmatrix} \quad . \tag{3.30}$$

The resulting transition probabilities are then given by Equations 3.31.

$$p_{11} = \frac{W_1 - W_2 - W_3}{W_1} \tag{3.31a}$$

$$p_{12} = \frac{W_2}{W_1} \tag{3.31b}$$

$$p_{13} = \frac{W_3}{W_1} \tag{3.31c}$$

$$p_{21} = \frac{W_2}{W_2} = 1 \tag{3.31d}$$

$$p_{31} = \frac{W_3}{W_3} = 1 \tag{3.31e}$$

Only if the algorithm enters the vertex in the most probable state, a random number needs to be drawn. In that case a bounce is possible as well as an update to one of the less probable states. On the other hand, when entering the vertex in a less probable state the system always propagates to the most probable one.

Chapter 4

Graphical Representation

This chapter introduces the reader to the graphical representation, which is later used to explain the different update processes used in the algorithm. For that purpose an operator string is visualized and its representation is reduced to its most simplified form. Additionally, vertices and the "linked vertex list" are discussed.

4.1 Graphical Representation of Operator Strings

Operator strings can be visually illustrated for better demonstration of how the algorithm samples over the configuration space.[15, 16] As shown in Equ. 3.16, such a string consists of sequentially ordered single bond operators, separated by intermediate spin states. Since this work is focused on the z-components of spin-1/2 particles, only two possible spin states, namely spin up (full blue circle) and spin down (full red curcle), occur. Further, the single bond operators are divided into diagonal (empty black boxes, a=1) and off-diagonal (full black boxes, a=2) operators. Unit operators $\hat{H}_{0,0}$ are represented by an empty space between two intermediate states. Note, that the outer most states α are identical (trace).
Fig. 4.1 shows an operating string for an open spin chain consisting out of 5 spins. The string has a length of $M = 8$ and inheres 3 diagonal and 2 off-diagonal operators (n=5). The numbers 1 to 5 at the top of the coloured dots label the different spins on the lattice. Since only next neighbour interaction is allowed, only four different bonds (spin 1 - spin 2, spin 2 - spin 3, spin 3 - spin 4, spin 4 - spin 5) exist. The top and bottom rows of the

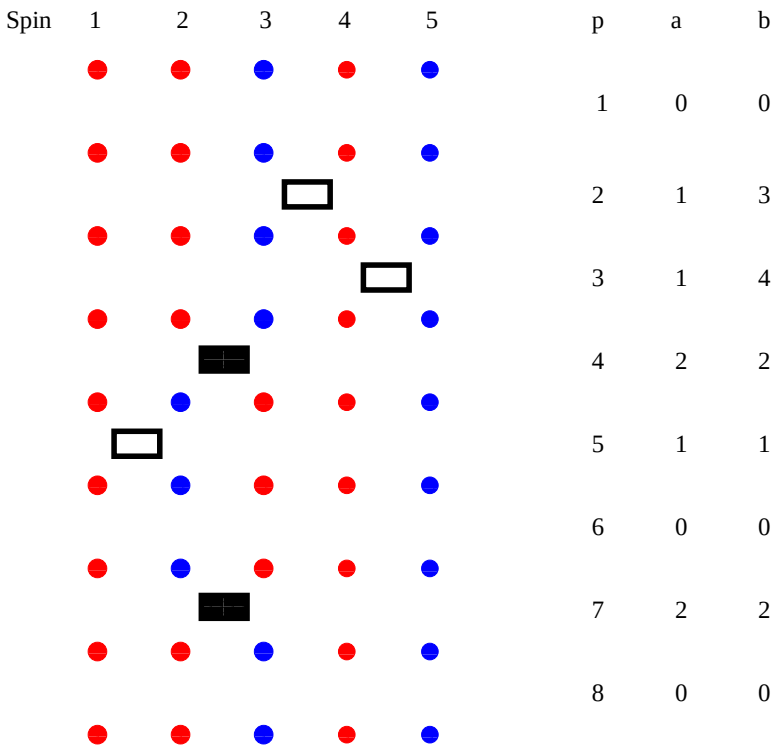

Figure 4.1: Complete Operatorstring at a defined state $|\alpha\rangle = |\uparrow,\uparrow,\downarrow,\uparrow,\downarrow\rangle$

coloured dots represent the spin state $|\alpha\rangle = |\downarrow,\downarrow,\uparrow,\downarrow,\uparrow\rangle$. The intermediate spin states correspond to the α'_p in Equ. 3.16. The space between two spin states α'_p represents the current single bond operator at this position. Empty spaces refer to an unit operator $\hat{H}_{0,0}$ (a=0). Empty black boxes represent diagonal operators(a=1), while full black boxes correspond to off-diagonal operators (a=2). The three columns on the right refer to the position (p) in the operator string, the operator type (a) and, the bond (b) the current operator is acting on.

When propagating the system from the top towards the bottom, the effects of the different operators become clear. While the diagonal operators do not change the spin state, the off-diagonal ones flip both spins belonging to the corresponding bond. This difference is used in the algorithm to sample the configurations space in two different update steps. Once the whole operator string acted on the initial spin state α, the system returns to exactly this initiate state again, which needs to be considered in the update steps as well. It needs to be mentioned that cutting the operator string at any position and

reattaching the two pieces in different order, leads to a new operator string with equal statistical weight. This can be used to calculate the averages of local spins.
In Fig. 4.1 all intermediate spin values are drawn, but the amount of spin flips is rather small. Since those spin flips only occur due off-diagonal operators, it is sufficient to draw only the operators with their four spin states. The resulting representation is demonstrated in 4.2. The operators with

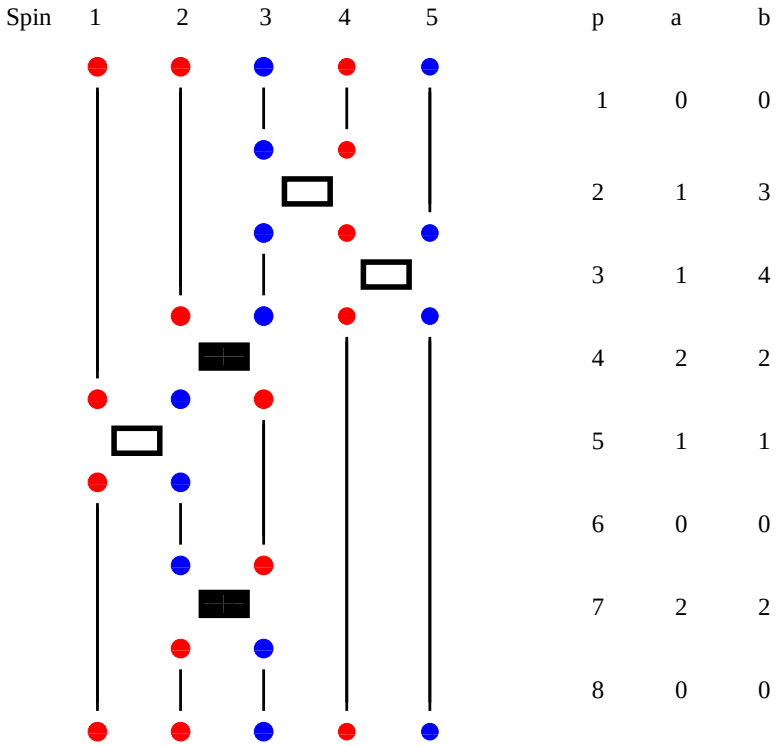

Figure 4.2: Simplified graphical Interpretation of an operator string

their 4 spin states form "vertices", which are connected by vertical lines. This simplified illustration covers all the important information, so that the columns p, a, and b are not needed in future plots. Also this representation is a great tool to discuss and plan the algorithm.

4.2 Vertices and Linked Vertex List

A vertex consists of a single bond operator, an entrance, and an exit leg. The possible combinations are limited by the system. The weights of the different vertices are given by the transition probabilities in Sec. 3.4.2 in Chap. 3. In other words, vertices describe the update process at the local single bond operator,when initiating the the update on the spin at the entrance leg. In Fig. 4.3 the possible sets of vertices for the Heisenberg system are shown. These vertices are used in the "loop algorithm"[18] to perform off-diagonal updates (see Sec. 6.4).

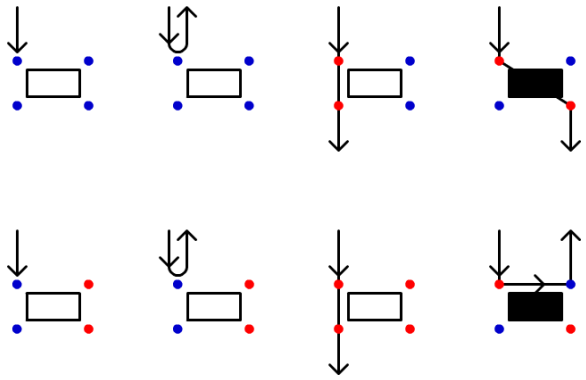

Figure 4.3: Vertices in a Heisenberg system.

Linked Vertex List

In the loop algorithm a walker is propagating between and along the vertices. The linked vertex list is a map, sending the walker to the next vertically connected vertex. It is constructed by defining a $4 \times M$ vertex leg space and connecting each leg with its vertically closest leg. Due to periodic boundary conditions within an operator string, a vertex can even be connected with itself. Once the map is complete (all legs are connected with another one), the list is used to generate a loop (see Sec. 6.4).

Chapter 5

Heisenberg Model

This chapter introduces the reader to the Heisenberg model. After a general description, the effective Hamiltonian used in the QMC-SSE simulations is explained.

5.1 General Model

The Heisenberg model[9] is a lattice model developed to describe spin-spin interactions. In contrast to the Ising model[8] the spins are treated three dimensionally. In the classical limiting case that the spins completely align with the z-axis, the Ising and Heisenberg model are equivalent. The quantum mechanical Heisenberg Hamiltonian without an external magnetic field is given as

$$\hat{H} = \sum_{i<j} J_{i,j} \hat{S}_i \hat{S}_j \quad , \tag{5.1}$$

with the spin operators $\hat{S}_i$, $\hat{S}_j$ and the coupling constant $\mathrm{J}_{i,j}$. Performing the dot product of the spin operators results in

$$\hat{H} = \sum_{i<j} J_{i,j} (\hat{S}_i^x \hat{S}_j^x + \hat{S}_i^y \hat{S}_j^y + \hat{S}_i^z \hat{S}_j^z) \quad . \tag{5.2}$$

Introducing the ladder operators

$$\hat{S}^+ = \hat{S}^x + i\hat{S}^y \quad , \quad \hat{S}^- = \hat{S}^x - i\hat{S}^y \tag{5.3}$$

allows to rewrite Equ. 5.2 as

$$\hat{H} = \sum_{i<j} J_{i,j}(\hat{S}_i^z \hat{S}_j^z + \frac{1}{2}(\hat{S}_i^+ \hat{S}_j^- + \hat{S}_i^- \hat{S}_j^+) \quad . \tag{5.4}$$

To complete the model an external magnetic field term is added to Equ. 5.4. The final resulting Hamiltonian is given by Equ.

$$\hat{H} = \sum_{i<j} J_{i,j}(\hat{S}_i^z \hat{S}_j^z + \frac{1}{2}(\hat{S}_i^+ \hat{S}_j^- + \hat{S}_i^- \hat{S}_j^+) - H_{ex}\mu_B g \sum_i \hat{S}_i^z \tag{5.5}$$

H_{ex} is an external magnetic field. Often in computer simulations the external field and the constants in the magnetic term are combined with a scaling factor into a simple $h\hat{S}_i^z$. In this work the full magnetic term is used, since it eases the comparison to experimental parameters.

5.2 Effective Hamiltonian for QMC-SSE

In computer simulations relative parameters are usually preferred over absolute ones. For simplicity constants are usually assumed with a value of 1. The resulting Hamiltonian then reads

$$\overline{\hat{H}} = \sum_{i<j} \overline{J_{i,j}}(\hat{S}_i^z \hat{S}_j^z + \frac{1}{2}(\hat{S}_i^+ \hat{S}_j^- + \hat{S}_i^- \hat{S}_j^+) - \sum_i \overline{h} S_i^z \quad , \tag{5.6}$$

where the $\overline{J_{i,j}} \in (0,1)$ are defined as fractions between the actual coupling constant and the largest appearing coupling constant. The bars are used here to distinguish between the absolute numbers. This simplification works well for model calculations, but also makes the conversion to SI units harder. For this conversion reason, the Hamiltonian used in this work does not use the complete simplification. Which Hamiltonian is used exactly is demonstrated by the following derivation. It also aids to understand the origin of some parameter ratios and their dimensions.
The Boltzmann factor in terms of $k_B T$ is written as

$$e^{-\beta\hat{H}} = e^{-\frac{\hat{H}}{k_B T}} \quad . \tag{5.7}$$

For the next steps the following notation is used. J'$_{i,j}$ are the coupling constants in units of Joule and J'_{max} refers to the largest occurring coupling

constant. This newly defined coupling is introduced into the Boltzmann factor (Equ. 5.8).

$$e^{-\frac{\hat{H}}{k_B T}} = e^{-\frac{\frac{J'_{max}}{J'_{max}}\hat{H}}{k_B T}} = e^{-\frac{\frac{\hat{H}}{J'_{max}}}{k_B \frac{T}{J'_{max}}}} \tag{5.8}$$

Using the notation $J_{i,j} = \frac{J'_{i,j}}{k_B}$ results in coupling constants $J_{i,j}$ in units of Kelvin and in a Boltzmann factor without a k_B (Equ. 5.9).

$$e^{-\frac{\hat{H}}{k_B T}} = e^{-\frac{\frac{\hat{H}}{J'_{max}}}{\frac{T}{J_{max}}}} \tag{5.9}$$

The Hamiltonian used for sampling is now represented by the original Hamiltonian divided by J'_{max} and thus is dimensionless (see Equ. 5.10).

$$\frac{\hat{H}}{J'_{max}} = \sum_{i<j} \frac{J'_{i,j}}{J'_{max}} \{\hat{S}_i^z \hat{S}_j^z + \frac{1}{2}(S_i^+ S_j^- + S_i^- S_j^+)\} - \frac{1}{J'_{max}} H_{ex} \mu_B g \sum_i \hat{S}_i^z \tag{5.10}$$

Note that the units of the coupling constants in Equ. 5.10 are Joule. To avoid rather small numbers, usually Kelvin are used. To this end Equ. 5.10 is multiplied by $\frac{k_B}{k_B}$ and reads

$$\frac{k_B}{k_B}\frac{\hat{H}}{J'_{max}} = -\sum_{i<j} \frac{k_B}{k_B}\frac{J'_{i,j}}{J'_{max}} \{\hat{S}_i^z \hat{S}_j^z + \frac{1}{2}(S_i^+ S_j^- + S_i^- S_j^+)\} - \frac{k_B}{k_B}\frac{H_{ex}}{J'_{max}} \mu_B g \sum_i \hat{S}_i^z \quad . \tag{5.11}$$

Using again the earlier introduced notation $J_{i,j} = \frac{J'_{i,j}}{k_B}$ results in Equ. 5.12.

$$\frac{1}{k_B}\frac{\hat{H}}{J_{max}} = -\sum_{i<j} \frac{J_{i,j}}{J_{max}} \{\hat{S}_i^z \hat{S}_j^z + \frac{1}{2}(S_i^+ S_j^- + S_i^- S_j^+)\} - \frac{H_{ex}}{J_{max}}\frac{\mu_B}{k_B} g \sum_i \hat{S}_i^z \tag{5.12}$$

Equ. 5.12 is the "effective" Hamiltonian used in this work. The actual spin-spin interactions are governed by the ratios of the coupling constants and the actual units do not matter, even tough now given in Kelvin. The magnetic field term has its external field H_{ex} still in Tesla, and by forming the ratio $\frac{\mu_B}{k_B}$ the former uncomfortable (in SI units) constants are reduced to the constant value of 0.671713..., which is a very manageable size for an algorithm. The advantage compared to the usually simplified Hamiltonian (Equ. 5.6) is that external field and temperature are given in Tesla and

Kelvin. However, for comparison between these differently written Hamiltonians following relations are valid:

$$\overline{\hat{H}} = \frac{1}{k_B}\frac{\hat{H}}{J_{max}} \tag{5.13}$$

$$\overline{J_{i,j}} = \frac{J_{i,j}}{J_{max}} \tag{5.14}$$

$$\overline{h} = \frac{H_{ex}}{J_{max}}\frac{\mu}{k_B}g \tag{5.15}$$

5.3 Diagonal and Off-Diagonal Operators

As explained in Chap. 3, in QMC-SSE the Hamiltonian is decomposed into single bond operators. Further it is required to distinguish between diagonal and off-diagonal terms. By looking at Equ. 5.12 and by taking also the unit operator into account, the model consists out of three different operator types:

$$\hat{H}_{0,0} = \sum_{\alpha} |\alpha\rangle\langle\alpha| \tag{5.16a}$$

$$\hat{H}_{1,b} = \frac{J_b}{J_{max}}\hat{S}^z_{i(b)}\hat{S}^z_{j(b)} - \frac{H_{ex}}{J_{max}}\frac{\mu_B}{k_B}g(A_{i(b)}\hat{S}^z_{i(b)} + A_{j(b)}\hat{S}^z_{j(b)}) \tag{5.16b}$$

$$\hat{H}_{2,b} = \frac{J_b}{2J_{max}}(S^+_{i(b)}S^-_{j(b)} + S^-_{i(b)}S^+_{j(b)}) \tag{5.16c}$$

The change in notation ($J_{i,j} \rightarrow J_b$, $S_i \rightarrow S_{i(b)}$, and $S_j \rightarrow S_{j(b)}$) illustrates that the sampling is performed over bonds (b) and not single spins. While for the spin-spin interactions this "bond-sampling" is just a change in notation, it causes a problem with the magnetic field term, because the magnetic energy is located on the spins and not on the bonds. To avoid an overcounting of the magnetic energy, the magnetic field term needs to be distributed over all bonds connecting a spin. Therefore the two factors $A_{i(b)}$ and $A_{j(b)}$ are added to Equ. 5.16b. Their values are simply defined as $A_{i(b)}\frac{1}{Nb_i}$, with Nb_i the number of bonds of the spin i.

5.4 Notation for Spin Ladder Systems

While Equ. 5.12 is generally valid, it is practical for lattice models to rename the coupling constants $J_{i,j}$ according to their coupling "direction". The

labels are a choice of the user. Usually simple numbering (J_1,J_2,J_3,..,J_N for N different coupling directions), labels according to the axis (J_x,J_y,J_z), specific names (J_L, J_R... for **L**eg and **R**ung directions of a ladder system), or any combination of those is used. Since in this work the QMC-SSE code is applied on spin ladder systems (see part III), we use the notation J_L (leg-direction), J_R (rung-direction), and J_3 (stacking direction).

Part II

Algorithm

Chapter 6

Algorithm

This chapter provides the reader insight on the algorithm[14–19] used in this work. Flow charts for different routines as well as the truncation M is discussed. Further a short overview about parallelisation is provided.

6.1 Overview

Figure 6.1 demonstrates the flow chart of the QMC-SSE algorithm, which can be in summarized as:

1. Initialization of system parameters such as lattice geometry and coupling constants. Also the zero point shift for ensuring positive weights is processed here.

2. A sweep is performed, consisting out of one diagonal and one off-diagonal update step. Here also desired data are extracted.

3. Check if the truncation M is large enough. If not, increase it and reset the collected data.

4. If the pre-set number of sweeps has been reached, the simulation ends. Else continue again with point 2.

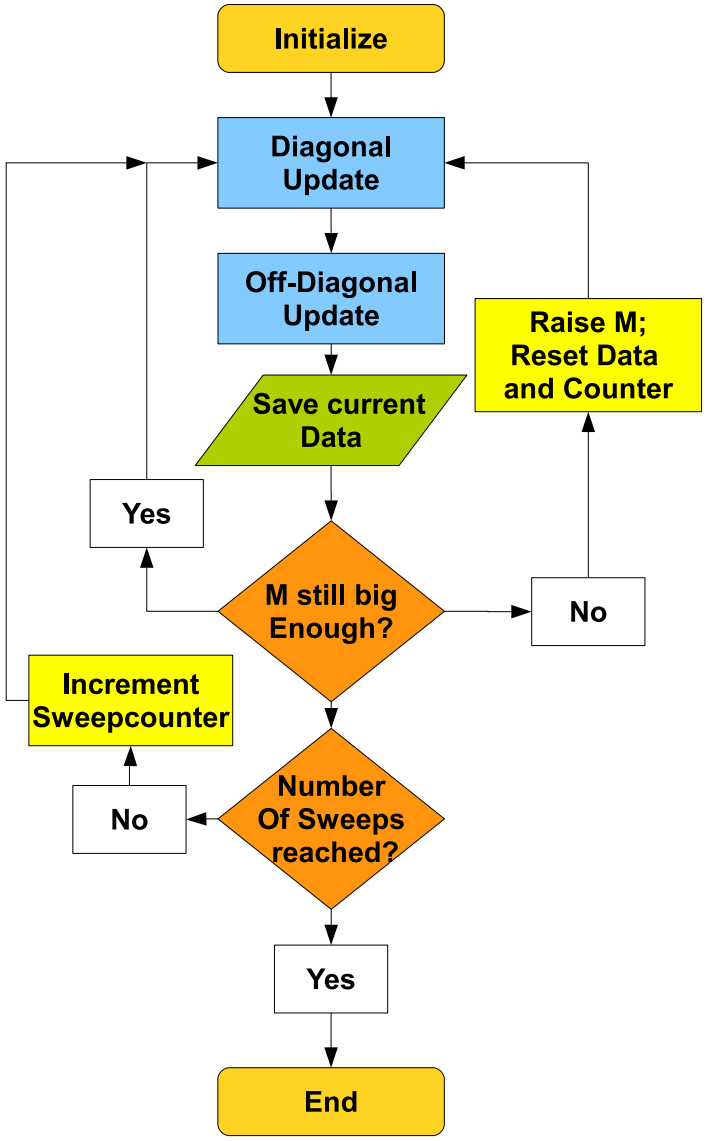

Figure 6.1: Overview-flowchart of the QMC-SSE algorithm

6.2 Initialization

Before starting the actual simulation, the system parameters need to be loaded into the code. It is important to put a lot of effort into this stage. A well designed grid for the algorithm as well as pre-calculating the later used transition probabilities can reduce the computation time by a large amount. Some points to keep in mind:

- **Geometry**

  The algorithm samples over a lattice of bonds. Thus the actual geometry is not important, as long as the correct bonds are considered. The spin lattice is then reduced to an one dimensional lattice (chain), and the bonds connect the associated spins with each other.

- **Statistical weights and the zero point shift**

  In principle the zero point shift to ensure positive statistical weights can be chosen freely, as long as it is large enough. However, the best performance is achieved by shifting the single bond operators by their most negative diagonal eigenvalue. This results in a zero weight for that state which reduces the possible choices for the walker and speeds up the sampling.

- **External magnetic field**

  An external magnetic field interacts with the spins. However, the sampling occurs over bonds and the external field terms need to be distributed along these bonds. Adding the field term of both spins to the bond leads, except for a 2 spin system, to a double counting of those terms. To avoid that, the field terms are equally distributed on all bonds connected with that current spin.

- **Number of sweeps**

  The number of sweeps needs to be chosen according to the other system parameters and the desired system data. For example, one data point of the total magnetization corresponds to one sweep. On the other hand, the local magnetic moments can additionally be averaged over the different intermediate spin states, and thus require less sweeps for a reliable result.

Once the grid for the algorithm has been set up an allowed random initial configuration is being generated and passed towards the sampling routine.

6.3 Diagonal Update

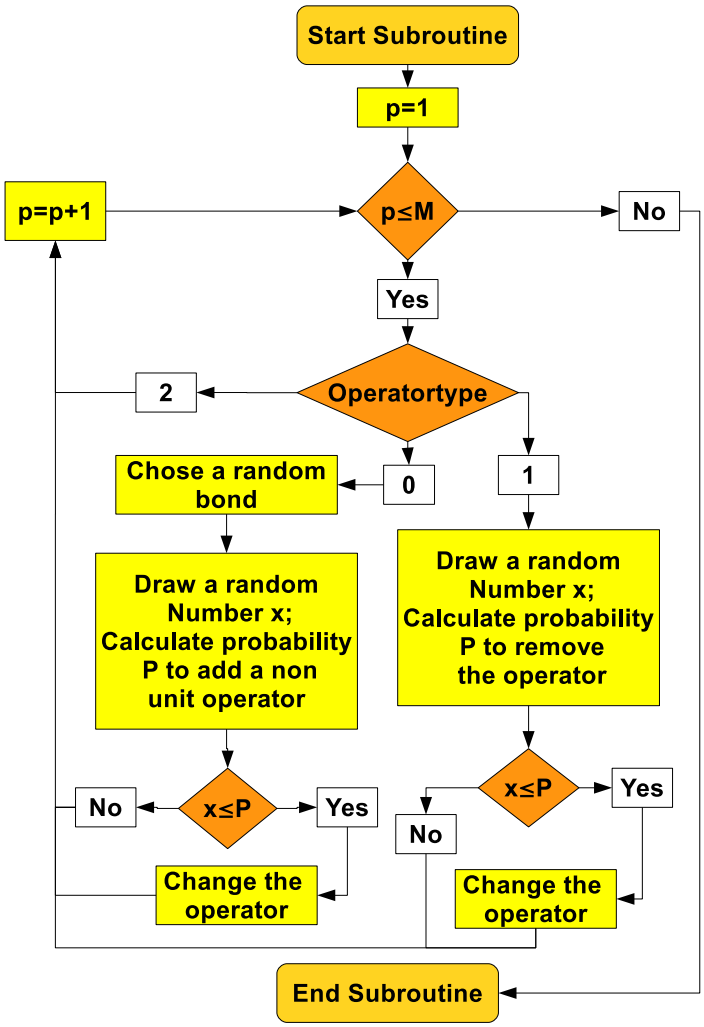

Figure 6.2: Flowchart - diagonal update

In Fig. 6.2 shows the flowchart for the diagonal update routine, which works in detail as following:

- It samples sequentially over all operator string positions $p = 1 \ldots M$

- At every p the current operator type is being determined. The three types are the unit operators (a=0), diagonal operators (a=1), and off diagonal operators (a=2). As the name suggests, only diagonal operator changes are allowed. In particularly, only transfers from an unit operator $\hat{H}_{0,0}$ to a diagonal operator $\hat{H}_{1,b(p)}$ and vice versa are performed. This corresponds to a change in the non-unit operator number n without affecting spin states at any position in the grid.

- Depending on the current operator type at position p the algorithm follows one of the following three branches:

  1. Type 0: A random bond is chosen. The transition probability to add a non unit operator at this bond is calculated according to equation 3.19. A random number is drawn and if it is smaller than the transition probability a new non unit operator is added to the configuration at the chosen bond.

  2. Type 1: A diagonal operator is at the current position in the operator string. The transition probability of removing the operator is being calculated according equation 3.20. A random number is drawn and the change is accepted if the number is smaller than the transition probability.

  3. Type 2: There is an off diagonal operator at the current position of the operator string. Since the diagonal update only considers changes of diagonal operators the algorithm proceeds without taking any action.

- The loop continues until $p = M$

Summarized the diagonal update has 3 major properties:

- Only changes from diagonal non unit operators to unit operators and vice versa are performed.

- The diagonal update changes the non unit operator number n.

- The total spin configuration and thus the current spin state remains unchanged.

6.3.1 Example

Fig. 6.3 shows the start of a diagonal update step. The green arrow indicates the current position in the operator string. Empty solid boxes represent diagonal operators $\hat{H}_{1,b(p)}$ and filled boxes off-diagonal operators $\hat{H}_{2,b(p)}$. After

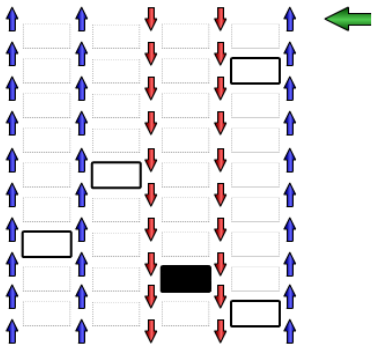

Figure 6.3: Diagonal update

the process starts, each position is checked for a possible operator update, which is indicated by the green arrow moving downwards. Fig. 6.4 shows the system after the first four operator string positions have been updated. The first two rows remained unchanged. This indicates that neither the

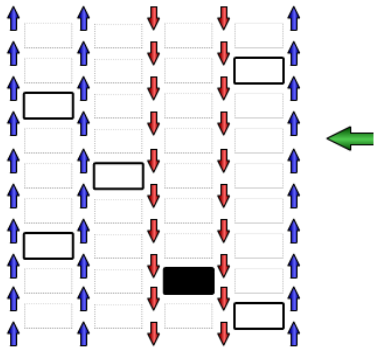

Figure 6.4: Diagonal update

adding of a diagonal operator in the first row, nor the removal of the operator in the second row were accepted. However, the removal of the operator at position three was accepted. Once all positions have been checked for a possible update the diagonal update step ends. During the complete update process (from Fig. 6.3 to Fig. 6.5) two operators were removed (actually replaced by an unit operator) and one was added resulting in a reduction of

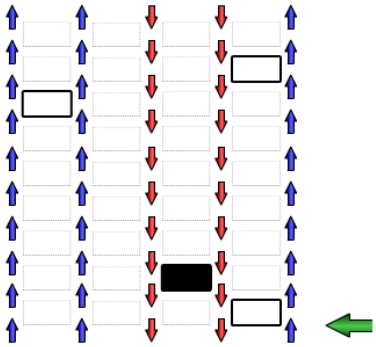

Figure 6.5: Diagonal update

the non unit operator number n by one. Note that off-diagonal operators and spins remain unchanged at this stage of the algorithm.

6.4 Off-Diagonal Update

In the beginning of algorithms simulating vertex models local updates were used for off-diagonal updates. This was rather inefficient and cluster updates in form of loops were being developed [18, 19]. In the loop algorithm a walker is generated that moves through the current configuration and performs changes to operators and spins along its way until it reaches its starting point again. Fig. 6.6 shows the flowchart for the off-diagonal update.

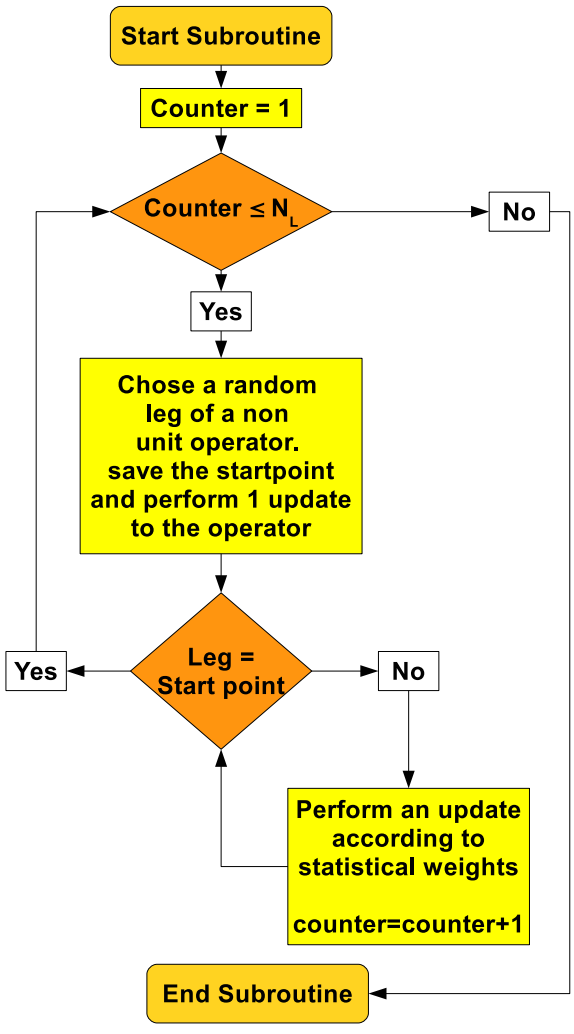

Figure 6.6: Flowchart for the off-diagonal update

In detail this part of the update procedure works as follows:

- Create the linked vertex list.
- Choose a random starting point for the walker by randomly selecting a leg at one of the existent non unit operators.
- Perform an operator change according to the equations in Sec. 3.4.2. An operator change consists of a flip of the spin at the entrance leg, the change of the operator according to statistical weights and an update of the current position of the loop to its corresponding exit leg.
- Move the walker to its linked vertex point according to the linked vertex list and flip all spins along its way.
- Perform such operator updates over and over again until the walker reaches its starting point again and thus closes the loop.
- Count the number of loops generated during one update step. If this number reaches the set number of loops for each update step (N_l in the flow chart) the off-diagonal update step is complete. The number of loops is determined due the equilibrium phase so that the average amount of operator updates is about $2 \times M$.[16, 17]

There are three major properties of the off-diagonal update that complement the features of the diagonal one:

- Non unit operators are transformed into other (allowed) non unit operators.
- The non unit operator number n remains unchanged, because only non unit operators are transformed into each other.
- Spins can flip and thus the different spin states can be sampled.

Example

Fig. 6.7 shows the start of a loop in the off-diagonal update step. The start-

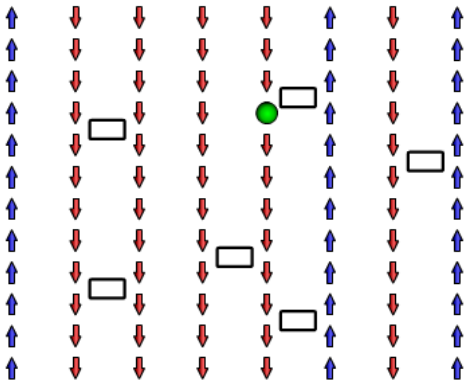

Figure 6.7: Off-diagonal update

ing point (green ball) was drawn randomly under any leg of any operator contained in the complete operator string. Then an operator update is performed, by drawing a random number and checking it against the equations from Sec. 3.4.2. After the exit leg has been determined, the operator is changed accordingly and the walker moves to the connected vertex according to the linked vertex list. All spins passed by the walker are flipped. The resulting intermediate state is demonstrated in Fig. 6.8. The yellow line

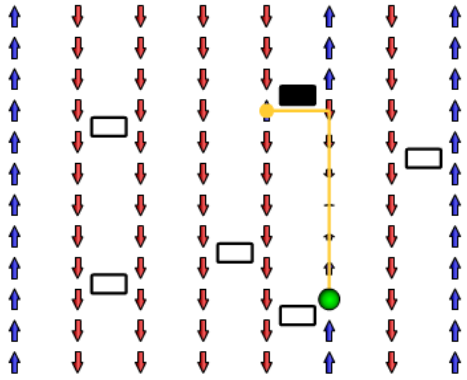

Figure 6.8: Off-diagonal update

represents the path of the walker. Note that the first operator was transformed from a diagonal (empty box) into an off-diagonal (filled box) one. This process is repeated until the next operator is reached (Fig. 6.9).

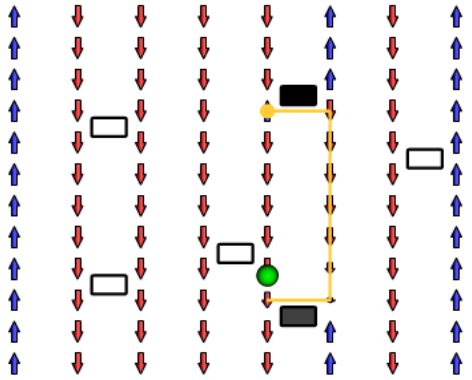

Figure 6.9: Off-diagonal update

As before, the diagonal operator is transformed into an off-diagonal one. But also updates from a diagonal into another diagonal operator are possible, which can be seen through the next operator update. Comparing Fig. 6.9 with Fig. 6.10 might lead to the wrong assumption that the third operator passed, remains unchanged. True is, that the operator type (diagonal) remains the same. However, the spin state on its right side gets altered, and thus the eigenvalue of the operator is different after the update. After

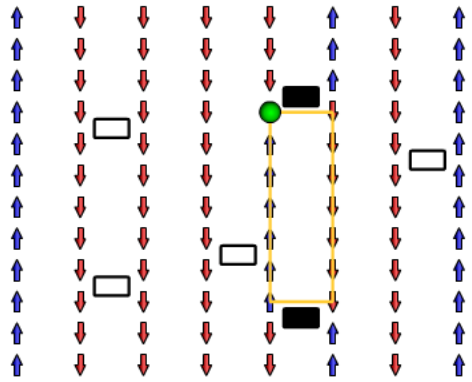

Figure 6.10: Off-diagonal update

the third operator update, the walker reaches its starting point again and thus closes the loop (Closed yellow track in Fig. 6.10). Then a new loop starts, except the set amount of loops has been reached. In that case a measurement (data extraction) is performed and the next diagonal update step starts.

6.5 Truncation M

6.5.1 A Good Estimate for M

The choice of M is important. If M is too small then not all possible states will be sampled, which falsifies the statistics. On the other hand, the runtime increases with increasing M. Thus it is recommended to choose M is as small as possible, but at the same time sufficiently large to remain correct statistics. Fig. 6.11 shows three histograms of n obtained by using three different cutoffs M. The remaining system parameters were identical. The

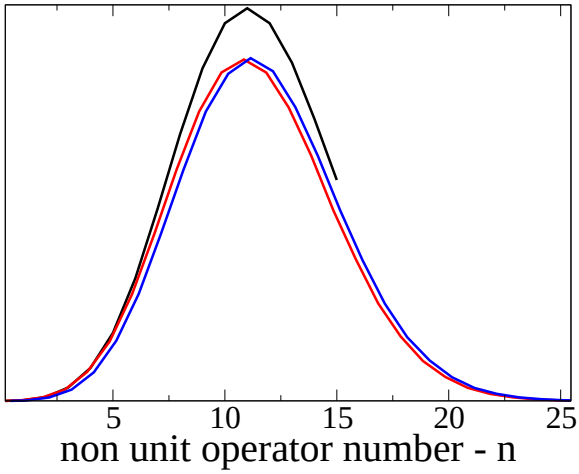

Figure 6.11: Distribution of the non unit operator number n for three different cut-offs $M = 15$ (black), $M = 50$ (red), and $M = 150$ (blue).

histogram with $M = 15$ (black) indicates that not all possible states are covered, because the distribution is cut at $n = 15$, before it can reach the zero line again. The curves with $M = 50$ (red) and $M = 150$ (blue) are shifted along the x-axis to be able to distinguish them, because they are actually overlapping. This clearly demonstrates the existence of a truncation M_{min}, from which on all $M > M_{min}$ lead to the statistically correct result. Considering, that the statistics is governed by the non unit operators, one can truncate with $M = n_{max}$, with n_{max} as the largest occurring non unit operator number during the simulation. According to [16] based on [14] and [12, 13] one can show that $\langle n \rangle = \beta N_b |E_b|$ with N_b as the number of bonds and $|E_b| = -\langle H_b \rangle$ as the internal energy per bond. This internal energy per bond also includes the shift of the energy. Thus, the larger the energy shift the more non unit operators are needed to describe the system, which

is another good argument to keep the energy shift as small as possible. The width of the distribution for n is approximately $\sqrt{\langle n \rangle}$. From this a good guess for n_{max} can be made and the truncation can be set to $M = a \times n_{max}$. a is a security factor to assure $M > n_{max}$ with a value in the range of $(1.2, 1.5)$.

6.5.2 Self Update of M

Even tough M can be guessed quite well, it is recommended to implement a self adjustment of M in the algorithm, if the current n_{max} gets too close to the current M.[14] Once the update process for M is triggered, the subroutine shown in the flow chart in Fig. 6.5.2 is performed.

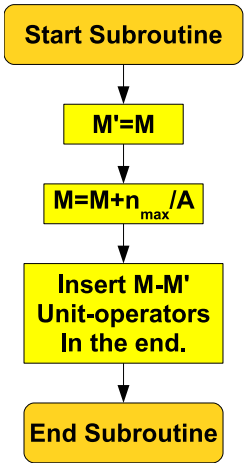

Figure 6.12: Flowchart of the 'update M' subroutine

In detail the procedure works as following:

- Save the current M in M'
- Increase M by a factor of $\frac{n_{max}}{A}$. A is a constant chosen by the user and usually between 2-5 to achieve $M = a \times n_{max}$, with a in $(1.2, 1.5)$.
- Fill the current operator string with $M - M'$ unit operators, by appending them in the end.

- Since the statistical weights change with M, the collected data is reset and the "measurements" start from zero again.

With that algorithm M will be determined automatically, even with a small starting value of M. An example of the self-adjustment of M is shown in Fig. 6.13.

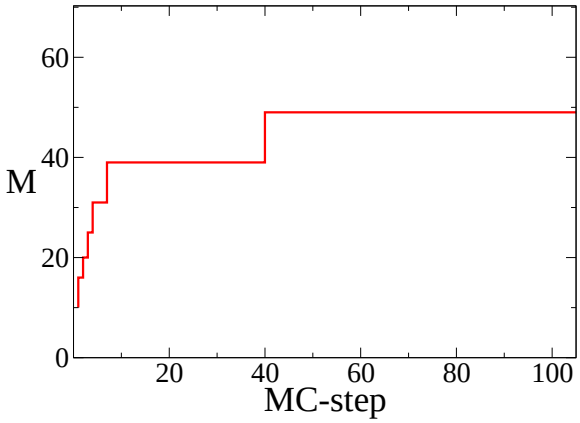

Figure 6.13: Development of the truncation M during the equilibrium phase for 100 steps

Here M starts with a value of 10 and gets progressively increased until its value does not change anymore. Note that A in the adjustment process needs to be chosen wisely. A large factor A leads to small increments of M. On first sight, this looks desirable, since smaller M need less calculation time. However, small steps obviously lead to more updates of M and thus also increase computation time. A balanced value of A is suggested to be 3 or 4.[14]

6.5.3 Equilibrium Phase

The QMC-SSE simulations start with a random spin state α, but the operator string is only filled with unit operators. Thus, before taking measurements, one has to be sure the system reaches its equilibrium. For that purpose, before extracting any data, a certain amount of update steps has to be performed, which is called the "equilibrium phase". While for single node calculations the length of this phase does not matter so much, it has a strong impact of the overall runtime when running parallel on a CPU cluster (see Sec. 6.6.3). To determine a good length for the equilibrium phase, calculations of a spin system has been performed for different equilibrium phase lengths. It turns out, that in combination with the self adjustment of the truncation M, even a very short equilibrium phase can be enough (see Fig. 6.5.3). In Fig. 6.5.3 the equilibrium phase is plotted in respect to

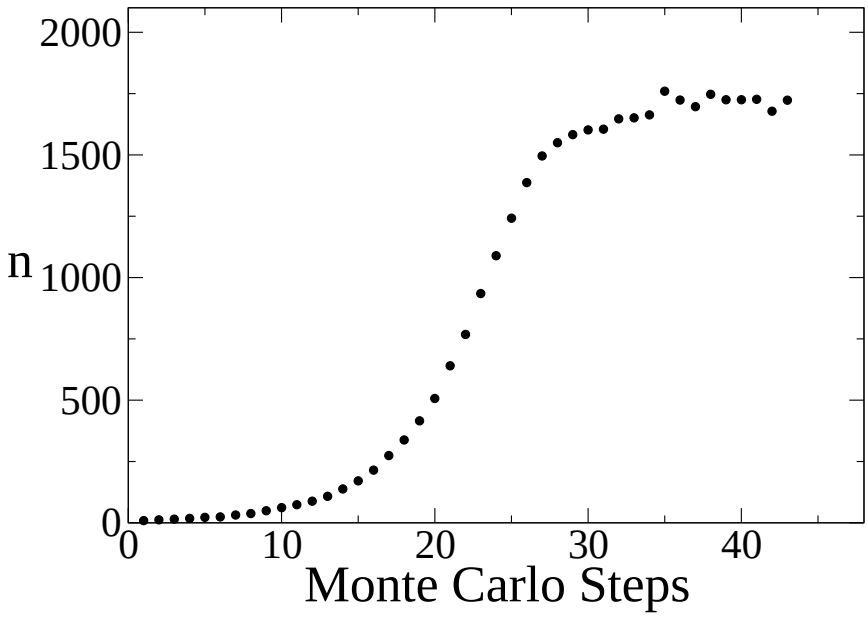

Figure 6.14: Development of n during the equilibrium phase with an equilibrium step number of 10

the amount of Monte Carlo steps. The length of the equilibrium phase was chosen to be 10 MC steps only. But the self adjustment of the truncation M kept restarting the equilibrium phase and thus a total of 43 MC was performed. After 30 MC steps a plateau is reached, indicating that equilibrium is achieved. For confirmation also simulations with 100 and 1000

MC steps as equilibrium phase have been performed and compared to the results shown in Fig. 6.5.3. In Fig. 6.5.3 the development during these three different equilibrium phases is shown. The filled black circles correspond to the plot from Fig. 6.5.3. The red squares refer to a simulation with a 100 MC step long equilibrium phase and the blue triangles to a simulation with 1000 MC steps. The agreement between the three simulations is obvious and thus a long equilibrium phase can be avoided.

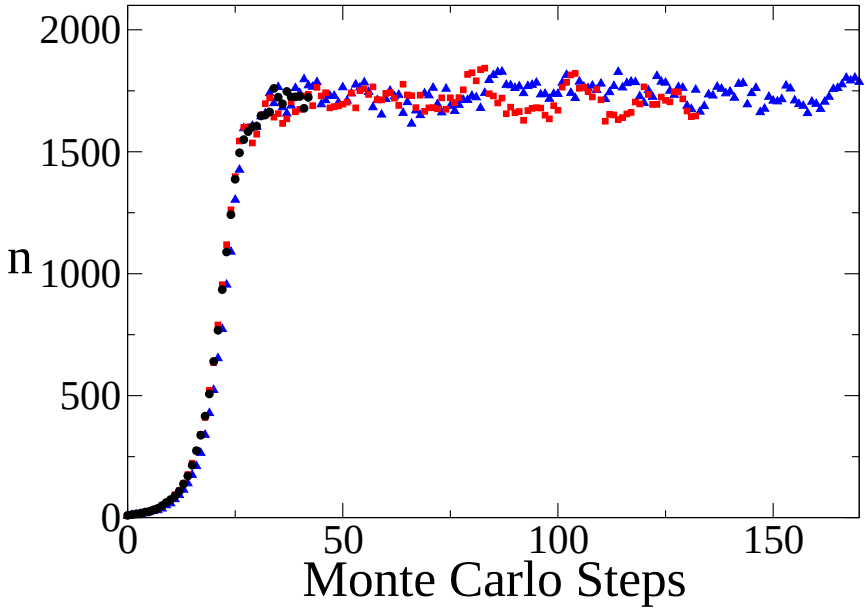

Figure 6.15: Comparison of the different chosen length of equilibrium steps

6.6 Parallelization

Clusters of CPUs or GPUs are standard these days in scientific calculations. Obviously a larger amount of CPUs working on the same problem should lead to a reduction in the calculation time. However, the increase in calculation power does not reduce the runtime linearly as will be shown later. During this PhD work two standards for parallelization were applied on the QMC-SSE code, namely OpenMP [20] and OpenMPI [21]. Despite the similarity of their names, these two standards work completely differently. There is plenty of literature available,[20, 21] so it is sufficient to give a brief overview only.

6.6.1 OpenMP

OpenMP [20] stands for "Open Multi Processoring". The important properties are:

- **Threads are invoked due the master thread**

  One master thread proceeds along the main algorithm. Once it reaches a loop that can be distributed easily among other threads, it invokes sub-threads.

- **Easy to parallelize**

  OpenMP is easy to parallelize, because the main algorithm does not differ much from a single processor code. Especially for MC simulations this is an advantage, since the MC steps can be separated without any problem.

- **Threads Share Memory**

  As long as someone does not want to perform cross printed circuit board (PCB) calculations, this also is an advantage for MC simulations, because the running counters are shared. However, for simulation runs that are supposed to use a few hundred CPUs, OpenMPI is recommended.

6.6.2 OpenMPI

[21] OpenMPI stands for "Open Message Passing Interface". Since the program developed during this work is supposed to run on a grid engine with hundreds of CPUs, OpenMPI was favoured over OpenMP. The important features of OpenMPI are:

- **Threads are invoked simultaneously as independent threads at the start**

  There is no master thread anymore. However, a "rank" gets assigned to every thread. With the help of these ranks certain tasks in the algorithm can be limited to certain threads only.

- **Communication between the threads over an interface (MPI)**

  This is the main feature of MPI. Instead of having a single thread multiplying itself for splitting up the work on different CPUs, each

thread works independently. Variables are not shared anymore, but are transferred over the messaging interface if necessary. Once has to be very careful with timing the messaging processes right. If the threads are communicating too often, it even can lead to a slow down of the overall simulation.

- **Memory is not shared**

  As a result of having many independent threads, their memory is not shared. This allows for cross PBC parallelization and thus in principle simulations on an unlimited amount of nodes.

Note that a difficulty for MC appears in OpenMPI, when a fixed number of update steps is used, since there is no shared memory for a shared counter anymore. During this work it turned out that letting the threads communicate after a certain time instead of a certain amount of MC steps increases the overall speed gain. Further the desired amount of measurements should only be a lower limit for the code and the final measurement number needs to be used for the statistics in the end.

6.6.3 Runtime Scaling

Simulations with identical parameters have been performed for different amount of nodes. The parallelization simply spreads the amount of measurements over the different nodes (advantage of MC simulations). Since every simulation needs first an equilibrium phase, the best theoretical scaling is given by Equ. 6.1.

$$t_{nodes} = t_{equ} + \frac{t_{measure}}{N_{nodes}} \tag{6.1}$$

t_{nodes} corresponds to the real time needed for completing the simulation on N_{nodes} nodes. t_{equ} refers to the time spent in the equilibrium phase, which every thread has to perform. $t_{measure}$ is the total time needed to complete all measurement steps, which are distributed over the different nodes. From Equ. 6.1 the condition for achieving a good runtime performance is obvious. As long as $t_{equ} << \frac{t_{measure}}{N_{nodes}}$ the runtime scales almost directly with the number of nodes. On the other hand, if $t_{equ} \cong \frac{t_{measure}}{N_{nodes}}$ the simulation will actually waste a lot of computation time just with the equilibrium phase. Fortunately the equilibrium is reached quickly (see Sec. 6.5.3) and thus, especially for long calculations of large systems, almost scales with the

number of nodes used. Fig. 6.16 demonstrates the good performance in runtime scaling by plotting the relative runtime (t_{nodes}/t_1) versus the node number. The red squares correspond to the QMC simulations. The black dotted line represents Equ. 6.1. For reference also the physical maximum of $1/N_{nodes}$ (blue dashed line) is plotted.

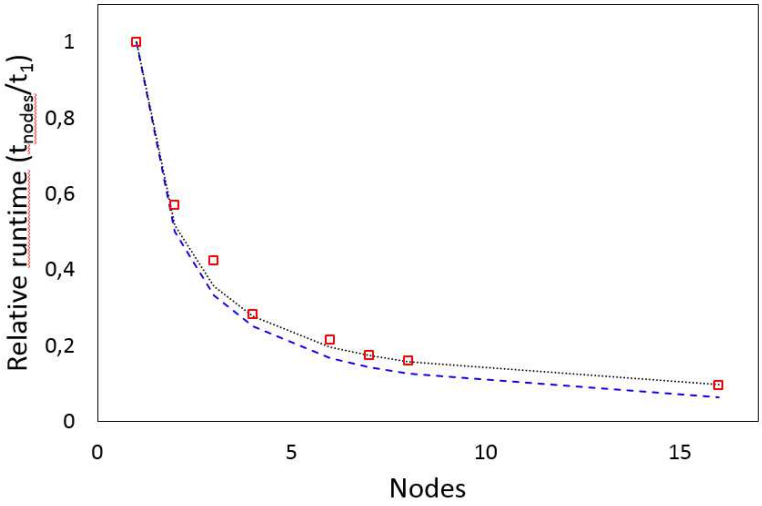

Figure 6.16: Relative runtime against number of nodes.

Chapter 7

Testing the Code

To test the accuracy of the code, simulations of small spin systems have been performed and compared to results obtained to a MATLAB[22] code using the Suzuki-Trotter expansion.[23] This expansion gives analytically correct results, but is limited to very small systems ($N_{Spins} \leqslant 12$). All in this chapter presented results are performed with periodic boundary conditions in x direction and an external field of $H_{ex}/J = 0.1$(except Fig. 7.1). Further only one coupling constant J was used for all spin-spin interactions.
The actual testing was performed on more system parameters than the ones listed here, but a selection for space reasons had to be made.

7.1 Spin Chains

Calculations for anti-ferromagnetic spin chains containing N=4 and N=8 spins have been performed. From these calculations the the energy per spin ($\langle E \rangle / N$) (Fig. 7.1) as well as the susceptibility χ (Fig. 7.1) have been extracted and compared to the ST expansion.

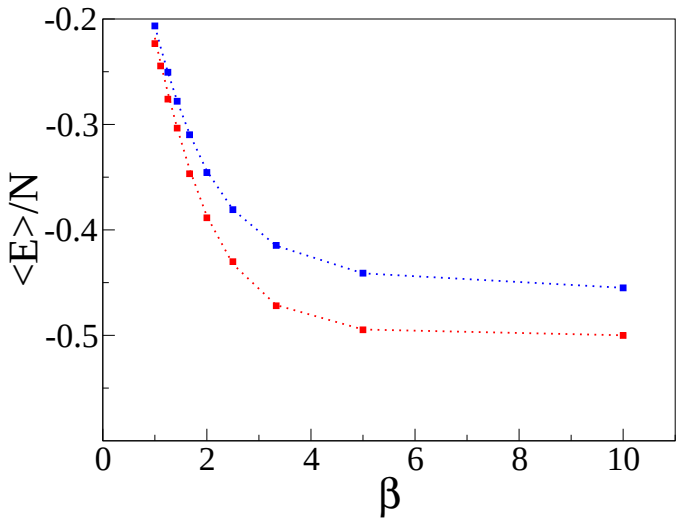

Figure 7.1: $\langle E \rangle / N$ versus the inverse temperature β for AF spins chains containing 4 (red) and 8 (blue) spins. Squares: QMC results. Dotted lines: Suzuki-Trotter expansion.

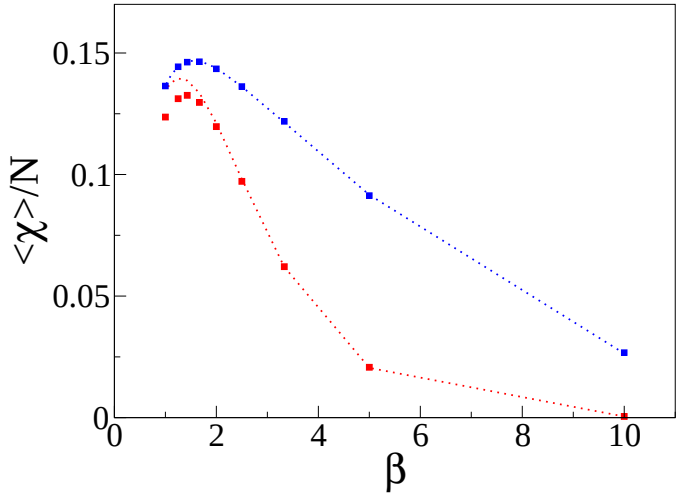

Figure 7.2: $\langle \chi \rangle / N$ versus the inverse temperature β for AF spins chains containing 4 (red) and 8 (blue) spins. Squares: QMC results. Dotted lines: Suzuki-Trotter expansion.

The QMC-SSE results are in very good agreement to the ST expansion. Only at higher temperatures (small β) there is a small divergence for the 4 spin chain, best visible through the susceptibility. The reason is that the energy, and thus also $\langle n \rangle$, is that small, that there are not enough non unit operators entered to sample correctly. In that case it is suggested to add a flip chance of 0.5 to every spin not constrained to any operator in the current state.[24]

To demonstrate that the code also works for different external magnetic fields, additional simulations for $H_{ex}/J = 0.5$ and $H_{ex}/J = 1.0$ have been performed (Fig. 7.1).

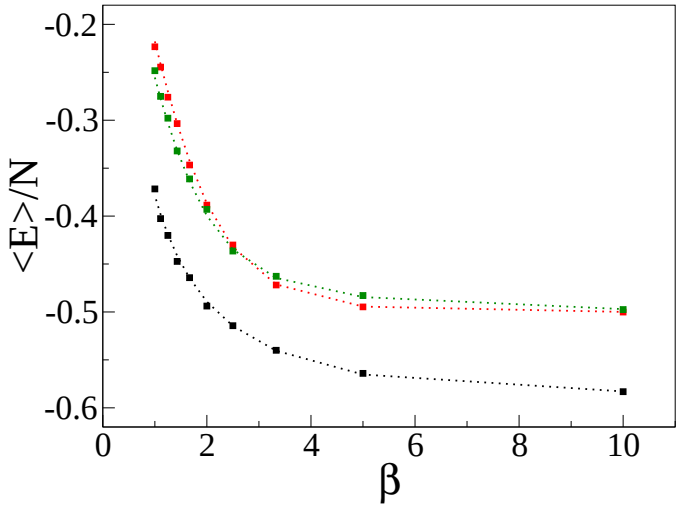

Figure 7.3: $\langle E \rangle / N$ versus the inverse temperature β for AF spins chains with $H_{ex}/J = 0.1$ (red), $H_{ex}/J = 0.5$ (green), and $H_{ex}/J = 1.0$ (black). Squares: QMC results. Dotted lines: Suzuki-Trotter expansion.

7.2 Spin Ladders

Simulations have been performed for spin ladder systems containing 4×2 and 6×2 spins under the same system parameters as for the spin chains before. The results are again in perfect agreement (see Fig. 7.2 and Fig. 7.2).

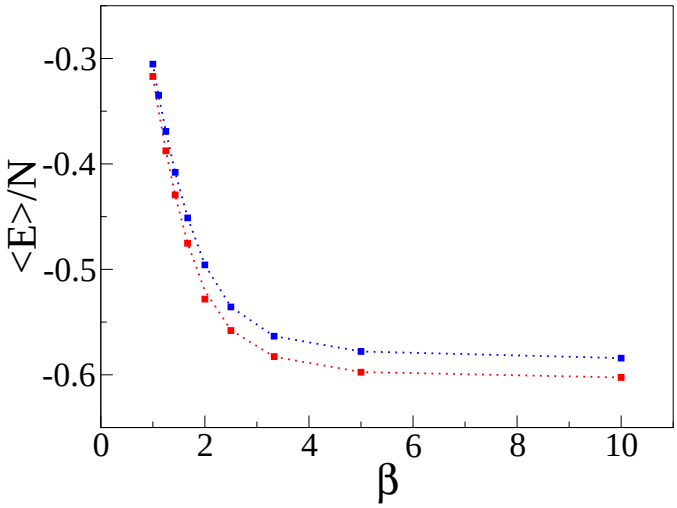

Figure 7.4: $\langle E \rangle / N$ versus the inverse temperature β for AF spins ladders containing 4×2 (red) and 6×2 (blue) spins. Squares: QMC results. Dotted lines: Suzuki-Trotter expansion.

Also simulations for ferromagnetic systems have been performed. They also are in perfect agreement with the ST expansion and thus it is sufficient to show only one ferromagnetic plot (Fig. 7.2).
After proving the reliability of the code, it finally can be applied to study experimentally observed effects.

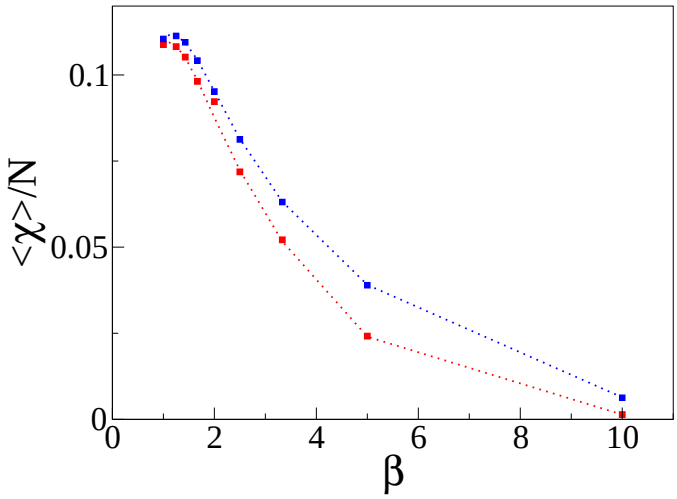

Figure 7.5: $\langle\chi\rangle/N$ versus the inverse temperature β for AF spins chains containing 4×2 (red) and 6×2 (blue) spins. Squares: QMC results. Dotted lines: Suzuki-Trotter expansion.

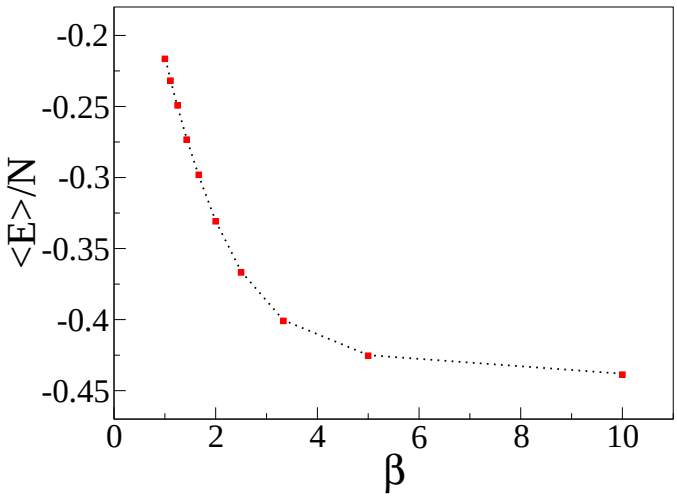

Figure 7.6: $\langle E\rangle/N$ versus the inverse temperature β for a ferromagnetic spin ladder containing 6×2 spins. Squares: QMC results. Dotted lines: Suzuki-Trotter expansion.

Part III

Application - Broadening of the NMR spectra

Chapter 8

Background

8.1 Introduction

$SrCu_2O_3$ is a spin-$\frac{1}{2}$ Heisenberg spin-ladder compound that has been studied intensly both experimentally and theoretically. The crystallographically determined structure[25, 26] consists of planar Cu-O trellis lattices[27] with intercalated Sr ions. These trellis lattices contain the spin ladders which are almost perfectly decoupled due to frustration. It is agreed, that the unpaired electron of the Cu^{2+} ion carries a spin-1/2 and the spin dynamics arises from the Cu-O-Cu interaction via super-exchange over the oxygen ions. The hyperfine interaction couples the magnetic moments of the spins to the nuclear magnetic moments of the Cu ions and in turn influences the local magnetic resonance field. Upon doping with small amounts of non-magnetic impurities e.g. Zn, which occupy Cu sites, a broadening of the Cu NMR-spectrum with decreasing temperature is observed.[28, 29] It is known that an impurity in a single spin ladder causes an exponentially decaying staggered effective local magnetic moment profile around this impurity.[30–38] However, fitting the NMR spectra on the basis of this exponential behaviour requires much larger correlation lengths as compared with theoretical studies of single spin ladders.[39, 40] For a reasonable fit for a spin chain with an impurity concentration of $x = 0.0025$ a correlation length of about $\xi_x \sim 100$ is required.[28] Using a spin-ladder model with a concentration of $x = 0.001 - 0.003$ ξ_x is estimated to be $\sim$ 20 - 50.[29] An exponential decaying cloud model[41, 42] for inter-ladder coupling in one layer ($\sim$exp(-($\xi_x/r_x + \xi_y/r_y$)) and for stacked ladder systems ($\sim$exp(-($\xi_x/r_x + \xi_y/r_y + \xi_z/r_z$)) works well for impurity con-

centrations around $x = 0.02$, but fails to explain the broadening at very small dilutions ($x \leqslant 0.005$). In the present work we perform QMC simulations for single and stacked spin-ladders within the parameter range suggested in the report by Johnston at al.[43]. We find that a coupling to adjacent stacked spin ladders is required to describe the experimentally found low temperature NMR line broadening down to very small impurity concentrations which is consistent with a study on the chain material Sr_2CuO_3.[44]

8.2 Experiment

In his experimental investigation Fujiwara et al. [28] reports about NMR studies on undoped and doped $SrCu_2O_3$. The results are shown in Fig. 8.1. For a doping of $x = 0.0025$ a massive broadening of the Cu NMR

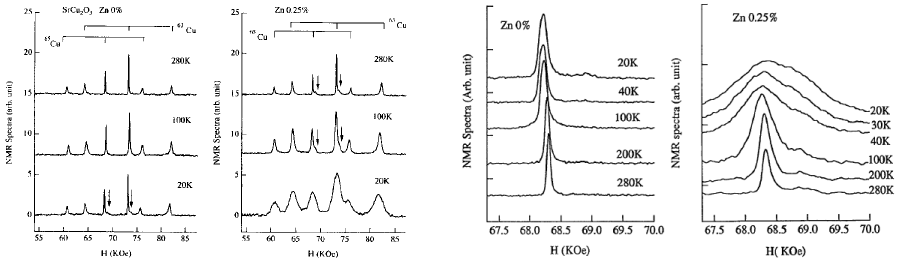

Figure 8.1: Experimental data taken from Fujiwara et al.[28] The left panel shows the effect of the NMR line-width broadening in doped $SrCu_2O_3$ for all spin transitions, while the right panel zooms on the ^{65}Cu central peak.

spectrum at low temperature is observed while in the undoped specimen this effect is almost absent. On the first sight an increasing line-width for decreasing temperature is counterintuitive, which implies that the observed broadening must be due to the temperature dependence of the long range order along and between the spin ladders. Similar experiments have been performed by Ohsugi et al. [29] for $SrCu_2O_3$ and for other spin ladder systems $YBa_2(Cu_{1-x}Zn_x)_3O_{6+y}$,[45, 46] $YBa_2(Cu_{1-x}Zn_x)_4O_8$, [47] and $Bi(Cu_{1-x}Zn_x)_2PO_6$.[48]

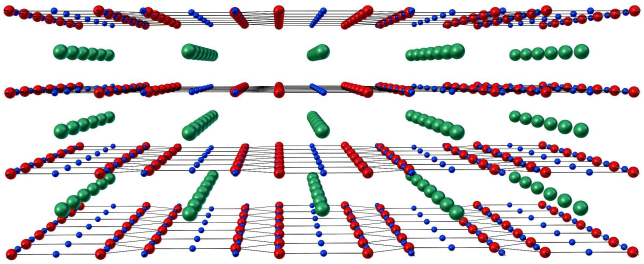

Figure 8.2: $SrCu_2O_3$ structure, blue small balls: O, red middlesized balls: Cu, green larger balls: Sr. — *Made with Blender[49]*

8.3 Structure and Model

The crystallographically determined structure of $SrCu_2O_3$[26, 50**?**] (Fig. 8.2) consists of planar Cu-O trellis lattices with intercalated Sr ions. The unpaired spin-$\frac{1}{2}$ of the Cu ions couple anti-ferromagnetically via superexchange over the intermediate oxygen ions and build the spin ladders. This corresponds to a Heisenberg model with effective coupling constants J_L (coupling in leg direction) and J_R (coupling in rung direction). The anisotropy of these coupling constants is due differences in the electronic structure of the the oxygen ions residing either on a ladder legs or a ladder rung.[51] Fig. 8.3 illustrates the structure of the Cu-O trellis lattice and its containing spin ladders (orange bars). The triangle structure (green triangles) causes a frustration, which effectively leads to an almost perfect decoupling of neighbouring ladders. Thus $SrCu_2O_3$ is known to be a model spin ladder compound. However, other couplings between spins are still possible such as interladder coupling in stacking direction, ferromagnetic diagonal terms within the ladders or ring exchange. A very intensive study on the geometry and the coupling constants was performed by Johnston et al.[43] by fitting the possible models to the experimental susceptibility obtained by Azuma at al.[52]. The most intense study of parameters had been performed for a single ladder and further parameter sets have been studied as a small perturbation of it. Also LDA+U calculations have been performed and the parameters agree within 5% of the fitted ones. To investigate the low temperature broadening caused by impurities it is sufficient to focus on single ladders and stacked ladder systems without diagonal coupling or ring

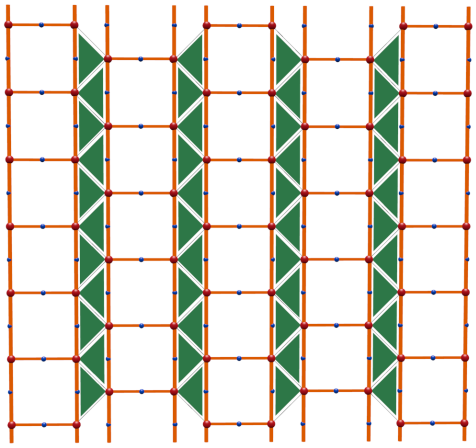

Figure 8.3: Trellis lattice formed by copper and oxygen in $SrCu_2O_3$. Orange bars mark the spin ladders. The trellis structure causes a frustration between neighbouring ladders in plane(green triangles) effectively decoupling the ladders almost perfectly. — *Made with Blender[49]*

exchange, which will be discussed in Sec. 11. The model structure, its nota-

$\frac{J_L}{k_B}(K)$	$\frac{J_R}{J_L}$	$\frac{J_3}{J_L}$
1905(5)	0.488(3)	-
1970(150)	0.48(3)	-
1882	0.471(1)	-
1894(8)	0.5	0.009(4)
1920(70)	0.5	0.01(1)

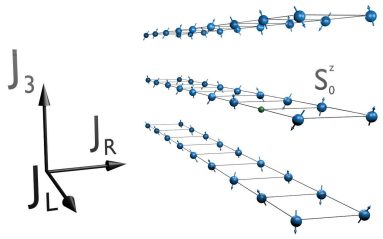

Figure 8.4: Simplified model of $SrCu_2O_3$ with relevant notations. In the table one can see the model parameters obtained by Johnston at al.

tions and the used parameters that are used in this work can be seen in Fig. 8.4. There J_L is the exchange constant along the leg direction (x-axis), J_R along the rungs (y-axis) and J_3 in stacking direction (normal to the Cu-O planes, z-axis). Non magnetic impurities miss an unsaturated spin-$\frac{1}{2}$ and thus can be described as vacancies on the spin-$\frac{1}{2}$ grid (small green ball in Fig. 8.4). S_0^z is the spin on the same rung as the impurity. Further $S_{i,j}^z$ for a single ladder and $S_{i,j,k}^z$ for a stacked ladder system refer to a spin at lattice site i in x-direction , j in y-direction, and k in z-direction. For systems

containing a single impurity only the the origin is chosen so that $S^z_{0,0}$=S^z_0 for single ladders and $S^z_{0,0,0}$=S^z_0 for stacked ladder systems.

8.4 Rung-picture

To describe the impact of an impurity in a spin ladder one considers the case of $J_R \gg J_L$ (or vanishing J_L) which leads to the so called rung-picture, in which the rungs are seen as independent from each other (Fig. 8.5). The

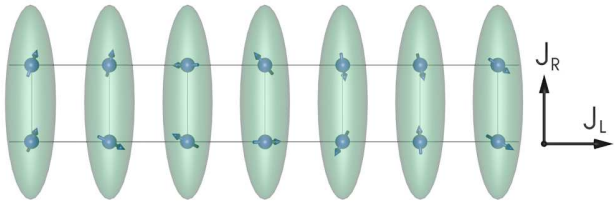

Figure 8.5: Rung-picture in a 2 leg system. All spins are paired up into singlets.

spins of each rung form a singlet separated by a spin-gap of energy $J_R/2$ from the triplet state that prevents the system from responding to a small external magnetic field. Adding an additional ladder leg leaves each rung with an unsaturated spin (Fig. 8.5) and the system can respond even to small external fields. This is the reason why a spin gap can be observed in even leg spin ladders, but not in odd leg spin ladders.[53] By introducing an

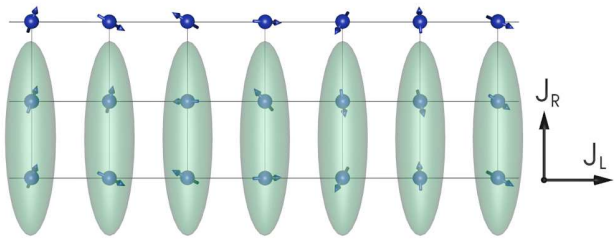

Figure 8.6: Rung-picture in a 3 leg system. In every run one spin remains unpaired.

impurity in an even leg spin ladder one rung remains with an odd number of spins by breaking one singlet up. This leaves a spin-1/2 free (Fig. 8.7) to respond to an external magnetic field (free spin). It turns out that this

mechanism also holds for $J_L \geqslant J_R$ with the difference that the sufficiently large coupling in leg direction causes an effective local magnetic moment profile around the impurity.

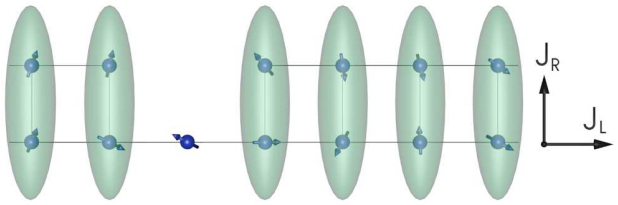

Figure 8.7: Rung-picture in a 2 leg system with 1 impurity represented by a vacancies on the lattice. Because of the impurity one singlet is broken and the 'free' spin will respond to even small external fields.

8.5 Different Representations of a Magnetic Moment Profile

For a better understanding of the upcoming chapters the different representations of spin profiles used in this work are explained in this section. The reason is that different features of the system can be illustrated better for different representations. All plots shown in this section used the same result taken from one QMC calculation and show the local effective magnetic moment profile $\langle S^z_{i,j} \rangle$ versus lattice site. Here i is the lattice coordinate in leg direction and j in rung direction. The data used was taken from a single ladder system with one impurty located at $i = 100$ and $j = 1$. For a better imagination of a magnetic moment profile Fig. 8.8 shows a 3D plot. The red ball illustrates the non magnetic impurity. The green mesh is the local magnetic moment profile. The shape of the gaussian peaks only support the visualization and give no information about a spatial distribution. The tips of the peaks however, correspond to the actual values. The staggered magnetic moment profile can clearly can be seen. Fig. 8.9 shows the same data in two dimensional plots. The left panel is an exact projection of the ladder on the x-z plane. The ladder leg containing the impurity (j=1) is represented by the green squares while the leg with S^z_0 (j=0) is illustrated by the blue triangles. Here the x-axis corresponds exactly to the lattice co-

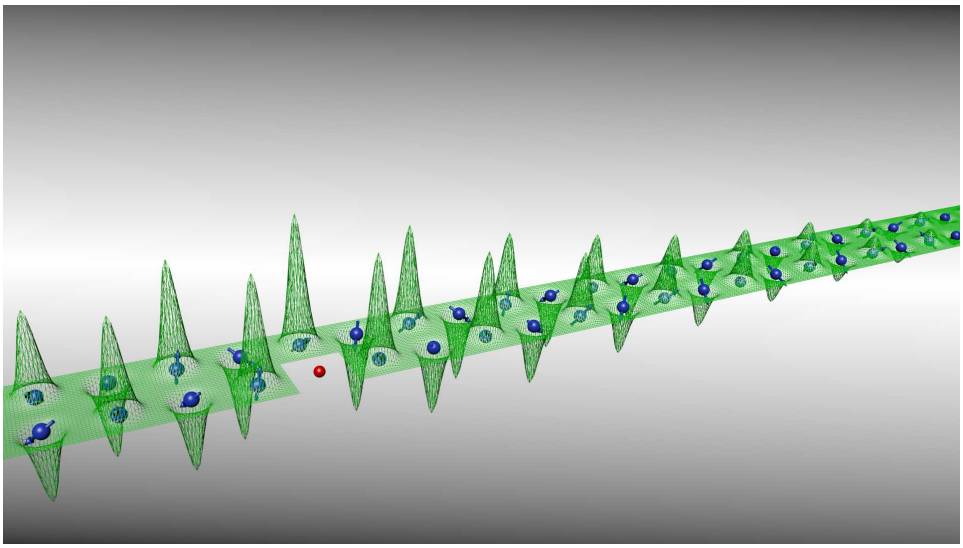

Figure 8.8: 3D Plot of a spin ladder with 1 impurity (red ball). The local effective magnetic moments of the spins (blue) are represented by the tips of the peaks in the green mesh. The shape was chosen for visibility only, but the relative height to each other is correct. — *Made with Blender[49]*

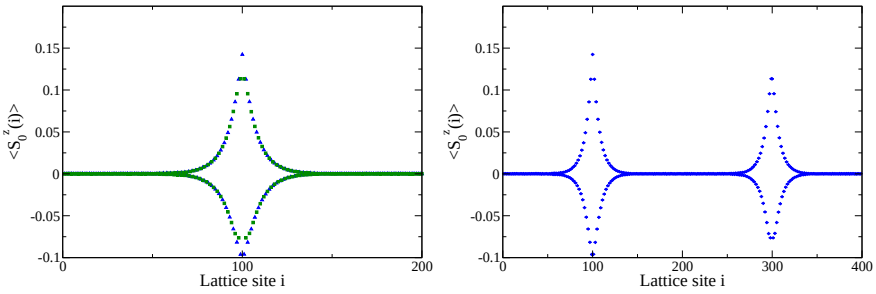

Figure 8.9: Top pannel, bottom pannel.... larger!

ordinate i. The right panel plots both ladder legs consecutively. Note that the x-axis does not correspond to the lattice coordinate i anymore. Lattice sites 1-200 correspond to ladder one and lattice sites 201-399 to ladder 2 (the impurity as a vacancy is not being plotted and thus reduces the lattice sites by one). These type of plots are well suited to get an idea about the NMR spectrum of a system since the magnetic resonance field profile has basically the same shape (see Sec. 8.6). On the other hand these representations are not the best choice when one wants to compare different profiles or find the best parameters for a fit. For that purpose it is better to use absolute values of the magnetic moment profile as is shown in Fig. 8.10. There the left

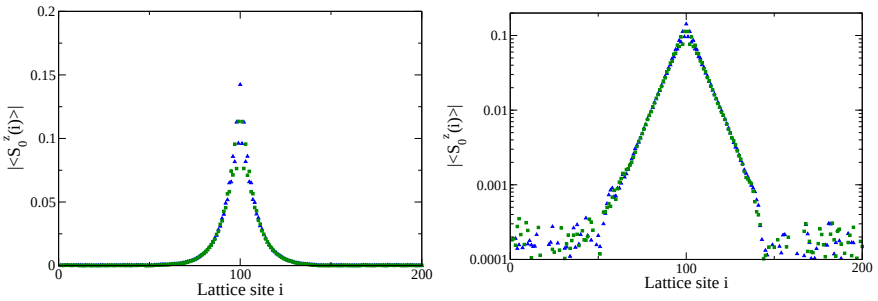

Figure 8.10: Fill out, change left panel for absolute values + consecutively ladders + top pannel, bottom pannel

panel shows the same plot as the right panel of Fig. 8.9, but with absolute values. This is especially useful when looking at the differences in profiles that can be caused by slightly changing one of the system parameters. In the right panel of Fig. 8.10 a logarithmic plot with overlaying ladder legs is used. The logarithmic scale can be used to analyse properties of the system, like the exponentially decaying nature of the magnetic moment profile as well as fitting parameters even at very small values of the effective magnetic moments (see Sec. 11).

8.6 From a Spin Profile to the NMR Spectrum

To achieve the NMR spectrum in experiments a scan of either the external magnetic field H_0 or the radio frequency μ_{RF} is performed. Once the resonance condition (Equ. 8.1) is fulfilled a part of the radiation is being absorbed, which can be measured in a change of intensity behind the sample resulting in the NMR absorption spectrum. Since the absorption intensity obviously depends on the amount of nuclei resonating, the NMR spectrum corresponds to the histogram of resonating nuclei.

$$\frac{\nu_{RF}}{\gamma_N} = H_0 \tag{8.1}$$

In Equ. 8.1 γ_N is the nuclear gyro-magnetic ratio of the probed nuclei. For a system without an impurity the resulting NMR spectrum is a sharp peak with a natural line-width. However, for non vanishing effective moments of the spins the hyperfine coupling between spins and nuclei shifts the local magnetic field at the nuclei, which needs to be taken into account when

applying Equ. 8.1. The resulting resonance condition[54] including the hyperfine coupling then becomes

$$\frac{\nu_{RF}}{\gamma_N} = H_0(i) + A_{HF}\mu_B g\langle S_i^z(H_0(i))\rangle \quad , \tag{8.2}$$

where A_{HF} is the hyperfine coupling (for Cu A_{HF}=-12T/μ_b) and $\langle S_i^z(H_0(i))\rangle$ is the effective local magnetic moment in z-direction of a spin at site i with an external field H_0(i). This 'recursive' relation between $\langle S_i^z(H_0(i))\rangle$ and the external field H_0(i) causes a problem for theoretical studies using intensive calculations. While in principle a scan over the magnetic field range can also be performed in QMC calculations, this procedure would be too cumbersome in practice. However, if the magnetic field dependence of $\langle S_i^z(H_0(i))\rangle$ is known only one calculation at a single resonance field H_{ref} is needed to obtain the whole resonance field spectrum. For small values of (μ_B H_0)/(k_B T) this can be achieved simply by assuming a linear response to an external field

$$\langle S_i^z(H_0(i))\rangle = \langle S_i^z(H_{ref})\rangle \frac{H_0(i)}{H_{ref}} \quad , \tag{8.3}$$

which leads (using Equ. 8.2) to the analytic solution

$$H_0(i) = \frac{\nu_{RF}}{\gamma_N} \frac{1}{1 + A_{HF}\mu_B g \frac{\langle S_i^z(H_{ref})\rangle}{H_{ref}}} \quad . \tag{8.4}$$

For large $\frac{\mu_B H_{ref}}{k_B T}$ the linear approximation is not valid anymore and a hyperbolic tangent relation is used (see Sec. 10.3). The resulting resonance condition

$$\frac{\nu_{RF}}{\gamma_N} = H_0(i) + A_{HF}\mu_B g\langle S_i^z(H_{ref})\rangle \frac{tanh(\frac{\mu_B H_0(i)}{k_B T})}{tanh(\frac{\mu_B H_{ref}}{k_B T})} \tag{8.5}$$

needs to be solved numerically. However, the linear approximation is still useful since it yields a good initial value for the numerical solving procedure. The histogram of the resulting resonance field profile H_0(i) corresponds to the NMR spectrum. To simulate the natural line-width the histogram is smoothened with a gaussian of 0.2T FWHM (Full Width Half Maximum). Fig. 8.11 describes the evolution from an effective magnetic moment profile to its NMR spectrum. The labels on the left y-axis are in units of μ_B and were scaled to fit to their corresponding magnetic field values in Tesla (labels

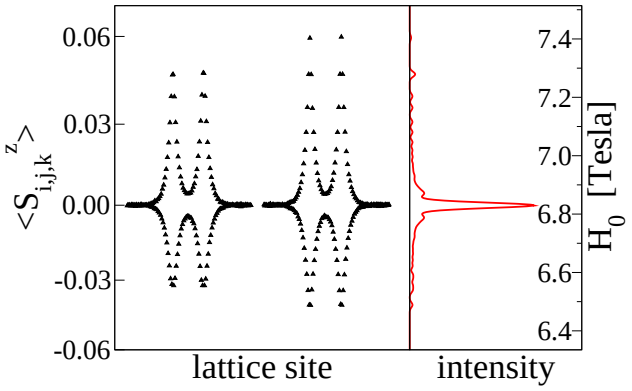

Figure 8.11: Transforming the resonance field profile $H_0(i)$ to a histogram which results into the NMR absorption spectrum. Single ladder system (k=1).

on the right y-axis). This plot provides a good insight on how an effective magnetic moment profile influences the NMR spectra.

8.7 Spin Profile and the NMR Broadening

Before starting with calculations it is worthwhile to discuss the influence of the magnetic moment profile on the NMR spectrum and the requirements to achieve a broadening effect. For that purpose it is suggested to compare the example magnetic moment profile in Fig. 8.11 with its NMR spectrum. While effective magnetic moments of zero build up the main NMR peek non zero moments are spread out on the spectrum in a large range around the main peak. A broadening of the main NMR peak can be achieved by two mechanisms. First of all by reducing the number of spins with an effective magnetic moment of zero. This would simply reduce the height of the main NMR peak resulting in a small increase of the FWHM. Secondly, but more important, is to increase the occupation number of spins with effective magnetic moments in the vicinity of the zero line. Not only this would decrease the height of the main peak by reducing the number of zero moments, but also it increases the height of the NMR line along its slope. This obviously can lead to a strong increase in the FWHM. In other words for a strong broadening effect one has to find a system in which an impurity can influence a lot of spins at once, but only very weakly. This raises some problems for the analysis with QMC as explained in Sec. 9.3.

Chapter 9

Direct QMC Approach

This chapter demonstrates the results of analysing the broadening effect by calculating the NMR spectra directly from QMC results. For that purpose QMC calculations with 1 impurity on a single ladder and on a stacked ladder system within the parameter range given by Johnston at al.[43] have been performed at different temperatures. This direct approach serves well to study the basic properties of single and stacked ladder systems containing an impurity. However, for a more exact description of a real system a better method is needed as discussed in Sec. 9.3.

9.1 Single Ladder with 1 Impurity

To determine whether the influence of an impurity on a spin ladder system has a strong temperature dependence QMC calculations of a single ladder containing 1 impurity are performed at T/J_L=0.02083($\triangleq$ 40K) and T/J_L=0.175($\triangleq$ 334K). The ratio of the system parameters J_R/J_L=0.488 as the best fit for $SrCu_2O_3$ is taken from literature.[43] The system size is 200×2 with periodic boundary conditions along the ladder. Substituting 1 impurity for 1 spin leads to an impurity concentration of 0.25% comparable to the experiment of Fujiwara et al.[28] Also the magnetic field H_{ref}/J_L=0.0037 is chosen according to experiment. The results of these calculations are plotted in Fig. 9.1. At room temperature (right panel) the effective magnetic moment profile consists mainly out of stochastic noise around the zero line. In contrast to that the appearance of magnetic order at low temperature (left panel) is clearly visible. However, the FWHM of the according NMR

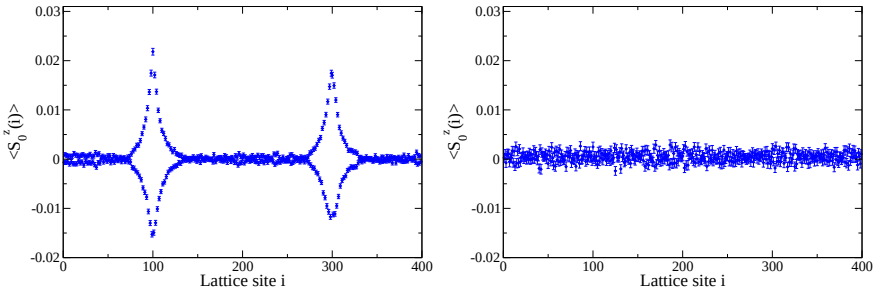

Figure 9.1: Temperature effect of an impurity on a single ladder. Left panel 40 K. Right panel 334 K. JR/JL=0.488 which corresponds to the best fit given by Johnston at al.

spectrum is hardly increased compared to the natural line-width. To cover a larger range of the parameter space and its possible effects on the NMR spectrum a scan of J_R/J_L between 0.4 and 0.6 is performed. In Fig. 9.2 the resulting profiles for different J_R/J_L as well as the corresponding FWHM of the NMR spectra are plotted. Even tough the system parameter ratio J_R/J_L varies quite strongly, the differences in the effective magnetic moment profiles are rather small. The FWHM (inset of Fig. 9.2) shows a small increase for smaller J_R/J_L (because of an increase of the correlation length ξ_x). However, the increase of about 10% is not comparable at all to the experimental increase of about 400-500%. The conclusion of these results is that the large experimental broadening effect cannot be explained on the basis of a single ladder model together with physically reasonable system parameters.

9.2 Stacked Ladder System with 1 Impurity

Calculations with systems consisting out of 6 stacked ladders (100x2x6 with periodic boundary conditions in leg and stacking direction) are performed. As for single ladders the system contains one impurity only, which corresponds to a concentration of $x = 0.08\dot{3}\%$. Note that the impurity concentration is now only $\frac{1}{3}$ compared to the calculations of single ladders. A scan of system parameters within the recommended ranges (J_R/J_L=0.5, J_3/J_L between 0.001 and 0.02) has been performed. The results are plotted in Fig. 9.3. While for small J_3/J_L the stacked ladder system behaves effectively like a single ladder system, the influence on neighbouring ladders increases with

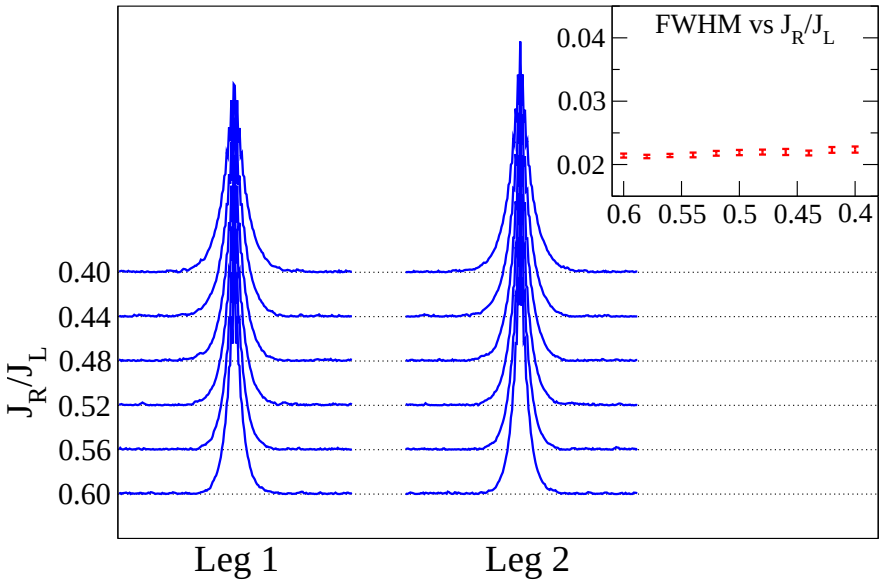

Figure 9.2: Absolute values of the effective local magnetic moments induced by a single impurity (0.25%) for a single ladder for different J_R/J_L. System size is 200 x 2 spins with periodic boundary conditions. $T/J_L = 0.02083$ (comparable to an experimental value of 40K) and $H_{ref}/J_L = 0.01$. Spin distributions for both legs are given, the impurity is located in leg 1. In the inset the FWHM is plotted versus J_R/J_L.

larger J_3/J_L. This influence has a strong impact on the FWHM as can be seen in the inset of Fig. 9.3. Even tough the impurity concentration is only one third compared to the single ladder calculations, a strong broadening effect is clearly visibly at larger J_3/J_L. The cause of this is the unexpected shape the effective local magnetic moment profile on neighbouring ladders. Instead of following a simple exponential decay

$$\sim e^{-\frac{x}{\xi_x}} e^{-\frac{z}{\xi_z}} \tag{9.1}$$

the profile gets more and more smeared out the further the ladder is away from the impurity (see Fig. 9.4). This results in a large amount of non zero effective magnetic moments close to the zero line, which is the requirement of of the desired broadening effect as was discussed in Sec. 8.7. While these results look very promising already they are not representative for real systems yet, because the calculations were limited to systems containing one impurity only. With periodic boundary conditions this corresponds to systems with equally distributed impurities. To simulate a more realistic

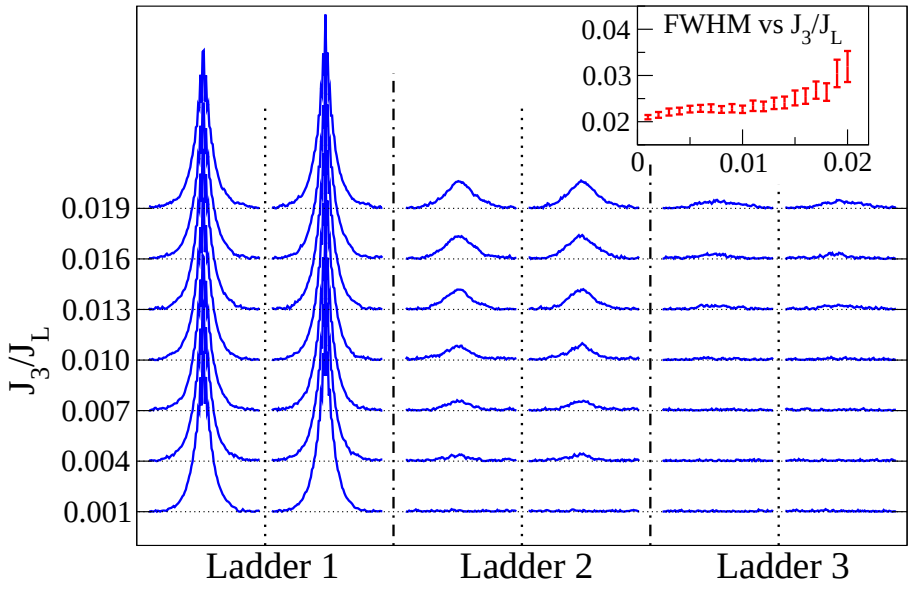

Figure 9.3: Absolute values of the local magnetic moments induced by 1 impurity ($0.08\dot{3}\%$) in a single ladder for different J_3/J_L with $J_R/J_L = 0.5$. System size was $100 \times 2 \times 6$ spins with periodic boundary conditions in leg and z direction. $T/J_L = 0.0208$ ($\triangleq$ 40K) and $H_{ref}/J_L = 0.01$. Due symmetry reasons only 3 ladders need to be plotted. In the inset the FWHM is plotted as a function of J_3/J_L, the increase is easily visible.

system one has to average over many different impurity configurations, which leads to a necessity of a large amount of QMC calculations. Additionally it turns out that the stochastic noise enhances artificially the broadening of the NMR spectra (See Sec. 9.3), which calls for longer QMC runs. Even tough the direct investigation of impurity effects on the NMR spectra with QMC calculation is possible, it is not worth the large amount of computational power required. A more efficient approach will use QMC calculations to study the properties of single impurities and use these results to generate magnetic moment profiles due an analytical model (see Chapters 10 and 11).

9.3 The Bottleneck of QMC in the Direct Approach

Using QMC calculations directly to obtain NMR spectra contains two flaws. First of all the stochastic noise artificially enhances the broadening effect of the NMR central peak. The reason for this lies in the responsibility of ef-

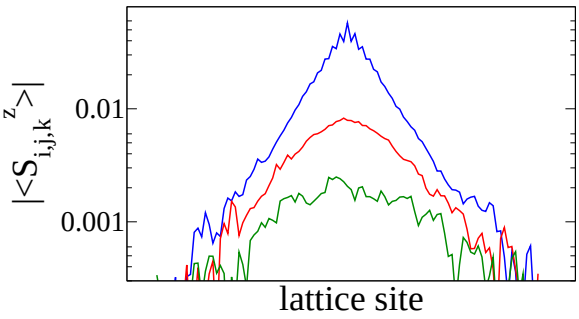

Figure 9.4: Stacked ladders legs are plotted on top of each other to demonstrate the non exponential behaviour found on neighbouring ladders. The blue line represents the ladder containing the impurity, the red line the next neighbouring ladder and the green line the next next neighbouring ladder

fective moments close to the zero line on an increase the FWHM. One has to distinguish which non zero effective moments are caused by the impurity and which ones are caused by the stochastic noise only. Fig. 9.5 demonstrates the influence of the stochastic noise on the FWHM. The left panel

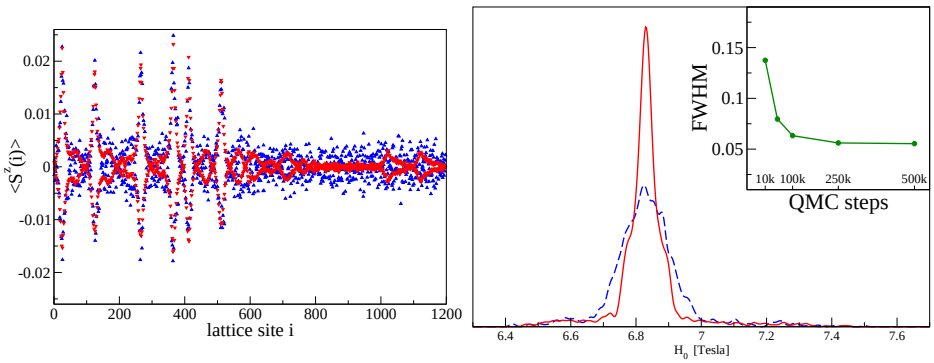

Figure 9.5: Left panel: Effective local magnetic moment profiles for 10k (blue up-triangles) and 500k (red down-triangles) QMC steps. Right panel: Illustration of the influence of stochastic noise on the NMR spectrum for 10k (blue dashed line) and 500k (red solid line) QMC steps. The inset shows the FWHM plotted versus QMC steps

of Fig. 9.5 shows the effective magnetic moment profiles for a short (blue up-triangles) and a long (red down-triangles) QMC calculation of the same system. Their corresponding NMR spectra are shown in the right panel of Fig. 9.5 (blue dashed for the short and red solid of the long QMC calculation). It is clearly visible that the short calculation broadens the FWHM. To prevent obtaining wrong data one needs to reduce the stochastic noise

until its influence on the NMR spectrum vanishes, which is achieved by increasing the QMC steps accordingly (inset of the right panel in Fig. 9.5).We want to emphasise the strong demand for long QMC runs and point ot that short runs cannot be used even for an estimate. While for a single QMC calculation a long run time is not that much of an issue, it leads to a problem when many QMC calculations are needed. This leads to the second and more important problem of the direct approach. While calculations with single impurities have only one possible NMR spectrum, this is not valid for systems with more than one impurity. In the latter systems different impurity configurations lead to different effective moment profiles and thus to different NMR spectra, which is demonstrated in Fig. 9.6. Thus to achieve a

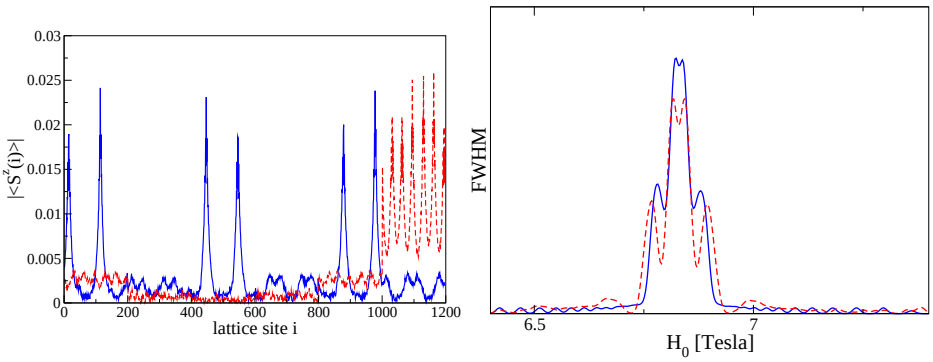

Figure 9.6: Illustration of the influence of impurity configuration. The Solid blue line represents a system with equally distributed impurities while the red dashed line correspond to a system with impurities close to each other. Left panel: Effective magnetic moment profiles. Right panel: Corresponding NMR spectra.

NMR spectrum comparable to a real system, one has to average over many different impurity configurations. For the direct QMC approach this means one calculation for each configuration. Taking the earlier discussed necessity of long QMC runs into account leads to a tremendous increase of calculation time. This "bottleneck" renders a study with the direct approach to be uneconomic and thus calls for a different more effective method of studying impurity effects on NMR spectra (see Chapter 10 and 11).

Chapter 10

Basic Properties of Impurities in Spin Ladder Systems

Even tough the "direct" approach resulted in some promising insights the uneconomically large amount of calculation time needed for simulating systems closer to reality render this method rather ineffective for further analysis. A better approach is to use QMC calculations to analyse the impact impurities have on spin ladder systems with the aim to reproduce effective magnetic moment profiles analytically. This chapter focuses on the first part of the just mentioned approach namely the detailed analysis of effective magnetic moment profiles caused by a low amount of impurities.

10.1 Magnetic Moment Profile induced by a Single Impurity

It is known that an impurity in a single spin ladder causes an exponentially decaying staggered effective local magnetic moment profile around this impurity.[30–38] This exponential decay is governed by the same correlation length ξ_x (in leg direction) as for an undoped system. ξ_x itself depends on the system parameters J_L, J_R, the temperature T/J_L and the impurity concentration. However, it turns out that for the broadening regime $T/J_L \leqslant 0.05$ $\triangleq$100K and for a very low impurity concentration the correlation length ξ_x remains almost constant.[39, 40]. To demonstrate the

exponential decay the effective magnetic moment profile is plotted in Fig. 10.1 on a logarithmic scale for two temperatures. The two temperatures are

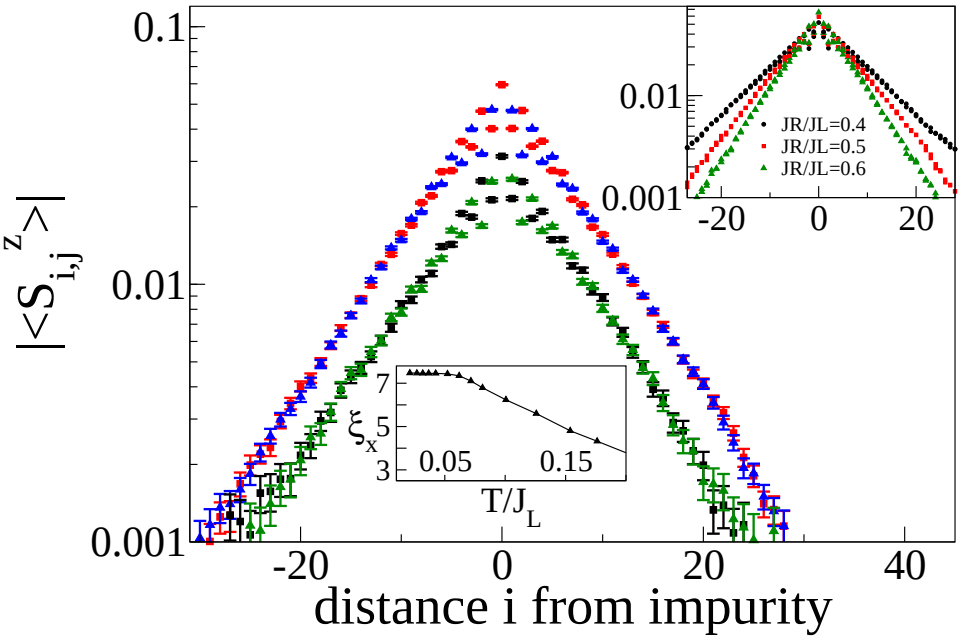

Figure 10.1: Magnetization of a single ladder for $J_R/J_L = 0.5$, $H/J_L = 0.01$ with a single impurity at two different temperatures. Upper curve (red/blue) $T/J_L = 0.02$ ($\triangleq$ 40K), lower curve (black/green) $T/J_L = 0.05$ ($\triangleq$ 100K). The different colours refer to magnetic moments located at the undoped ladder leg (red and black) and for the doped ladder leg (blue and green). For the two temperatures considered the correlation length remains almost constant (lower inset). The upper inset shows the change of the correlation length for different values J_R/J_L. $\xi_x(J_R/J_L)$ becomes 5.9, 7.45, and 9.75 for $J_R/J_L = 0.6$, 0.5, and 0.4, respectively.

chosen to be both below $\mathrm{T/J}_L \leqslant 0.05 \triangleq$100K to illustrate the consistency of ξ_x in this temperature regime. The lower inset plots ξ_x versus $\mathrm{T/J}_L$ taken from Greven et al.[39] The inset in the top right shows different resulting profiles for different ratios of $\mathrm{J}_R/\mathrm{J}_L$ as a result of the changing correlation length ξ_x. Note that with increasing ξ_x and thus increasing expansion of the magnetic moment profiles the maximum at S_0^z decreases.

10.2 Impurity compared to a Free Spin in a Magnetic Field

The reasoning for comparing the effective magnetic moment profile is based on the rung picture (see Sec. 8.4. There an impurity breaks a singlet up and leaves a free spin that can responds even to small external fields. For $\mathrm{J}_R/\mathrm{J}_L \to 0$ a ladder system corresponds to the rung-picture and thus the spin S_0^z on the same rung as the impurity becomes a completely free spin. Because of this congruency of rung picture and spin ladder in the limit $\mathrm{J}_R/\mathrm{J}_L \to 0$ it is reasonable to search for a correlation between the behaviour of a free spin in an external field and the effective local magnetic moment profile caused by an impurity. For a free spin the Heisenberg Hamiltonian

$$\hat{H} = \sum_{i \neq j}^{N} J_{ij}(\hat{S}_i^z \hat{S}_j^z + \frac{1}{2}(\hat{S}_i^+ \hat{S}_j^- + \hat{S}_i^- \hat{S}_j^+)) - \sum_{i}^{N} \mu_B g H_{ex} \hat{S}_i^z \tag{10.1}$$

reduces to the magnetic term only and the expectation value $\langle S_{free}^z \rangle$ depending on the external field H_{ex} and temperature T can be calculated analytically resulting in

$$\langle S_{free}^z \rangle = \frac{1}{2} \tanh \frac{\mu_B H_{ex}}{k_b T} \quad . \tag{10.2}$$

Note that this equation only depends on the ratio of the external field H_{ex} and the temperature T. This also holds for the scaled values used in QMC calculations $h \to H_{ex}/J_L$ and $t \to T/J_L$, because J_L cancels itself in $\mathrm{H}_{ex}/\mathrm{T}$. QMC calculations for different ladder systems are performed for different $\mathrm{H}_{ex}/\mathrm{T}$ and are compared to their corresponding value of Equ. 10.2. A selection of these results are printed in Tab. 10.1. It turns out that for low temperature and systems with a single impurity only the expectation value of a free spin is almost perfectly preserved in the sum of all spin expectation values independent of the system parameters J_L, J_R and J_3. The large deviations at small $\frac{H_{ex}}{T}$ call for a more detailed temperature scan. The results for 3 impurities (last cell in Tab. 10.1) indicate an interaction between impurities, which also makes a study of the spacial distribution of impurities necessary.

N_{imp}	system	$\frac{H_{ex}}{T}$	$\langle S^z_{free} \rangle$	$\sum \langle S^z_i \rangle$	$\frac{\sum \langle S^z_i \rangle}{\langle S^z_{free} \rangle}$
	200x2				
1	$\frac{J_R}{J_L}$=0.4	0.48	0.1558	0.1567	1.0074
	$\frac{J_R}{J_L}$=0.5	0.1	0.0335	0.2563	7.6423
		0.5	0.1619	0.1623	1.0024
		2.0	0.4362	0.4361	0.9997
	$\frac{J_R}{J_L}$=0.6	0.48	0.1558	0.1579	1.0132
	100x2x6				
1	$\frac{J_R}{J_L}$=0.5, $\frac{J_3}{J_L}$=0.01	0.48	0.1558	0.1574	1.0097
3		0.1838	0.0614	0.1891	3.0798
				0.1580	2.5723
				0.1847	3.0074
				0.0628	1.0219

Table 10.1: Free spin in a magnetic field compared to the total magnetization of different systems at different system parameters. N_{imp} is the number of impurities. In the last part ($N_{imp} = 3$) different impurity configurations were simulated.

10.3 Temperature Behaviour of the Total Magnetization

For a detailed temperature analysis QMC calculations are performed for a 200×2 ladder system in the temperature range $0.005 \leqslant T/J_L \leqslant 0.1$. The used system parameters are J_R/J_L=0.5 and H_{ref}/J_L=0.01. To distinguish between an impurity effect and an intrinsic spin ladder property the temperature scan is performed for a system containing only a single impurity as well as for an undoped system. From these QMC results the total magnetization is extracted and plotted versus T/J_L (Fig. 10.2). Two temperature

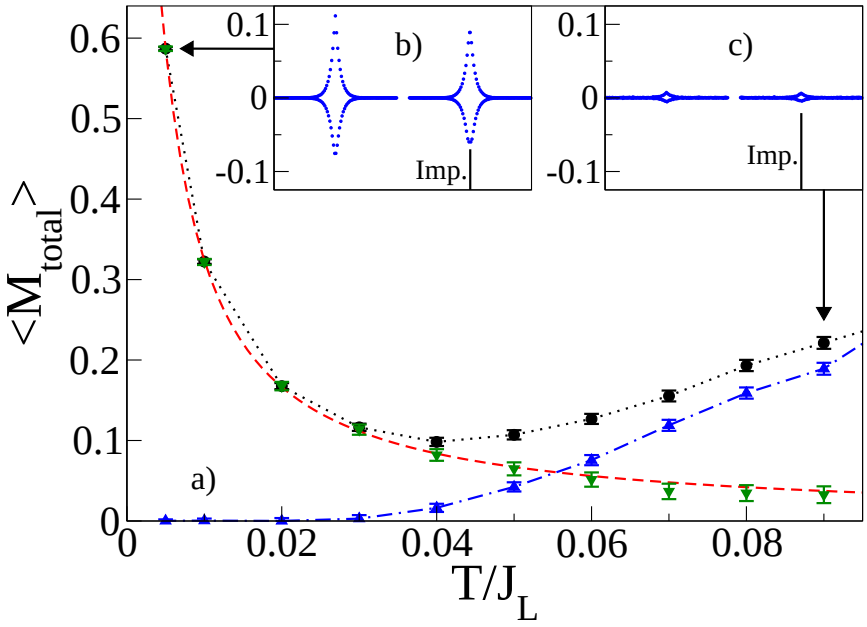

Figure 10.2: a) Total magnetizations versus T/J_L for a system with (blue up-triangles) and without (black circles) an impurity. System parameters: 200 × 2 ladder with periodic boundary conditions in x direction, J_R/J_L = 0.5, $H_{ref}/J_L = 0.005$. To observe the effect caused by the impurity only, the difference between the undoped and doped systems is shown (green down-triangles). The red dashed line describes the analytical solution for a free spin in a magnetic field. In the insets distributions of effective local magnetic moments at b) $T/J_L = 0.005$ and c) $T/J_L = 0.09$ are plotted.

dependent effects with direct impact on the NMR spectrum can be identified. First of all by looking on the undoped system (blue up triangles) the total magnetization raises once the temperature is large enough. Because of

the systems symmetry and thus the equality of all the spins this can only be interpreted as a collective response to an external field according to the susceptibility measured experimentally.[52] Applied to the NMR spectrum this leads to a shift of the main peak towards higher external fields, but the shape of the peak is conserved, which is actually experimentally observed for the undoped system (see the right panel of Fig. 8.1). This is valid also for the doped system (filled black circles), however due the broadening effect at lower temperatures this shift is not that obvious anymore. The second effect with a direct impact on the NMR spectrum is the change of the effective local magnetic moments in the vicinity of the impurity. This effect is rather localized and thus does not cause a shift of the NMR peak, but the local magnetic moment profile appearing (Fig. 10.2 insets *b* and *c*) changes the shape of the NMR signal and thus the FWHM. The total magnetization distributed on the ladder due to doping with a single impurity matches exactly the total magnetization a single free spin would yield. This is demonstrated in Fig. 10.2 by plotting the difference in total magnetization (green down triangles) of the doped and undoped system next to the free spin solution (red dashed line), which shows a perfect agreement. For $SrCu_2O_3$ these two effects occur in neighbouring slightly overlapping temperature regimes, which explains the NMR peak shift towards lower H_0 before, upon further lowering of the temperature, the broadening sets in. With this plot the results for one impurity of table 10.1 are well explainable. Once the temperature is sufficiently small the collective excitation vanishes and the system follows the *tanh* behaviour (ratios 1.0 in table 10.1). For larger temperatures the collective excitation raises the total magnetization further, independently of the impurity, which leads to a factor greater than 1 (ratio of 7.6423 in table 10.1). The in this section obtained results for a single spin ladder also hold for stacked ladder systems. For validation this is demonstrated in Fig. 10.3 by plotting the effective magnetic moment profiles of a stacked ladder system ($200\times2\times8$) for two different temperatures. Black dots show the results of a QMC calculation at T/J_L=0.175≙334K and green dots a QMC calculation at T/J_L=0.02083≙40K. Because of the overlaying plot, both effects are visible. For low T/J_L (green dots) a magnetic moment profile is formed symmetrically around the zero line. For high T/J_L (black dots) the collective response to the external field slightly shifts the almost flat magnetic moment profile above the zero line.

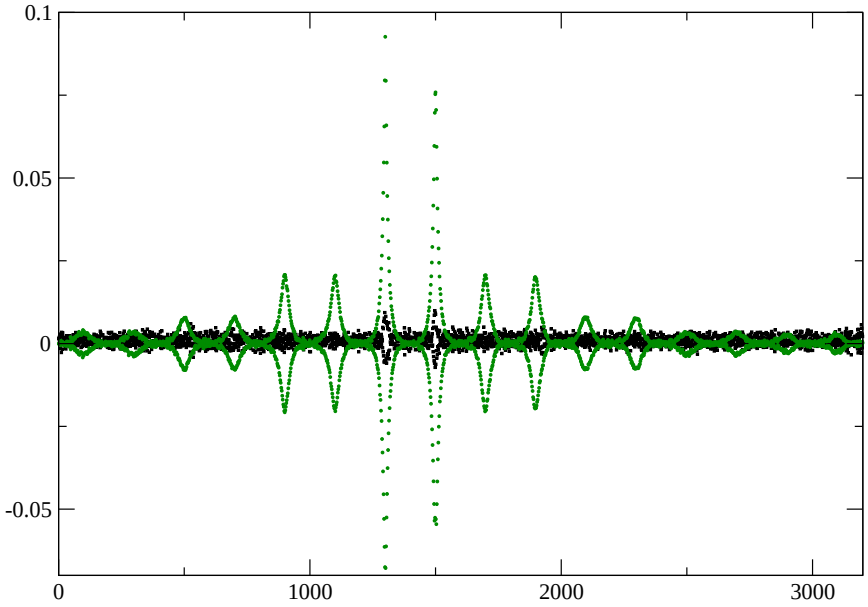

Figure 10.3: Effective local magnetic moment profiles for a 200 × 2 × 8 stacked ladder system with periodic boundary conditions in x and z directions for two different temperatures. System parameters used are J_R/J_L = 0.4, J_3/J_L = 0.02 and H_{ref}/J_L = 0.01. Green dots (T/J$_L$=0.01) show the raise of effective local magnetic moments around the impurity while black dots (T/J$_L$=0.111) show the collective response to an external field.

10.4 Temperature Behaviour of the Effective Local Magnetic Moments

While the total magnetization induced by an impurity does not depend on the exchange integrals J$_L$, J$_R$, and J$_3$, the expansion of the "spin cloud" forming around its impurity does. For larger J_R/J_L and thus smaller correlation length ξ_x (for stacked ladders smaller ξ_z for larger ratios of J_R/J_3) the spin cloud becomes more localized and vice versa. While in general the correlation length depends on temperature and dilution[39, 40] it remains nearly constant in the temperature regime where the broadening effect is observed and in the limit of low impurity concentrations. Thus, not only the total magnetization of the whole system, but also the effective local magnetic moments show a hyperbolic tangent behaviour. One can obtain an analytical description of the effective local magnetic moments (see Equ. 10.3) by introducing a fit pre-factor A(ξ)=A(J$_R$/J$_L$) and taking the expo-

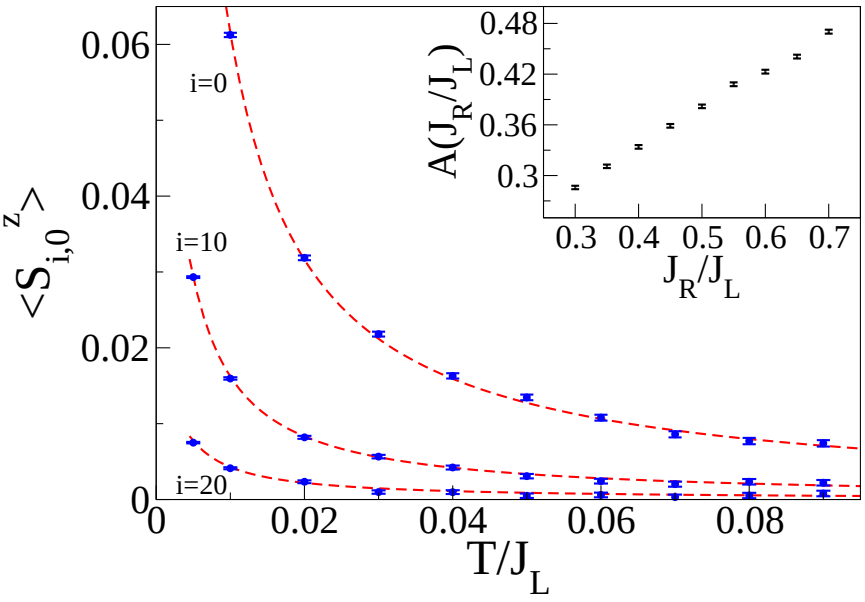

Figure 10.4: Effective local magnetic moments of the spins opposite of the impurtiy (S_0^z), at a distance of 10 lattice sites (i=10) and 20 lattice sites (i=20) versus T/J_L. The dashed lines correspond to a free spin in a magnetic field times a proportionality factor. System parameters: 200 × 2 ladder with periodic boundary conditions in x direction, $J_R/J_L = 0.5$, $H_{ref}/J_L = 0.005$

nentially decaying nature of the staggered magnetic moment profile into account.

$$\langle S^z_{i,j}(T)\rangle = A(\xi)(-1)^{|i+j|}e^{-\frac{|i|}{\xi_x}}\frac{1}{2}\tanh(\frac{\mu_B H_{ref}}{k_B T}) \qquad (10.3)$$

The pre-factor A(ξ) is determined by scaling down the solution of the free spin (Equ. 10.2) to fit $\langle S_0^z\rangle$, which is obtained through a QMC calculation at a chosen T/J_L. Fig. 10.4 shows a comparison between (Equ. 10.3) and QMC results for three different lattice sites. $A(\xi)$ has been extracted from one QMC simulation at S_0^z and $T/J_L = 0.005$. In the broadening temperature regime ($\xi \sim$ const.) the analytical descriptions (dashed lines) fit perfectly to the QMC calculations. This also holds for stacked ladders if the correct magnetic moment profile is applied (see Sec. 11). In the inset of Fig. 10.4 the pre-factor $A(J_R/J_L)$ is plotted versus J_R/J_L. The smaller J_R/J_L (and thus larger ξ_x) the smaller is also the maximum of the spin profile $\langle S_0^z\rangle$. This is a result of the spacial distribution of the impurity induced spin cloud, which gets less localized at larger correlation lengths. It has to be mentioned that for systems in which ξ shows a pronounced

temperature dependence the description given in Equ. 10.3 is only valid for $\xi \to \xi(T)$ and thus $A(\xi) \to A(\xi(T))$. Then QMC simulations are needed for every temperature step.

10.5 Magnetic Field Dependence

To investigate the magnetic field dependence of a magnetic moment profile QMC calculations of a ladder with a single impurity for different magnetic fields H/J_L and fixed temperature are performed. Fig. 10.5 compares the QMC results (blue triangles) for the total magnetic moment of the ladder to the free spin solution Equ. 10.2 (red dashed line). For small

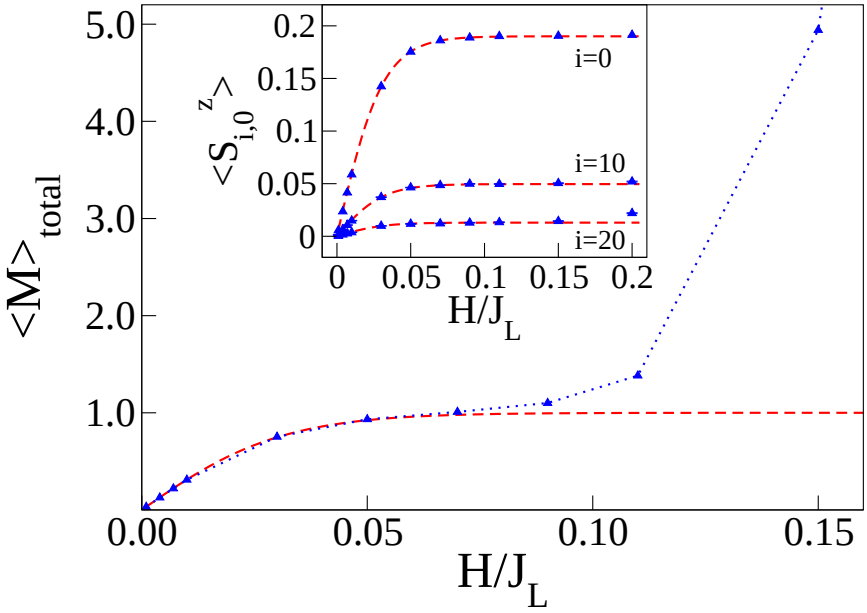

Figure 10.5: Total magnetization versus H/J_L for a system with a single impurity (blue up-triangles). System parameters: 300 × 2 ladder with periodic boundary conditions in x direction, $J_R/J_L = 0.5$, $T_{ref}/J_L = 0.02083$. The red dashed line corresponds to the solution of a free spin in a magnetic field. The inset compares Equ. 10.3 with the QMC results for $\langle S^z_{i,0} \rangle$.

fields ($H/J_L \leqslant 0.07$) the QMC results match the free spin solution perfectly. Above $H/J_L = 0.07$ (corresponding to an applied magnetic field of about 200 Tesla) the magnetization starts to rise significantly, which indicates that the applied magnetic field is large enough to break up the singlets, thus producing an additional magnetization. However, in our simulations magnetic

fields never exceed $H/J_L = 0.01$ so that Equ. 10.3 is valid in the magnetic field range. The inset shows the QMC results for the local spins (blue up-triangles) opposite of the impurity (i=0) and at distant sites i=10 and i=20 in comparison to the solution given by Equ. 10.3 (red dashed line).

10.6 Multiple Impurities

10.6.1 Well Separated Impurities

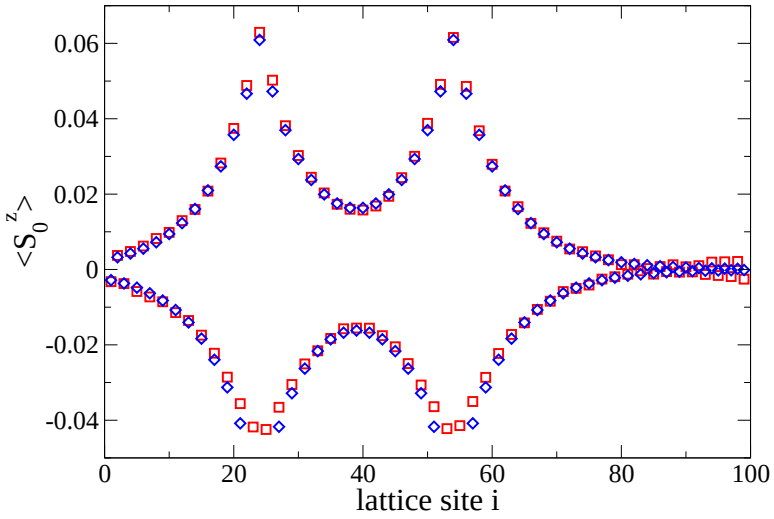

Figure 10.6: Demonstration of how well superimposing magnetic moment profiles of single impurities can describe the profile caused by two impurities. Red squares: QMC results of a single ladder system containing two impurities with a distance of 30 lattice sites. Blue diamonds: Assembled magnetic moment profile obtained by superimposing two single impurity profiles with a distance of 30 lattice sites.

The existence of more than 1 impurity can have an impact on the total magnetization of the system (see table 10.1 bottom row). Since impurities induce a rather localized effective magnetic moment profile around themselves an assumption can be made right away. Obviously impurities separated sufficiently from each other (larger than the expansions of their induced spin clouds) can be seen as independent and thus the total magnetization they induce will result in the free spin solution times the impurity number, which is validated in the bottom row of table 10.1 for the values of ∼3.0. The interaction of closer impurities needs more analysis. In first order approxi-

mation the resulting effective magnetic moment profile caused by impurities with overlapping induced spin clouds can be described by a superposition of two independent magnetic moment profiles, which is demonstrated in Fig. 10.6. There the magnetic moment profile for a single ladder containing two impurities is compared to a profile created by superposing two single impurity profiles using the same impurity distance. However, to understand the reduction of the total magnetization in the bottom row of table 10.1 the concept of "sublattices" needs to be introduced.

10.6.2 Sublattices

A sublattice consists out of all lattice positions that prefer the same spin orientation. Thus all spins on a sublattice form a ferromagnetic lattice. For our anti-ferromagnetic model this applies to every second lattice site resulting in two sublattices illustrated in Fig. 10.7 Applying this picture on overlapping

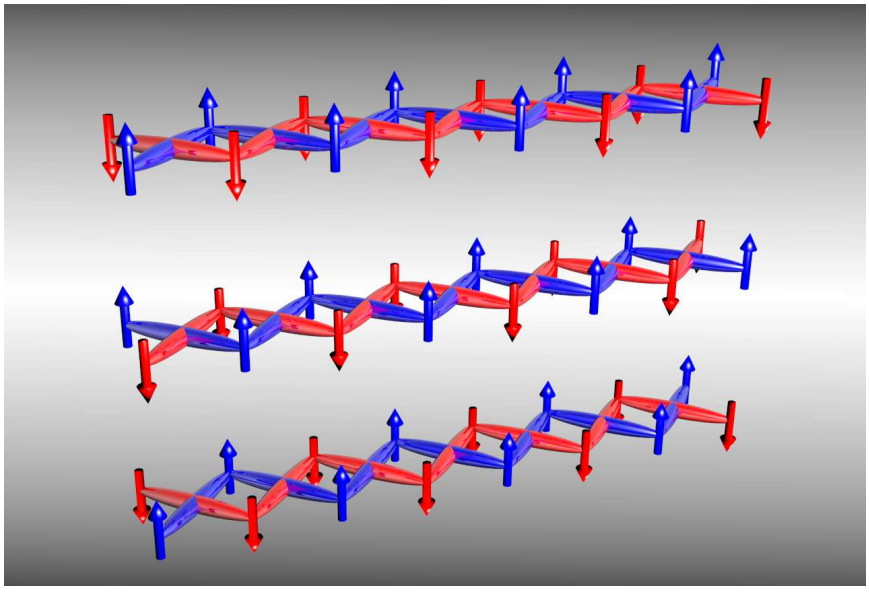

Figure 10.7: Illustration of the two different ferromagnetic sublattices (blue up arrows, red down arrows) that combined build up the anti-ferromagnetic spin system. — *Made with Blender[49]*

spin clouds leads to two cases. First there is the case when impurities are an even amount of lattice site apart (from now on will be referred as "same sublattice"). In this case only magnetic moments with the same sign interact, which on first sight does not change the total magnetization. The other case

describes impurities with an odd number of lattice sites apart. In this case all interacting spins have opposite sign resulting in a weakening of both spin clouds. This explains the at first sight surprising values of the bottom row of Table 10.1. The value of about 2.57 corresponds to two slightly overlapping spin clouds based on different sublattices. For the value of about 1.02 two impurities are close enough to completely annihilate each others spin cloud leaving only the magnetic moment profile of the third impurity.

10.6.3 Close Impurity Interaction

While for far and medium-close impurities the picture of superimposed spin clouds works well it is not valid anymore once the impurities reside within each others spin cloud. In this case the two different S_0^z are close enough to directly "feel" and thus interact with each other. This interaction can be approximated by a two particle Heisenberg system with a distance dependent effective coupling (see Equ. 10.4).

$$\hat{H} = J_{eff}(d)\overrightarrow{S_1}\overrightarrow{S_2} \quad , J_{eff}(d) = C \times e^{-\frac{d}{\xi_x}} \quad , \tag{10.4}$$

where the constant C is a fit parameter. The correlation length xi_x is taken from a QMC calculation. This approximation holds well as long as the distance is sufficiently large for the ladder to behave 1-dimensional. In Fig. 10.8 $\langle S_0^z \rangle$ for different models is plotted versus the impurity distance for different system parameters $\mathrm{J}_R/\mathrm{J}_L$. The black bars represent the directly obtained QMC results. The red down triangles correspond to the 2 particle Heisenberg system with an effective coupling with C fitted to the QMC results. The difference between those two data sets is caused by a too small impurity distance so that the ladder does not effectively behave like a 1-dimensional system anymore. The blue dotted line results from superimposing two single impurity profiles and shows are large deviation compared to the directly obtained QMC data. Also calculations with stacked ladder systems have been performed and lead to the same result with the addition that impurities on different ladders can always be described by a simple superposition. The reason for this seems to be the extremely weak coupling in stacking direction. In summary, the effective magnetic moment profile caused by more than one impurity can be described by a superimposition of single impurity profiles as long as impurities do not reside on the same ladder within each

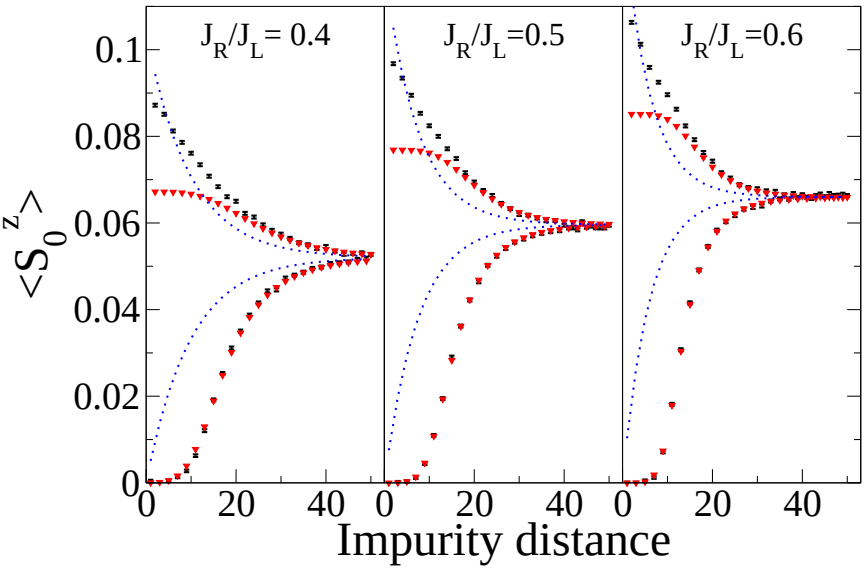

Figure 10.8: $\langle S_0^z \rangle$ for different models plotted versus the impurity distance for different system parameters J_R/J_L. The three models are direct QMC calcultion (black bars), two particle Heisenberg system with effective coupling J_{eff} (red down triangles) and a superposition of single impurity profiles (blue dotted line).

others spin cloud.

10.7 System Parameters and ξ_x

Johnston at al. [43] performed the parameter scan for stacked ladder system at a fixed ratio J_R/J_R=0.5. However, small changes of the correlation length ξ_x can already influence the FWHM of the NMR spectra. To investigate if small perturbations of J_R/J_R=0.5 could lead to an enhanced or weakened FWHM a scan of ξ_x in the parameter range $J_R/J_L = 0.4 - 0.6$ has been performed for a single ladder. It turns out that within this parameter range ξ_x changes linearly with the inverse of this ratio, namely J_L/J_R, shown in Fig. 10.9.

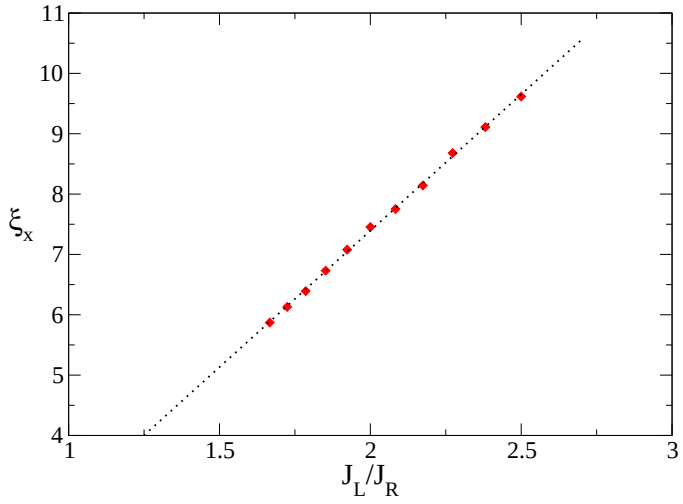

Figure 10.9: ξ_x vs J_L/J_R

Further calculations for different J_3/J_L have been performed to analyse the influence of J_3/J_L on the correlation length ξ_x. In Fig. 10.10 J_3/J_L scans for two different ratios of J_L/J_R are plotted. ξ_x increases for about 10% if

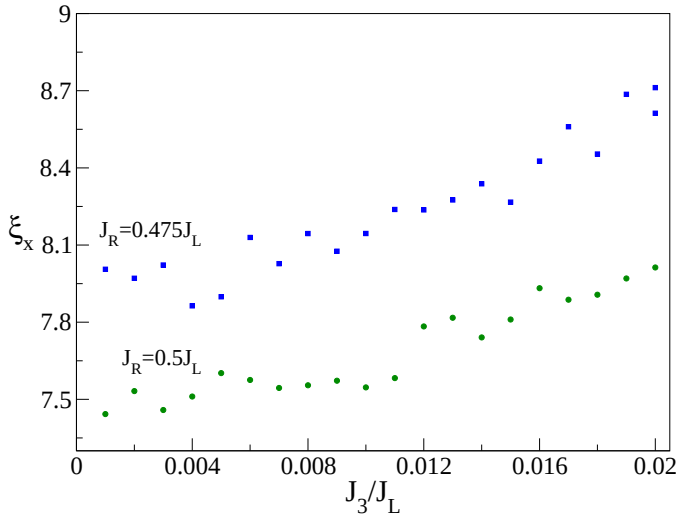

Figure 10.10: ξ_x vs J_3/J_L for two different values of J_L/J_R.

a single ladder system system (J_3/J_L=0) is compared to a stacked ladder system coupled with J_3/J_L=0.02. Thus a larger coupling in stacking direction does not only increase the number of lattice sites affected by influencing additional ladders, but also flattens the magnetic moment profile on the impurity inhering ladder, leading to an enhancement of the FWHM.

Since small adjustments in J_R/J_L and J_3/J_L influence ξ_x and thus the FWHM of the NMR spectra sufficiently large a detailed analysis of the system parameters J_R, J_L, and J_3 could lead to an overall improved result. However, this work focuses on the qualitative description of the low temperature broadening effect only. Improved quantitative results due system parameter adjustment could be a motivation for future works.

Chapter 11

Analytical Fit using QMC Results

This chapter explains how the obtained effective local magnetic moment profiles from QMC simulations can be described analytically. The resulting analytical profiles are not influenced by a stochastic noise and thus do not artificially enhance the temperature dependent broadening effect. In addition to that many profiles resulting from different impurity configurations can be generated quickly. The whole procedure from obtaining the parameters for the analytical fit from a small amount of QMC simulations until generating realistic NMR spectra is explained at the end of this chapter.

11.1 Single Ladders

For single ladders, the effective local magnetic moment profile induced by an impurity can be almost perfectly described with a staggered exponentially (with ξ_x) decaying function which was already described in earlier (Equ. 10.3) as

$$\langle S^z_{i,j}(\frac{H_{ref}}{T})\rangle = A(\xi_x)(-1)^{|i+j|}e^{-\frac{|i|}{\xi_x}}\frac{1}{2}\tanh(\frac{\mu_B H_{ref}}{k_B T}) \quad .$$

This equation only uses two parameters, namely ξ_x and $A(\xi_x)$. ξ_x can be extracted directly from a QMC calculation. $A(\xi_x)$ can be obtained by solving

equation Equ. 10.3 at $i, j = 0$ for $A(\xi_x)$, which results in

$$A(\xi_x) = \frac{\langle S_0^z \rangle}{\frac{1}{2} tanh \frac{\mu_b H_{ref}}{k_b T}} \quad . \tag{11.1}$$

$\langle S_0^z \rangle$ is the expectation value of the spin opposite of the impurity and can be directly taken from a QMC simulation. In Fig. 11.1 an effective magnetic moment profile is compared with Equ. 10.3 to illustrate the quality of this analytical description. The only deviations are within the first few lattice sites around the impurity, which only have an impact on the edges of the NMR spectrum (see sec. 8.6). Since the broadening effect is caused by effective magnetic moments with a small deviation from zero only, this analytic description renders to be a valid tool for the purpose of this work.

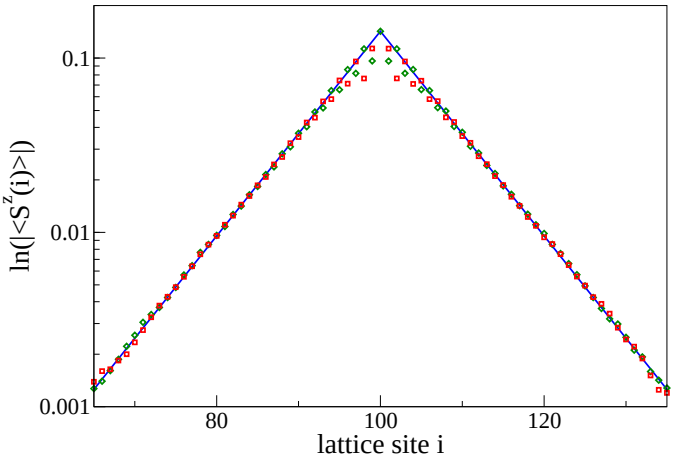

Figure 11.1: Comparison between the analytical description and the QMC result.

11.2 Same Function for Both Ladder Legs?

Fig. 11.1 demonstrates that the absolute values of both ladder legs follow the same function once a certain distance from the impurity is reached. For better understanding Fig. 11.2 uses a color code to illustrate the interaction between the two legs. On the left side of the two plotted ladders are two different fixed values represented by the blue and yellow balls. Because of correlations along and between the ladder legs the two former different values effectively average into a uniform one represented by the dark green

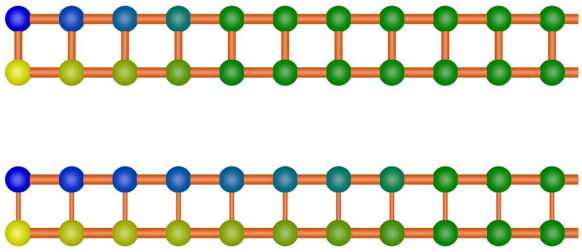

Figure 11.2: Illustration of why and how two legs can be described with the same function. The different thickness in the orange bonds represents the different coupling strength of the ladders.

balls the further away from the initial fixed values. Furthermore the stronger the legs are correlated the less lattice sites are necessary to achieve equality as illustrated in Fig. 11.2. This picture can very well be applied to a spin ladder. The different initial fixed values (blue and yellow) can be seen as the different effective local magnetic moments at the rung containing the impurity. The next few lattice sites towards the right correspond to the spins in the close vicinity of an impurity. The mixing there was not sufficient enough yet to average the difference out, which explains the deviations in Fig. 11.1 in the close vicinity of the impurity. However, with increasing distance the difference of the legs becomes smaller until the effective moments on the two different legs converge onto the same curve corresponding to Equ. 10.3. Since the coupling in rung direction ($J_R/J_L \sim 0.5$) is strong only a few latice sites are needed to achieve the equality of the legs.

11.3 Stacked Ladder Systems

In Sec. 9.2 was shown that for stacked ladders the profile is more and more smeared out the larger the distance in stacking direction is (Fig. 9.3), which cannot be described by a simple exponential cloud. Applying again the color picture from the last section (Sec. 11.2) helps to understand why. (I) while for a single ladder only two rows of lattice sites are mixing far more lattice sites are involved in stacked stacked systems. (II) the coupling in stacking direction is rather small. The large difference of the coupling constants within the ladders and in stacking direction (J_R,$J_L \gg J_3$) can be interpreted as a stronger correlation within a ladder than in stacking direction. Thus for the impurity inhering ladder the magnetic moment profile looks similar

to the one of a single ladder. The next neighbouring ladder does not see the impurity only, but the whole ladder profile of the former ladder. Then, with the stronger correlation within that neighbouring ladder, the profile will be smeared out more. This is repeating for every further neighbouring ladder. Fig. 11.3 illustrates the mixing for a stacked system by starting with a fixed bottom row containing balls of different colors, which represents the impurity inhering ladder. Every color value of a ball on a neighbouring ladder is achieved by averaging (with distance weighting) over five balls sitting on the former ladder. That way the strong initial color profile (bottom row) gets more and more smeared out there further away from the initial row, similar as was shown earlier in Fig. 9.3.

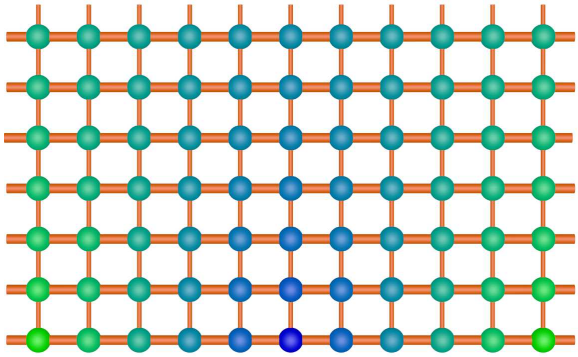

Figure 11.3: Illustration of a stacked ladder system due color mixing. The bottom row has its values fixed while every other ball corresponds to the average of the closest five balls from the row below.

The comparison with color mixing gives a nice explanation for the flattening of the profiles in stacking direction, but one has also to be sure that the influence of periodic boundary conditions in stacking direction can be excluded. For that purpose QMC calculations have been performed using the parameters from Johnston et al. [43]. In Fig. 11.4 the absolute effective magnetic moments $|\langle S^z_{0,0,k}\rangle|$ are plotted for different J_3/J_L in stacking direction derived from QMC calculations for 8 stacked ladders. Please note that for stacked ladders the position of the spins depend also on a stacking index k so that $S^z_{i,j} \rightarrow S^z_{i,j,k}$. With increasing J_3 the deviation from a simple exponential decay increases. This effect is shown in the inset of Fig. 11.4 where $|\langle S_{0,0,k}\rangle|$ is compared with a *hyperbolic cosine* for $J_3/J_L = 0.02$. At distant ladders the deviation from the *hyperbolic cosine* behaviour increases.

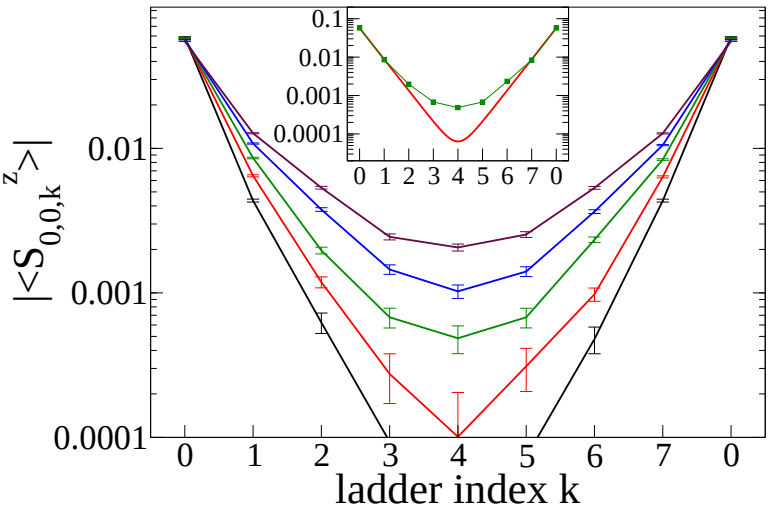

Figure 11.4: $|\langle S_{0,0,k}\rangle|$ for a stacked ladder system (k=0,1,2,...,7) with periodic boundary conditions. $J_R/J_L = 0.5$, $H_{ref}/J_L = 0.01$, $T/J_L = 0.02083$ and (from bottom to top) $J_3/J_L = 0.01, 0.015, 0.02, 0.025, 0.03$. The inset compares the QMC results for $J_3/J_L = 0.02$ with a *hyperbolic cosine* to demonstrate the non exponential behaviour.

It thus becomes obvious that a simple exponential cloud model cannot be used to describe the complete profile caused by an impurity in a stacked ladder system.

To describe now spin ladders other than the impurity inhering one, an ansatz comparable to the color model is used. For the leg with j=0 and k=1 (one ladder above the impurity inhering one) the expectation value of the spin $\langle S^z_{i,0,1}\rangle$ can be calculated by considering the influence of all spins on the ladder leg $S^z_{i,0,0}$, which describes the magnetic moment profile sufficiently well. For the next neighbouring ladder with k=2, the profile is calculated by considering only the influence of $S^z_{i,0,1}$. This procedure is repeated until the end of the stack is reached. The strength of the coupling between all the ladders can be modelled by a single ladder-independent coupling factor κ_z taken from the QMC results. Equ. 11.2 describes the spin profiles on the leg with j=0 for ladders with $k \geqslant 1$ to be

$$\langle S^z_{i,0,k}\rangle = e^{-\frac{1}{\kappa_z}} \sum_{l=-\frac{L_x}{2}}^{\frac{L_x}{2}} (-1)^{|l|+1} \langle S^z_{i+l,0,k-1}\rangle e^{-\frac{|l|}{\xi_x}} \tag{11.2}$$

where L_x is the length of the ladders. Exploiting the profile symmetry for the stacked ladders around the ladder consisting the impurity and the antisymmetry of the ladder legs the profile on the legs with j=1 is simply given as

$$\langle S^z_{i,1,k}\rangle = -\langle S^z_{i,0,k}\rangle \tag{11.3}$$

and

$$\langle S^z_{i,j,-k}\rangle = \langle S^z_{i,j,k}\rangle \tag{11.4}$$

for $k \geqslant 1$. To determine κ_z one applies Equs. 10.3, 11.1, and 11.2 for H=H_{ref} and T=T_{ref} and obtains

$$\langle S^z_{0,0,1}\rangle = -\langle S^z_0\rangle e^{-\frac{1}{\kappa_z}} \left(1 + 2\sum_{l=1}^{\frac{L_x}{2}} e^{-\frac{2l}{\xi_x}}\right) \tag{11.5}$$

with $\langle S^z_{0,0,1}\rangle$, $\langle S^z_0\rangle$ and ξ_x taken from the QMC simulation.

11.4 Profile of Multiple Impurities

Is the effective local magnetic moment profile caused by a single impurity calculated one can easily generate magnetic moment profiles for multiple impurities. To do so one simply has to superimpose the single impurity local effective moment profiles with respect to the impurtiy positions. To demonstrate how well this analytical model works two different profiles for different impurity configurations have been compared to their respective QMC profiles and plotted in Fig. 11.5. The QMC results (solid blue lines) are almost perfectly covered by the analytically generated profiles (solid red lines / open circles). Note that this fit only uses three parameters taken from a single QMC simulation, namely $\langle S^z_0\rangle$, ξ_x, and κ_z. Since the magnetic moment profiles can now be described analytically the problem of the stochastic noise is solved. However, the stochastic noise is still existent in the QMC simulation from which $\langle S^z_0\rangle$, ξ_x, and κ_z are obtained and therefore the statistical errors of those parameters need to be considered.
It has to be mentioned that even tough this method works well for most impurity configurations, it is not exact for close impurities residing on the same ladder (see next section). The impact of this deviation is not strong as long as the impurity concentration is sufficiently small enough. Further

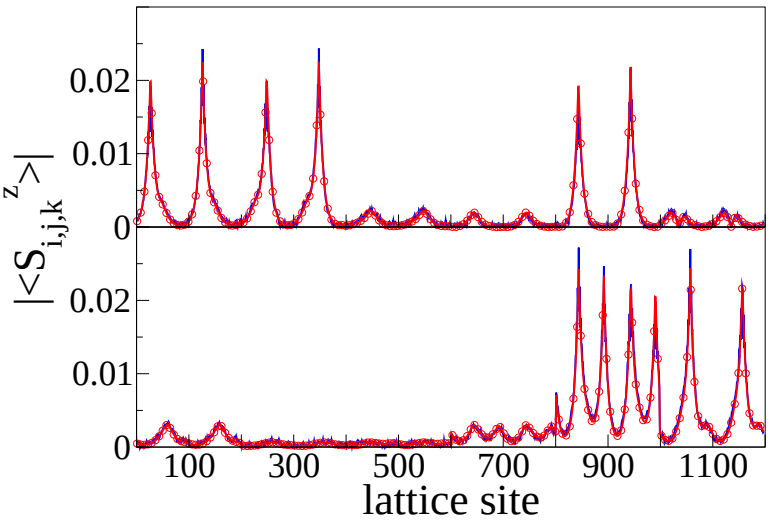

Figure 11.5: Illustration of the great quality of the analytical fit for two different impurity configurations.

the speed advantage of needing only a single QMC simulation outweighs the handicap in accuracy for qualitative analysis. However, for calculations that rely on accuracy a correction is needed that is obtained by performing additional QMC simulations as is shown in the next section.

11.5 Correction for Close Impurities

As discussed in Sec. 10.6.3 already, close impurities on the same spin ladder interact in a way so that simple superimposing of single impurity spin clouds is not valid anymore. However, it turns out that it is sufficient enough to replace $\langle S_0^z(\frac{H_{ref}}{T_{ref}})\rangle$ from Equ. 10.3 by a distance dependent $\langle S_0^z(\frac{H_{ref}}{T_{ref}}, dist)\rangle_{2Imp}$ obtained by performing a distance scan of 2 impurities with QMC simulations. Note that $\langle S_0^z(\frac{H_{ref}}{T_{ref}}, dist)\rangle_{2Imp}$ is not directly taken from the QMC simulation, since the QMC result contains already the superimposed value from the close-by impurity. To convert the QMC values ($\langle S_0^z(\frac{H_{ref}}{T_{ref}}, dist)\rangle_{QMC}$) into $\langle S_0^z(\frac{H_{ref}}{T_{ref}}, dist)\rangle_{2Imp}$ the superposition has to be taken out resulting in

$$\langle S_0^z(\frac{H_{ref}}{T_{ref}}, dist)\rangle_{2Imp} = \frac{\langle S_0^z(\frac{H_{ref}}{T_{ref}}, dist)\rangle_{QMC}}{1 + (-1)^{|i|+|j|} e^{-\frac{dist}{\xi_x}}} \quad . \tag{11.6}$$

Along with replacing $A(\xi_x)$ by the proper term Equ. 10.3 then becomes

$$\langle S^z_{i,j}(\frac{H}{T})\rangle = \langle S^z_0(\frac{H_{ref}}{T_{ref}}, dist)\rangle_{2Imp}(-1)^{|i+j|}e^{-\frac{|i|}{\xi_x}}\frac{1}{2}\frac{\tanh(\frac{\mu_B H}{k_B T})}{\tanh(\frac{\mu_B H_{ref}}{k_B T_{ref}})} \quad . \quad (11.7)$$

Equ. 11.7 describes effectively a magnetic moment profile caused by a single impurity on a single spin ladder, but already includes the enhancement caused by interaction of close impurities. To generate profiles for multiple impurities one simply has to superimpose the single magnetic moment profiles resulting from Equ. 11.7. In Fig. 11.6 the quality of the adjusted analytical description is demonstrated. There magnetic moment profiles for a distance of 13 lattice sites (different sublattices) and a distance of 14 lattice sites (same sublattices) are plotted for QMC results (black and green triangles with error bars) and compared to Equ. 11.7 (solid blue lines). Since no enhancement of a magnetic moment profile for impurities at dif-

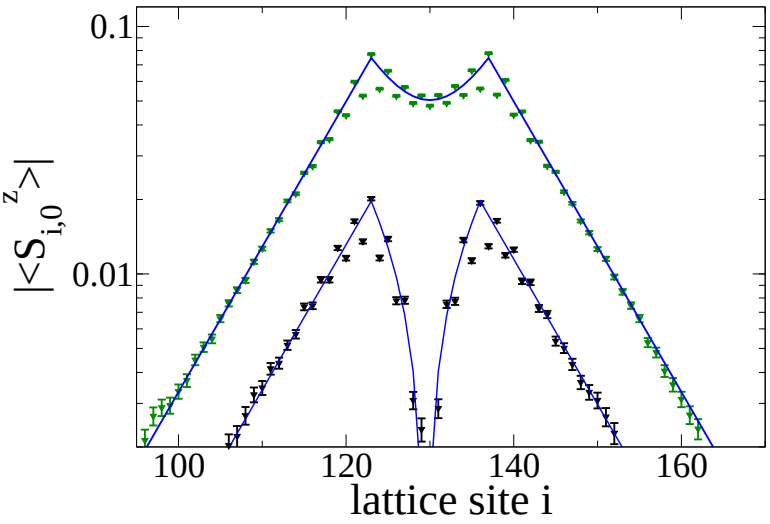

Figure 11.6: Magnetic moment profiles caused by close impurities on the same ladder leg. Full lines: fit according to Equ.11.7, symbols: QMC results. Upper curve: impurities are located at positions 123 and 137 at the same sublattice. Lower curve: impurities are located at positions 123 and 136 at different sublattices. QMC simulation for $J_R/J_L = 0.5$, $H/J_L = 0.01$, $T/J_L = 0.02083$.

ferent ladders has been observed the same procedure explained in Sec. 11.3 can be used to generate the magnetic moment profile at neighbouring ladders. To demonstrate the improved accuracy obtained by the just adjusted

analytical function Fig. 11.7 compares a QMC profile (black line) with the analytical description with (blue line) and without (red line) correction. For

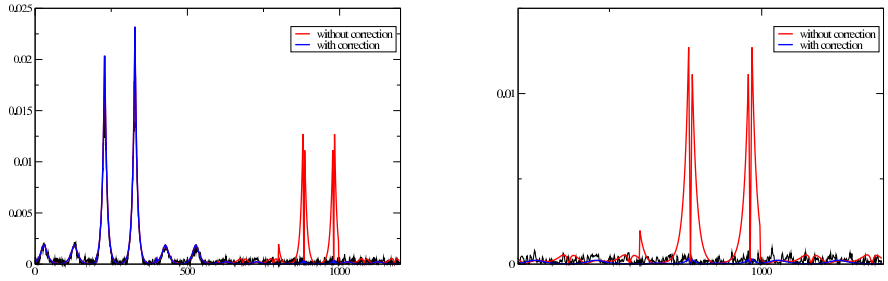

Figure 11.7: QMC results (black line) compared to its analytical fit with (blue line) and without (red line) correction for close impurities residing on the same ladder.

large impurity concentrations one needs to perform configuration analysis also for more than just 2 impurities on the same ladder. But since this work is primarily focused on small impurity concentrations $x \leqslant 0.0025$ it is sufficient to restrict our simulation to these pairs of impurities, since due to combinatoric reasons already three close impurities would occur with a probability of less than 0.6%.

11.6 Complete Procedure to simulate NMR Spectra closer to Reality

With the analytical description being complete following procedure needs to be applied to simulate NMR spectra closer to reality.

1. Perform a single QMC calculation for the desired system containing a single impurity only. Temperature and external field should be chosen according to produce a significant effective local magnetic moment profile for further data analysis (e.g. T/J_L=0.02, H/J_L=0.01).

2. Extract $\langle S_0^z \rangle$, ξ_x, and κ_z from the QMC results.

3. Optional for higher accuracy and/or higher impurity concentration: Perform a distance scan of $\langle S_0^z(\frac{H_{ref}}{T_{ref}}, dist)\rangle_{2Imp}$. For larger impurity concentrations even 3 ore more impurities need to be considered.

4. Calculate the effective local magnetic moment profile around a single impurity using Equ. 11.7 for the central ladder and Equ. 11.2 for neighbouring ladders (by taking the systems symmetry into account).

5. Generate a random impurity configuration with the desired concentration.

6. Optional for higher accuracy and/or higher impurity concentration: Determine if impurities reside on the same ladder and if so their distance *dist*.

7. For every impurity the corresponding effective local magnetic moment profile is superimposed on the whole system.

8. Calculate the resonance field profile according to to Equ. 8.5.

9. Repeat points 5 and 8 until a desired number of configurations is achieved.

10. The final NMR spectrum then corresponds to the histogram (smeared with a gaussian simulating the natural linewidth) of all generated resonance profiles.

With this procedure it is possible to reduce the calculation time tremendously compared to a direct QMC approach. While a single QMC simulation might take already a few hours the analytical model provides a way to generate and simulate thousands of impurity configurations within a few minutes. Further with this model the temperature behaviour of the magnetic moment profile is known for regions with almost constant correlation length. Thus the effectiveness in CPU time is increased significantly, considering that only a small amount of QMC simulations (One single impurity simulation + the optional 80 simulations for the distance scan of two close impurities for J_R/J_L=0.5) is needed in the beginning to built up the analytical model compared to thousands of core hours for thousands of QMC simulations.
It needs to be mentioned that this model focuses on the broadening effect only. The shift of NMR peak from smaller to larger temperatures caused by a collective excitation of all the spins is not being considered. However, to calculate the shift of the resonance field peak one simply has to perform a temperature scan with QMC simulations of a system without an impurity.

Chapter 12

Results and Discussion

The results presented in this chapter are obtained by following the procedure derived within this work (see Sec. 11.6). All results are assumed to have constant correlation length ξ_x and constant inter ladder coupling factor κ_z. As was shown earlier (see Sec. 10.3) this assumption is valid for the temperature range in which the low temperature broadening effect occurs and for higher temperatures the effective local magnetic moment profile vanishes anyway. Further only close impurity interactions (see Sec. 10.6.3) of not more than two impurities are considered, which is sufficient for systems doped with a tiny amount ($x \leqslant 0.0025$) of impurities. Additionally only stacked ladder systems are investigated since single ladders alone cannot lead to the desired broadening effect.

12.1 Results within the 1-σ Range of Johnston at al.

The first calculations are performed within a 1-σ range of parameters suggested by Johnston at al.[43] Further to generate NMR spectra comparable to the experiment of Fujuwara et al.[28] an impurity concentration of x=0.0025 is used along with temperatures of ∼40 K and ∼330 K. In Fig. 12.1 the resulting calculated NMR spectra at 40K and room temperature as well as the experimental spectrum at 40K are plotted. As expected at room temperature (∼330 K, dashed blue line) no broadening effect is observed. The results at room temperature are also fairly independent of the stacking coupling constant J_3/J_L. This is in agreement with the first investigations

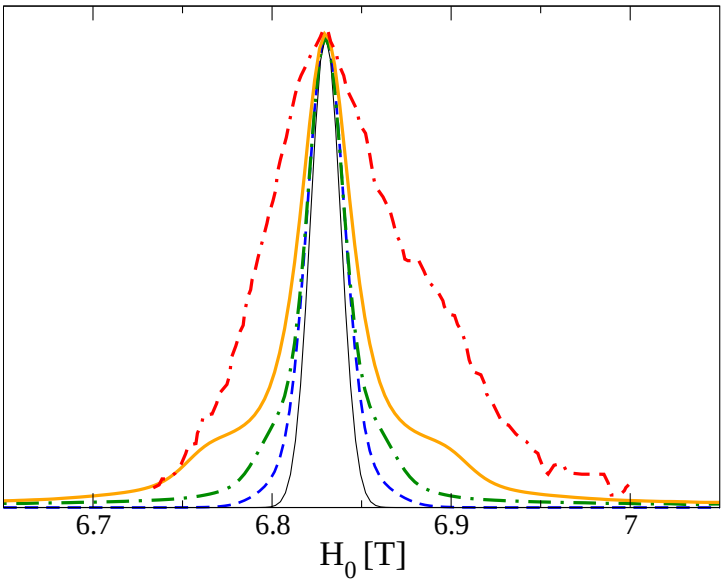

Figure 12.1: NMR Spectra for T = 40K, J_L = 1905K and J_R/J_L = 0.5 with J_3/J_L = 0.01 (red/dot-dashed line) and J_3/J_L = 0.02 (solid orange line). To see the temperature effect of the NMR broadening references lines at room temperature for doped (blue/dashed line) and undoped (thin solid line) systems have been added.

in Sec. 10.3 and confirms the validity of the analytical model at high temperatures even tough the correlation lengths is assumed to be constant with the fixed value taken from $\sim$ 40K. The reason is that the impurity induced magnetic moment profile at high temperatures simply has too small values to have a notable influence on the NMR spectrum. On the other hand the cooled systems ($\sim$40 K, green dot-dashed line for J_3/J_L=0.01, solid orange line for J_3/J_L=0.02) show the desired broadening effect even tough not as large as in experiment (red dot-double-dashed line). Note that in Johnston et al . [43] the ratio J_R/J_L was kept constant at 0.5 for stacked systems and the best fit to the susceptibility was made for a single ladder. Thus an adjustment for J_R/J_L is reasonable and can lead to a larger correlation length and thus to a stronger broadening effect. However, this work is focused mainly on the influence of a stacked coupling constant and only suggests a further analysis of J_R/J_L in $SrCu_2O_3$ for future investigations.

12.2 Results within the 2-σ Range of Johnston et al.

QMC simulations with a coupling constant in stacking direction at the border of the 2-σ range of Johnston et al.[43], namely J_3/J_L=0.03, are performed. The other system parameters remain un changed (see Sec. 12.1). In Fig. 12.2 the resulting NMR spectrum (solid red line) is compared to the experiment. The result looks very promising as the FWHM of the simu-

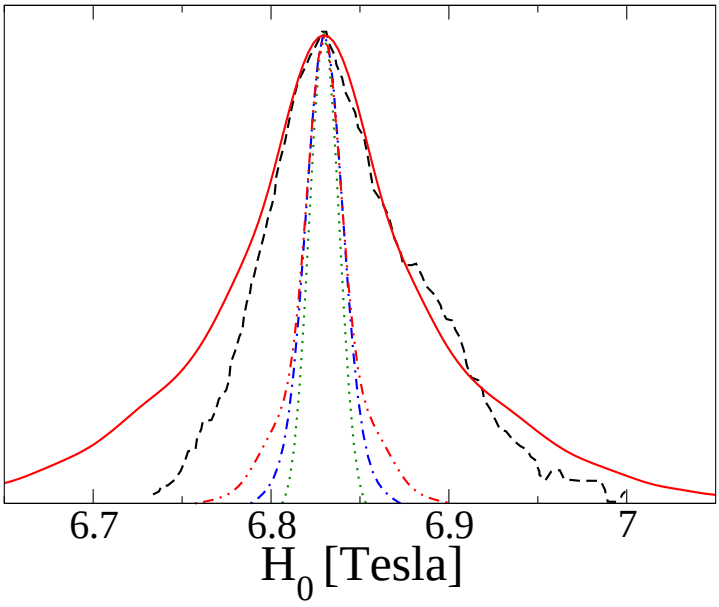

Figure 12.2: NMR Spectra for T = 40K, J_L = 1905K and J_R/J_L = 0.5 with J_3/J_L = 0.01 (red/dot-dot-dashed line) and J_3/J_L = 0.03 (solid red line) compared to experiment (black dashed line). To see the temperature effect of the NMR broadening reference lines at 336K for doped (blue dot-dashed line) and undoped (green dotted line) systems are shown.

lated NMR spectrum even exceeds the experimental one. However, it needs to be mentioned that for increasing J_3/J_L the haldane gap decreases until vanishing completely between $0.04<J_3/J_L<0.05$. The change in the gap has an influence on other system properties. To keep the haldane gap at a constant value one has to adjust the main coupling constant J_L accordingly. Further different combinations of J_R/J_L and J_3/J_L or even a ring exchange within the ladders could be considered to obtain a similar broadening effect but with less impact on the haldene gap. Again, this work focuses on the

qualitative description of the low temperature broadening effect considering stacked ladder systems and leaves more detailed investigations on the different parameter sets for future studies.

12.2.1 Comparison to the Experiment of Fijuwara at al.

So far only NMR spectra at two different temperatures, namely at 40K and 336K, have been calculated. To compare the temperature dependence over the whole temperature range used in experiment simulations at different temperatures with different combinations of J_R/J_L and J_3/J_L at different temperatures have been performed. The resulting FWHM are demonstrated in Fig. 12.3.

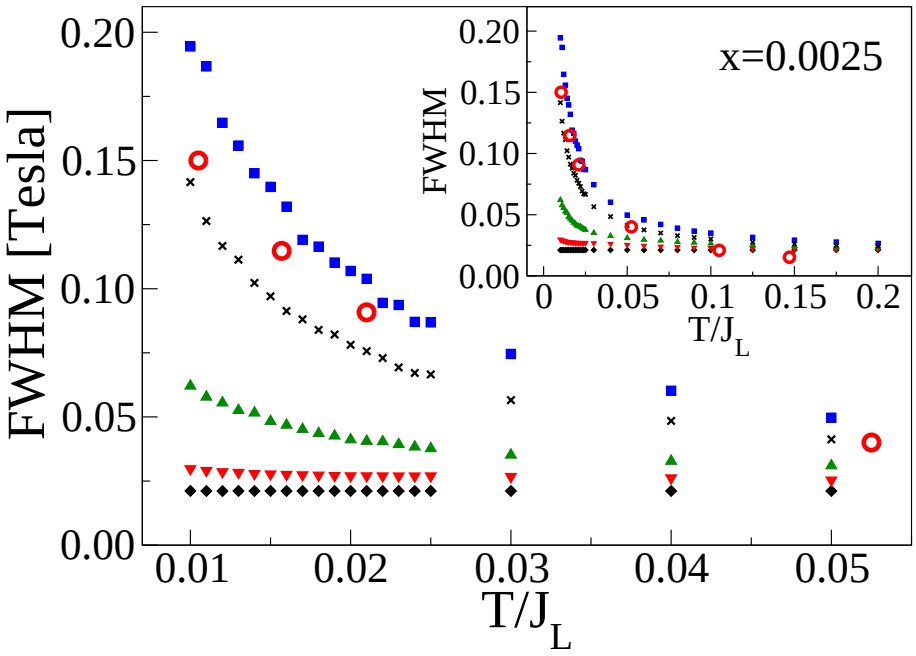

Figure 12.3: FWHM of the ^{65}Cu central peak vs temperature for a stacked ladder system with J_L = 1920K, $J_R/J_L = 0.5$, and varying inter ladder coupling J_3/J_L: 0.0 (black diamonds), 0.01 (red down-triangles), 0.02 (green up-triangles) and 0.03 (blue squares) . To show the influence of the rung coupling we perform a calculation for $J_R/J_L = 0.4$ and $J_3/J_L = 0.02$ (crosses). The individual correlation lengths for each curve are extracted from a QMC calculation around $T/J_L = 0.02083$ (=40K) and assumed to be independent of temperature. Experimental values are given by red open circles. The inset shows an expanded temperature range.

The different parameters used for this plot are J_R/J_L=0.5 with J_3/J_L=0.0 (black diamonds), J_3/J_L=0.01 (red down triangles), J_3/J_L=0.02 (green up triangles), J_3/J_L=0.03 (blue squares). Additionally simulations with J_R/J_L=0.4 and J_3/J_L=0.02 (black crosses) have been performed. J_L is kept fixed at 1920K. The red circles correspond to the measured FWHM taken from the experiment of Fujiwara et al.[28] The temperature range of the main graph is between 19K and 105K. The inset shows the extended temperature range up to 384K. The shape of the temperature dependent FWHM curve for the parameter set J_R/J_L=0.5 with J_3/J_L=0.03 (blue symbols) is in good agreement with experiment. At higher temperature ($T/J_L \geqslant 0.1$) there is quite a strong deviation tough considering that there should be almost no impurity influenced effective local magnetic moment profile. The reason for this deviation is the natural linewidth used in the simulations. Fujiwara et al. [28] mentioned a natural linewidth of 0.02 Tesla at low temperatures (4.2K), but for room temperature a linewidth of 0.01 Tesla. In this work only a natural linewidth of 0.02 Tesla was used, since the most interesting temperature range is below T/J_L=0.05, which explains the larger FWHM at higher

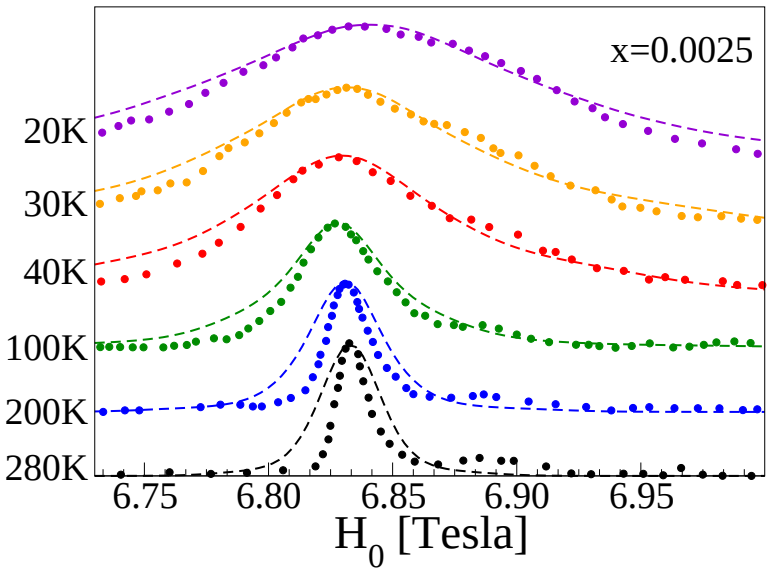

Figure 12.4: ^{65}Cu left peak NMR Spectra for J_L= 1920K J_R/J_L = 0.5 and J_3/J_L = 0.03 with different temperatures compared with experiment (filled circles) with a concentration of x=0.0025 and ν_{RF} = 83.55MHz.

temperatures compared to experiment. Also the curve for J_R/J_L=0.4 with

J_3/J_L=0.02 (black crosses) shows qualitatively a similar behaviour, which shows that more detailed investigation for an improved parameter set would be reasonable for future studies.
While the FWHM is the primary indicator for the low temperature broadening effect, the shape of the NMR spectra is important as well. For this purpose NMR spectra at different temperatures taken from experiment are compared to the simulated NMR spectra for the parameter set with J_R/J_L=0.5 with J_3/J_L=0.03 (see Fig. 12.4). As can be observed the simulated NMR spectra are in good agreement with the experimental ones. At lower temperatures the simulated ones are a bit wider, but the shape is comparable. The difference at higher temperatures results again from the differing natural linewidth.

12.2.2 Comparison to the Experiment of Ohsugi at al.

The results with the system parameters J_R/J_L=0.5 and J_3/J_L=0.03 presented in Sec. 12.2.1 are promising. However, so far the simulations have been compared only to one experiment with an impurity concentration of x=0.0025. To test the simulated spectra also on experiments performed by Ohsugi et al.[29] simulations are performed according to the experimental impurity concentrations. Note that in the simulations the parameters used for the analytical description are the same as for Sec. 12.2.1. Only the impurity concentration and the resonance condition parameters (ν_{RF} and external field H_0 for the main peak) have been adjusted according to experiment. The different impurity concentrations can be simulated by adjusting the size of the system box and the number of impurities.
In Fig. 12.5 simulated spectra are compared to experimental ones of a system with an impurity concentration of x=0.001. Again the simulated NMR spectra describe the experimental ones qualitatively very well. The asymmetry in the experimental NMR spectra below 40K is caused by an overlap with a ^{63}Cu transition that has its main peak around 10.05 Tesla. But the agreement on the unperturbed left side is noticeable. Results for quite large impurity concentrations, namely x=0.01 and x=0.02, are plotted in Fig 12.6. Also for these large impurity concentrations the qualitative behaviour is described fairly well by the simulated NMR spectra. However, at lower temperatures the simulated broadening effect appears to become larger compared to experiment. This is not a surprise considering that the analytical

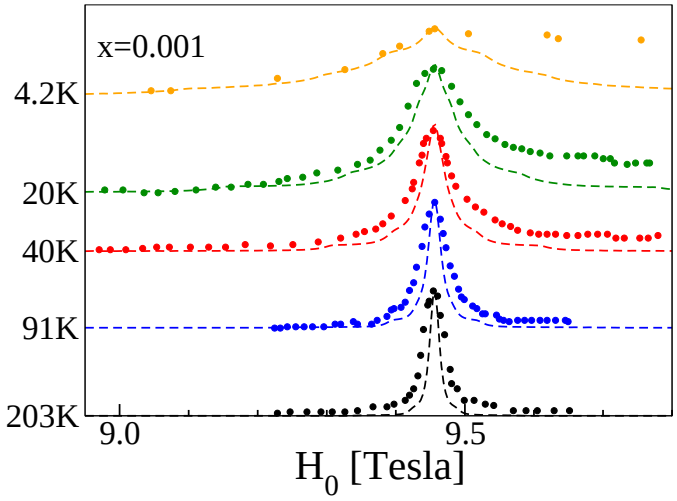

Figure 12.5: ^{65}Cu left peak NMR Spectra for J_L= 1920K J_R/J_L = 0.5 and J_3/J_L = 0.03 with different temperatures compared with experiment (filled circles) with a concentration of x=0.001 and $\nu_{RF} = 125.1MHz$. The asymmetric experimental profiles below 40K are caused by an overlap of a ^{63}Cu transition with it's main peak around 10.05 Tesla.

model used for the simulations only considers up to two close impurities residing on a the same ladder (see Sec. 11.5). While for small impurity concentrations (x$\leqslant$0.0025) this approximation works well, for larger impurity concentrations an additional configuration scan with more close impurities residing on the same ladder is required for more accurate results. The procedure should be comparable to a cluster algorithm in which the different impurity configurations correspond to different clusters.

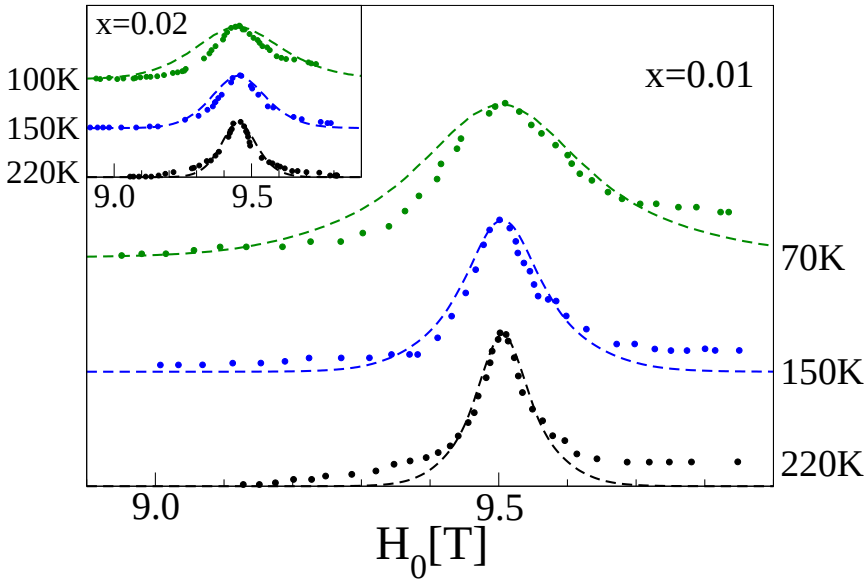

Figure 12.6: ^{65}Cu left peak NMR Spectra for J_L= 1920K J_R/J_L = 0.5 and J_3/J_L = 0.03 with different temperatures compared with experiment (filled circles) with a concentration of x=0.01. The inset shows the same system with an impurity concentration of x=0.02.

Part IV

Conclusion

Conclusion

This work describes the complete process of developing a Quantum Monte Carlo (QMC) code in the framework of the Stochastic Series Expansion (SSE) towards its application on realistic systems. The analysed experimentally observed effect is the low temperature broadening of the Cu NMR line in the spin ladder compound $SrCu_2O_3$ when doped with a small amount ($x \leqslant 0.0025$) of non magnetic impurities.

Here it is shown that the broadening effect can be reproduced by modelling the system with coupled stacked spin ladders without the need of physically unlikely large correlation lengths. This was required in former studies using non stacked systems. Further a framework was developed that allows to simulate NMR spectra of realistic materials for a certain temperature range with a small amount of QMC simulations.

This strong reduction in computation time can help future studies to investigate NMR spectra of spin ladder compounds using even more complex parameter sets as well as finding improved parameter sets to model real systems better.

Acknowledgements

I would like to express the deepest appreciation to my supervisor, Professor Peter Mohn, who has also become a friend over the years. Without his guidance and persistent help this dissertation would not have been possible.
I want to thank my family, in especially my parents, Erich and Christine, for supporting me my whole life.
Also I want to thank my lovely wife, Laura, for her moral support as well as for her patience, which she proofed to have during the final stages of my thesis.
Further I want to thank Professor Hans Gerd Evertz from the University of Technology of Graz for his collaboration and support.
I acknowledge the support from the Austrian Science Fonds FWF within the Science College W401-N13 and the SFB ViCoM F4109-N13 P04 and P09.

Bibliography

[1] R. Achleitner, "Monte carlo simulation methods for quantum mechanical systems," Diploma thesis, Vienna University of Technology, 2008.

[2] R. Achleitner, R. Gamillscheg, H.-G. Evertz, and P. Mohn, "Quantum monte carlo simulations for stacked spin ladder systems containing low concentrations of non-magnetic impurities; application to the low temperature broadening of NMR-Spectra in $SrCu_2O_3$," *Phys. Rev. B submitted*, 2013.

[3] N. Metropolis, "The beginning of the monte carlo method," *Los Alamos Science*, pp. 125–130, 1987.

[4] N. Metropolis and S. Ulam, "The monte carlo method," *Journal of the American Statistical Association*, vol. 44, pp. 335–341, 1949.

[5] M. Matsumoto and T. Nishimura, "Mersenne twister: a 623-dimensionally equidistributed uniform pseudo-random number generator," *ACM Trans. Model. Comput. Simul.*, vol. 8, pp. 3–30, 1998.

[6] N. Metropolis, A. Rosenbluth, M. Rosenbluth, A. Teller, and E. Teller, "Equation of state calculations by fast computing machines," *J. Chem. Phys. 21*, 1953.

[7] A. A. Markov, "An example of statistical investigation of the text eugene onegin concerning the connection of samples in chains," *Science in Context*, vol. 19, pp. 591–600, 2006.

[8] E. Ising, "Beitrag zur Theorie des Ferromagnetismus," *Zeitschrift für Physik*, vol. 31, no. 1, pp. 253–258, 1925.

[9] W. Heisenberg, "Zur Theorie des Ferromagnetismus," *Zeitschrift für Physik*, vol. 49, no. 9-10, pp. 619–636, 1928.

[10] P. Mohn, *Magnetism in the Solid State*. Springer Series in Solid-State Sciences , Volume 134, 2003.

[11] J. Yeomans, *Statistical Mechanics of Phase Transitions*. Oxford: Oxford University Press, 1992.

[12] D. C. Handscomb, "The monte carlo method in quantum statistical mechanics," *Mathematical Proceedings of the Cambridge Philosophical Society*, vol. 58, pp. 594–598, 1962.

[13] D. C. Handscomb, "A monte carlo method applied to the heisenberg ferromagnet," *Mathematical Proceedings of Camebridge Philosophical Society*, vol. 60, pp. 115–122, 1964.

[14] A. W. Sandvik and J. Kurkijärvi, "Quantum monte carlo simulation method for spin systems," *Phys. Rev. B*, vol. 43, no. 7, pp. 5950–5961, 1991.

[15] A. W. Sandvik, "Stochastic series expansion method with operator-loop update," *Phys. Rev. B*, vol. 59, pp. R14157–R14160, 1999.

[16] O. F. Syljuåsen and A. W. Sandvik, "Quantum monte carlo with directed loops," *Phys. Rev. E*, vol. 66, no. 4, p. 046701, 2002.

[17] O. F. Syljuåsen, "Directed loop updates for quantum lattice models," *Phys. Rev. E*, vol. 67, p. 046701, 2003.

[18] H. G. Evertz, G. Lana, and M. Marcu, "Cluster algorithm for vertex models," *Phys. Rev. Lett.*, vol. 70, pp. 875–879, 1993.

[19] R. H. Swendsen and J.-S. Wang, "Nonuniversal critical dynamics in monte carlo simulations," *Phys. Rev. Lett.*, vol. 58, no. 2, pp. 86–88, 1987.

[20] "OpenMP." Website. http://www.openmp.org.

[21] "OpenMPI." Website. http://www.open-mpi.org.

[22] MATLAB. Natick, Massachusetts: The MathWorks Inc., 2010.

[23] M. Suzuki, "Fractal decomposition of exponential operators with applications to many-body theories and monte carlo simulations," *Physics Letters A*, vol. 146, no. 6, pp. 319 – 323, 1990.

[24] A. W. Sandvik, "Stochastic series expansion method for quantum ising models with arbitrary interactions," *Phys. Rev. E*, vol. 68, p. 056701, 2003.

[25] M. Azuma, H. Yoshida, T. Saito, T. Yamada, and M. Takano, "Pressure-induced buckling of spin ladder in $SrCu_2O_3$," *J Am Chem Soc*, vol. 126, no. 26, pp. 8244–6, 2004.

[26] K. Sparta, A. Löffert, C. Gross, W. Aßmus, and G. Roth, "Single crystal x-ray structure analysis of the spin ladder compounds $SrCu_2O_3$ and $Sr_2Cu_3O_5$ between 300 K and 100 K," *Zeitschrift für Kristallographie*, vol. 221, no. 12, pp. 782–787, 2006.

[27] S. Gopalan, T. M. Rice, and M. Sigrist, "Spin ladders with spin gaps: A description of a class of cuprates," *Phys. Rev. B*, vol. 49, pp. 8901–8910, 1994.

[28] N. Fujiwara, H. Yasuoka, Y. Fujishiro, M. Azuma, and M. Takano, "NMR study of Zn doping effect in spin ladder system $SrCu_2O_3$," *Phys. Rev. Lett.*, vol. 80, pp. 604–607, 1998.

[29] S. Ohsugi, Y. Tokunaga, K. Ishida, Y. Kitaoka, M. Azuma, Y. Fujishiro, and M. Takano, "Impurity-induced staggered polarization and antiferromagnetic order in spin-$\frac{1}{2}$ Heisenberg two-leg ladder compound $SrCu_2O_3$: Extensive Cu NMR and NQR studies," *Phys. Rev. B*, vol. 60, pp. 4181–4190, 1999.

[30] Y. Iino and M. Imada, "Effects of nonmagnetic impurity doping on spin ladder system," *Journal of the Physical Society of Japan*, vol. 65, no. 12, pp. 3728–3731, 1996.

[31] Y. Motome, N. Katoh, N. Furukawa, and M. Imada, "Impurity effect on spin ladder system," *Journal of the Physical Society of Japan*, vol. 65, no. 7, pp. 1949–1952, 1996.

[32] G. B. Martins, M. Laukamp, J. Riera, and E. Dagotto, "Local enhancement of antiferromagnetic correlations by nonmagnetic impurities," *Phys. Rev. Lett.*, vol. 78, pp. 3563–3566, 1997.

[33] H.-J. Mikeska, U. Neugebauer, and U. Schollwöck, "Spin ladders with nonmagnetic impurities," *Phys. Rev. B*, vol. 55, pp. 2955–2963, 1997.

[34] A. W. Sandvik, E. Dagotto, and D. J. Scalapino, "Nonmagnetic impurities in spin-gapped and gapless heisenberg antiferromagnets," *Phys. Rev. B*, vol. 56, pp. 11701–11709, 1997.

[35] M. Laukamp, G. B. Martins, C. Gazza, A. L. Malvezzi, E. Dagotto, P. M. Hansen, A. C. López, and J. Riera, "Enhancement of antiferromagnetic correlations induced by nonmagnetic impurities: Origin and predictions for NMR experiments," *Phys. Rev. B*, vol. 57, pp. 10755–10769, 1998.

[36] R. Kilian, S. Krivenko, G. Khaliullin, and P. Fulde, "Impurity-induced spin polarization and NMR line broadening in underdoped cuprates," *Phys. Rev. B*, vol. 59, pp. 14432–14439, 1999.

[37] M.-H. Julien, T. Fehér, M. Horvatić, C. Berthier, O. N. Bakharev, P. Ségransan, G. Collin, and J.-F. Marucco, "^{63}Cu NMR evidence for enhanced antiferromagnetic correlations around Zn impurities in $YBa_2Cu_3O_{6.7}$," *Phys. Rev. Lett.*, vol. 84, pp. 3422–3425, 2000.

[38] H. Alloul, J. Bobroff, M. Gabay, and P. J. Hirschfeld, "Defects in correlated metals and superconductors," *Rev. Mod. Phys.*, vol. 81, pp. 45–108, 2009.

[39] M. Greven, R. J. Birgeneau, and U. J. Wiese, "Monte carlo study of correlations in quantum spin ladders," *Phys. Rev. Lett.*, vol. 77, pp. 1865–1868, 1996.

[40] M. Greven and R. J. Birgeneau, "Correlations and Néel order of randomly diluted quantum spin ladders," *Phys. Rev. Lett.*, vol. 81, pp. 1945–1948, 1998.

[41] J. Bobroff, N. Laflorencie, L. K. Alexander, A. V. Mahajan, B. Koteswararao, and P. Mendels, "Impurity-induced magnetic order in low-dimensional spin-gapped materials," *Phys. Rev. Lett.*, vol. 103, p. 047201, 2009.

[42] L. K. Alexander, J. Bobroff, A. V. Mahajan, B. Koteswararao, N. Laflorencie, and F. Alet, "Impurity effects in coupled-ladder $BiCu_2PO_6$ studied by nmr and quantum monte carlo simulations," *Phys. Rev. B*, vol. 81, p. 054438, 2010.

[43] D. C. Johnston, M. Troyer, S. Miyahara, D. Lidsky, K. Ueda, M. Azuma, Z. Hiroi, M. Takano, M. Isobe, Y. Ueda, M. A. Korotin, V. I. Anisimov, A. V. Mahajan, and L. L. Miller, "Magnetic susceptibilities of spin-1/2 antiferromagnetic heisenberg ladders and applications to ladder oxide compounds," 2000.

[44] J. Sirker and N. Laflorencie, "NMR response in quasi-one-dimensional spin-1/2 antiferromagnets," *EPL*, vol. 86, no. 5, 2009.

[45] H. Alloul, P. Mendels, H. Casalta, J. F. Marucco, and J. Arabski, "Correlations between magnetic and superconducting properties of Zn-substituted $YBa_2Cu_3O_{6+x}$," *Phys. Rev. Lett.*, vol. 67, pp. 3140–3143, 1991.

[46] K. Ishida, Y. Kitaoka, N. Ogata, T. Kamino, K. Asayama, J. R. Cooper, and N. Athanassopoulou, "Cu NMR and NQR studies of impurities-doped $YBa_2(Cu_{1-x}M_x)_3O_7$ (M=Zn and Ni)," *Journal of the Physical Society of Japan*, vol. 62, no. 8, pp. 2803–2818, 1993.

[47] G. V. M. Williams, J. L. Tallon, and R. Dupree, "NMR study of magnetic and nonmagnetic impurities in $YBa_2Cu_4O_8$," *Phys. Rev. B*, vol. 61, pp. 4319–4325, 2000.

[48] F. Casola, T. Shiroka, S. Wang, K. Conder, E. Pomjakushina, J. Mesot, and H.-R. Ott, "Direct observation of impurity-induced magnetism in

a spin-$\frac{1}{2}$ antiferromagnetic Heisenberg two-leg spin ladder," *Phys. Rev. Lett.*, vol. 105, p. 067203, 2010.

[49] "Blender." Website. http://www.blender.org.

[50] Z. Hiroi, M. Azuma, M. Takano, and Y. Bando, "A new homologous series Sr(n-1)Cu(n+1)O(2n) found in the SrO-CuO system treated under high pressure," *Journal of Solid State Chemistry*, vol. 95, no. 1, pp. 230 – 238, 1991.

[51] Y. Mizuno, T. Tohyama, and S. Maekawa, "Superexchange interaction in cuprates," *Phys. Rev. B*, vol. 58, pp. R14713–R14716, 1998.

[52] M. Azuma, Z. Hiroi, and M. Takano, "High pressure synthesis and magnetic properties of quasi one dimensional systems Sr[n-1]Cu[n+1]O[2n] (n=3, 5)," *Bulletin of the Institute for Chemical Research, Kyoto University*, vol. 72, pp. 187–194, 1994.

[53] H. Evertz, "Coupled quantum chains: A bumpy path from 1 to 2 dimensions," *Computer Simulations in Condensed Matter Physics IX*, p. 59, 1996.

[54] F. Tedoldi, R. Santachiara, and M. Horvatić, " ^{89}Y NMR imaging of the staggered magnetization in the doped haldane chain $Y_2BaNi_{1-x}Mg_xO_5$," *Phys. Rev. Lett.*, vol. 83, pp. 412–415, 1999.